

Nonlinear Effects in Granular Crystals with
Broken Periodicity

Thesis by
Joseph John Lydon II

In Partial Fulfillment of the Requirements for the degree
of
Doctor of Philosophy



CALIFORNIA INSTITUTE OF TECHNOLOGY

Pasadena, California

2015

(Defended December, 17th 2014)

To my family and friends

© 2015

Joseph John Lydon II

All Rights Reserved

ACKNOWLEDGEMENTS

I would like to first and foremost acknowledge and thank my advisor, Chiara Daraio. She has supported me through each step of my graduate research. When I was unsure or disappointed with my research direction, she supported me with much needed guidance. Her feedback and discussions on each of the research projects were invaluable. She gave me a tremendous amount of freedom in pursuing research problems that interested me. I especially would like to thank her for offering me an unparalleled graduate research experience.

I thank all the members of my thesis committee: William Johnson, Brent Fultz, Keith Schwab, and Austin Minnich. Professor Fultz, thank you for all of your guidance and support, specifically regarding our first few conversations on your perspectives and passions in materials science.

I would like to thank my mother, father, brother and sister. I love you all. Thank you mom for having complete and total faith and believing in me no matter what I do. Dad, thank you for helping me keep focus and greater perspective. I cherish all of our conversations.

To Ana Bucic, I am blessed to have met you.

To Marc Serra Garcia, discussing physics with you has been truly a pleasure and made this all fun. I thank you for our discussions, for you challenging me constantly, and for sharing your passion for science with me.

To Georgios Theocharis, I am lucky to have had your guidance. You have been an incredible mentor.

I would like to thank my good friends Andrew Morrison and Andrew Guichet. Thank you for all of the support. I could not ask for better friends.

ABSTRACT

When studying physical systems, it is common to make approximations: the contact interaction is linear, the crystal is periodic, the variations occurs slowly, the mass of a particle is constant with velocity, or the position of a particle is exactly known are just a few examples. These approximations help us simplify complex systems to make them more comprehensible while still demonstrating interesting physics. But what happens when these assumptions break down? This question becomes particularly interesting in the materials science community in designing new materials structures with exotic properties. In this thesis, we study the mechanical response and dynamics in granular crystals, in which the approximation of linearity and infinite size break down. The system is inherently finite, and contact interaction can be tuned to access different nonlinear regimes. When the assumptions of linearity and perfect periodicity are no longer valid, a host of interesting physical phenomena presents itself. The advantage of using a granular crystal is in its experimental feasibility and its similarity to many other materials systems. This allows us to both leverage past experience in the condensed matter physics and materials science communities while also presenting results with implications beyond the narrower granular physics community. In addition, we bring tools from the nonlinear systems community to study the dynamics in finite lattices, where there are inherently more degrees of freedom. This approach leads to the major contributions of this thesis in broken periodic systems. We demonstrate the first defect mode whose spatial profile can be tuned from highly localized to completely delocalized by simply tuning an external parameter. Using the sensitive dynamics near bifurcation points, we present a completely new approach to modifying the incremental stiffness of a lattice to arbitrary values. We show how

using nonlinear defect modes, the incremental stiffness can be tuned to anywhere in the force-displacement relation. Other contributions include demonstrating nonlinear breakdown of mechanical filters as a result of finite size, and the presents of frequency attenuation bands in essentially nonlinear materials. We finish by presenting two new energy harvesting systems based on our experience with instabilities in weakly nonlinear systems.

TABLE OF CONTENTS

Acknowledgements	iii
Abstract	iv
Table of contents	vi
List of figures and/or tables	viii
Introduction.....	1
1.1 Motivation	1
1.2 Goals and achievements	4
1.3 Structure of the thesis.....	6
Background information	8
2.1 Linear.....	8
2.2 Weakly nonlinear.....	12
2.3 Strongly nonlinear	18
2.4 Energy harvesting.....	19
Experimental setup	23
3.1 General experimental setup and tools.....	24
3.2 Measurement tools and techniques	26
3.3 Specific experimental setups	29
Modeling	33
4.1 Discrete particle model for the granular chain	33
4.1.1 Hamiltonian approximation.....	33
4.1.2 Nonconservative elements	35
4.2 Linear eigenanalysis and state space	36
4.3 Nonlinear modeling: integration and perturbation analysis	37
4.4 Modeling specific tools	44
4.5 Modeling for specific experiments.....	49
Linear dynamics in nonlinear lattices: Local to extended transitions of resonant defect modes.....	54
5.1 Introduction	54
5.2 Tuning mode profiles.....	56
5.3 Applications of tuning mode profiles.....	62
5.4 Analysis	64
5.5 Conclusion.....	70
5.6 Author contributions.....	70
Weakly nonlinear dynamic regime: Extraordinary stiffness tunability through thermal expansion of nonlinear defect modes	73
6.1 Introduction	73
6.2 Tuning the incremental stiffness in a granular chain.....	74
6.3 Transient Analysis	82
6.4 Author contribution	86

Weakly nonlinear dynamic regime: Nonlinear resonances and energy transfer in finite granular chains	87
7.1 Introduction	87
7.2 Results and discussion.....	91
7.3 Conclusion.....	105
7.4 Author contributions.....	106
Strongly nonlinear dynamic regime: Frequency bands of strongly nonlinear homogenous granular systems	107
8.1 Introduction	107
8.2 Experimental results	109
8.3 Conclusion.....	112
8.4 Author contributions.....	113
Applications: Energy harvesting	114
9.1 Energy harvesting inspired by thermal machines	114
9.2 Parametrically driven energy harvesting.....	122
9.2.1 Project goal.....	122
9.2.2 Introduction	123
9.2.3 Theoretical investigation.....	125
9.3 Author contributions.....	128
Conclusions & research summary.....	129
Bibliography.....	132
Appendix.....	140
1.1 Analytic modeling for extraordinary stiffness tunability.....	140
1.2 Analysis for strongly nonlinear frequency bands	147

LIST OF FIGURES AND/OR TABLES

<i>Number</i>	<i>Page</i>
Figure 2.1: a) Schematic for the acoustic band (red) of a monoatomic granular crystal. Effects of broken periodicity, finite size, and a defect mode are shown in blue. The long wavelength speed of sound is shown as the tangent as the wavenumber approaches zero (black). b) Setup by Man et al. ²⁷ to measure (c) the linear acoustic band and localized defect mode in a finite, 20 particle long, chain. Reprinted pending permission from American Physical Society ²⁷ , copyright (2012).....	10
Figure 2.2: Acoustic rectification by Boechler et al. ³² in the weakly nonlinear regime. The nonlinear resonance of a localized defect mode is only excited in one direction due to the broken mirror symmetry. Energy is transferred through nonlinearity to lower frequency propagating modes when the defect mode is excited. Reprinted by permission from Macmillan Publishers Ltd: Nature Materials ³² , copyright (2011).....	18
Figure 3.1: (Top) Picture of the experimental setup used in the tunable stiffness experiments (chapter 6). (Bottom) Schematic of the Experimental Setup. Each of the different parts of the experimental setup are indicated with text. We use the different input and output channels of the Lock-In amplifier to both excite and monitor the state of our system. The physical setup consists of an array of spherical particles aligned between two boundaries. In the schematic the boundary conditions are considered as fixed boundary conditions. The particles are supported by polycarbonate rods and are excited using piezoelectric actuators (green). These actuators can be both embedded in particles in the array and placed at the end of the array. Measurements are taken using either dynamic force sensors, static strain measurements, or velocities from the laser vibrometer (red). The voltage signals that need to be processed are indicated in blue. Each part of this setup is described in the following section.	24
Figure 3.2: Schematic of the experimental setup used for the essentially nonlinear frequency bands, chapter 8.....	31
Figure 4.1: A schematic representation of a periodic orbit in a system with two degrees of freedom, position, and velocity. The solid line indicates a closed limit cycle orbit while the dotted line shows that changing the initial condition to a point slightly off the orbit results in a orbit that is not closed. The variational matrix, V , describes this sensitivity.	40
Table 4.1: IEEE Notation for derivation of the electromechanical coupling for piezoelectric disks embedded between two half spheres.....	46
Figure 4.2: A schematic of the embedded piezoelectric element and connected circuit. Under certain conditions the electromechanical coupling can be ignored and we can assume voltage is proportional to the applied force ³⁴ . However, in many applications such as energy harvesting, the dynamics of the electrical circuit becomes essential.	47

Figure 4.3: Experimental Analysis of the Resonant Defect Particle. (a) The schematic of the experimental characterization system. (b) A comparison between the theoretical and experimental transmission spectra for the system in (a).	51
Figure 4.4: Experimental Fits to determine Numerical Parameters. (Left) Fit of the static response of the chain to Hertzian Force Law. (Right) Fit of the linear amplitude response of the defect to a Lorentzian to determine the linear dissipation of the chain.....	52
Table 4.2: Model Parameters (A_1 , A_{10} , masses, τ are experimentally measured).....	53
Figure 5.1: A schematic illustrating defect induced local modes and resonant defect tunability. (a),(c), and (e), represent the lattice subject to lower compression, while (b),(d), and (f) represent a higher compression. (a) and (b) show a mode due to a small defect (green) that is highly localized and does not change its profile between low (a) and high compression (b). (c) and (d) show that the mode due to a larger (red) defect is less localized and still does not depend on compression. (e) and(f) show a mode created by a resonant defect (red) in which the localization can be tuned to from highly localized to completely delocalized. (g) illustrates the origin of this tunability. The small (green) and large (orange) defect frequencies maintain a constant proportion with the band cutoff frequency, resulting in an unchanged localization. In the case of the resonant defect (red) frequency, this constant proportionality is not prescribed. Thus, compression changes the spatial profile of a resonant defect mode.	55
Figure 5.2: The acoustic band and defect mode profile evolution. The color scale shows the steady state amplitude at the embedded force sensors as a function of the frequency and the static compression (a) next to the defect and (b) at the crystal's edge. The defect mode, around 6.2 kHz, appears in the force sensor at the crystal's edge only after the band edge rises above the frequency of the defect mode (at 4 N). The mode's frequency increases very slightly as the lattice is compressed. The dotted curve is the theoretical edge of the acoustic band. (c),(d), and (e) show the local mode profile measured at three different compressions (0.3 N, 0.9 N, and 4.8 N), which are indicated as dotted vertical lines in (a) and (b). At higher compressions, shown in (e), the mode transitions to being completely extended and the dynamics are delocalized. The measurements are performed for half of the chain and we plot their mirrored image of the other half for clarity.....	58
Figure 5.3: Tunable Localization of a resonant defect mode. (a) Localization factor predicted analytically (solid line) for an infinite lattice and calculated computationally for a 31 particle chain (dashed line). Three horizontal dashed lines (i), (ii), and (iii) show localizations for different defect diameters, 11.1 mm, 14.3 mm and 17.5 mm, respectively. In addition, all parameters used in the computation are the derived from the experimental setup. The inset in (a) is an enlarged view, showing the deviation of the computational and analytical results close to the when the defect frequency and band edge meet. (b) The experimentally measured localization and a fit (red line) to the analytical prediction. Each experimental run is shifted along the compression axis to have the same zero point. The inset shows the mode profile used to measure the experimental localization for the run indicated by the arrow.	60

- Figure 5.4: Resonant Defects in Hexagonal Lattices. The normalized mode profile due to a resonant defect (red) placed in a two dimensional hexagonal lattice (grey). We plot the amplitude of the particles displacement in the nearest neighbor direction, \mathbf{a}_1 . The mode becomes less localized as it goes from low (a) to high (b) isotropic compression. 61
- Figure 5.5: Ultraslow velocity wave propagation. (a) A design proposal for achieving tunable ultraslow acoustic or phononic propagation. (b) The wave velocity of the high frequency narrow band waves in the schematic shown in (a). These results were numerically calculated by applying Bloch conditions to the six particle unit cell. 62
- Figure 5.6: Phonon Band Structure for a two dimensional hexagonal lattice . (a) The 2-D band surface with associated cuts (b) along high symmetry directions of a hexagonal lattice. This figure illustrates the acoustic transverse and longitudinal phonon bands. 64
- Figure 5.7: Analytical model. (a) A schematic for the analytical model including relevant parameters..... 64
- Figure 5.8: Tailoring the Resonator Design. (a) The effect of varying defect parameters on the mode frequency. The results for three resonant masses, m_r (solid lines) and one m_0 (dashed line). The arrow shows increasing m_r . (b) The localization of the defect mode for the same parameters shown in (a). For $m_0 < m_s$ (dashed line) the mode never delocalizes but asymptotically approaches the value of the localization for a mass defect of equivalent size, m_0 . The three vertical dashed lines indicate the compression at which the modes delocalizes when $m_0 < m_s$ 70
- Figure 6.1: Tuning stiffness through thermal expansion. **a.** Schematic diagram of the tunable stiffness mechanism illustrated in a 1-D granular chain. The diagram shows the static force on the lattice due to a prescribed displacement while harmonically driving the defect mode. As the lattice is compressed (blue arrow), the defect vibrational amplitude decreases (red arrows). This results in a negative incremental stiffness due to thermal contraction of the defect mode. **b.** Changes in the driving frequency and amplitude of the excitation control the incremental stiffness, and **c.** the strain point at which the stiffness is being modified. The curves are offset for clarity. 75
- Figure 6.2: Response of the nonlinear defect mode. **a.** Theoretical defect mode (blue) and acoustic band (green) frequencies' dependence on prescribed displacement. Experimental measurements are plotted as red dots with the four curves in panel **b** marked with black crosses. **b.** Normalized experimental velocity of the defect mode as a function of displacement of the lattice. Curves correspond to excitation frequencies of 10(blue), 10.5(green), 11(red), and 11.5 kHz (cyan). **c.** Experimental velocity of the defect mode for drive amplitudes of 4.2 (blue), 9.8 (green), and 15.4 nm (red) all at 10.5 kHz. **d.** Numerical results corresponding to **c**, for defects driven at 20, 50, and 80 nm, respectively. Our simplified model (see Methods) qualitatively reproduces the experimental results, but is unable to make precise quantitative predictions. 78
- Figure 6.3: Experimental tuning of the incremental stiffness. Force- displacement curves for excitation amplitudes of **a.** 5.9 nm **b.** 6.4 nm **c.** 7.54 nm **d.** 10.9 nm. Shown

- below are the defect mode velocities (proportional to the mode amplitude, $A(x)$) as a function of the overall displacement, x , of the lattice. 79
- Figure 6.4: Theoretical Investigation. **a.** Map relating the excitation parameters with the modified incremental stiffness and displacement point. **b.** Zero frequency band gap obtained by choosing excitation parameters corresponding to zero stiffness for the lattice. The blue and green line show the force transmitted with the defect drive on and off, respectively. The dotted red line shows the band edge frequency, f_c . When the drive is on, there is a band gap, and when the drive is off the lattice acts as a linear spring. **c.** Force-displacement relationships of the system when it is driven above the bifurcation amplitude. The presence of a tunable hysteresis allows the system to be used as a tunable damper. **d.** As the drive amplitude increases past the bifurcation, the hysteretic losses per cycle increase. The highlighted points correspond to the results in **c.** The inset in **d** shows the hysteresis in the defect vibration amplitude as the lattice is compressed cyclically. 80
- Figure 6.5: Transient Analysis. **a** Time constants that dictate the speed of the relaxation back to steady state. **b** As the system approaches a bifurcation, the amplitude response becomes steeper, and **c** the stiffness is modified more significantly. This is accompanied by longer relaxation time constants, which limits the speed of the system. 85
- Figure 7.1: (a) Schematic of the experimental setup where the chain's length is varied between 1 and 50 beads. For 1 and 2 bead systems there was no embedded sensor. (b-d) The experimental bifurcation dynamics in a 15 bead chain statically compressed at 8 N and driven at 7.3 kHz. (b) The linear transfer function measured using a white noise excitation. The dotted line at 6.8 kHz indicates the band cutoff frequency measured at the half power point of the last peak. The drive frequency (7.3 kHz) for the force time series in (c) is therefore in the band gap. (c) The force time series measured at the end of the chain shows how the bifurcation results in the amplitude growth and stabilization. (d) The power spectral density (PSD) of the red portion of the force signal in (c) shows that energy is transferred from the drive frequency, $f_d = 7.3$ kHz, to two new frequencies, f_N . We study how this bifurcation results from the finite size of a 1-d system. 90
- Figure 7.2: Color maps of the experimentally measured RMS velocity [mm/s] of single bead (a) and two bead (b) systems as a function of the drive amplitude and frequency. The velocity is measured in the second bead for the two bead system. The dotted line in (a) indicates the maximum at each drive amplitude. This clearly displays the mode softening to lower frequencies as the amplitude of the excitation increases. The insets show cross sections at increasing drive amplitudes. The asymmetry and the mode softening is a result of the nonlinear Hertzian contact interaction. The measurements are taking using a lock in amplifier to reduce noise. In addition, the low amplitude response is used to estimate the dissipation coefficients used in the one and two bead computational results. Panels (c) and (d) are the computational counterparts to (a) and (b). The system depends sensitively on the initial compression, F_0 , and the diagrams are fit to have the same linear (low amplitude) frequency as the experimental plots. This

- corresponds to a 8.67 N static compression for the single bead and 4.36N for two beads. 93
- Figure 7.3: The experimental nonlinear resonance and bifurcation behavior of a single bead driven at 6.85kHz. (a,b) The velocity of the bead (a) before and (b) after the bifurcation. (c) The maximum velocity measured at each drive amplitude. (d) The corresponding PSD of two time series, showing the dominant subharmonic frequency at $f_d/2$. (e) the Poincaré section of the dynamics of the bead before (red, central points) and after (blue, side points) the bifurcation. The splitting of the section from one point to two points is characteristic of a period doubling subharmonic bifurcation. Panels (f) and (g) are the computational plots that correspond to the experimental panels (c) and (d). (g) The PSD clearly shows that a sub-harmonic bifurcation occurs after the critical amplitude is crossed. 95
- Figure 7.4: Experimental nonlinear resonance and quasiperiodic bifurcation behavior in a system of 2 beads driven at 6.94kHz. (a,b) The velocity of the second bead (a) before and (b) after the bifurcation. (c) The corresponding PSD of two time series, showing the new frequencies f_{N1} and f_{N2} supported by the nonlinearity of the system, where $f_{N1} + f_{N2} = f_d$. The PSD of the time series clearly show that energy is transferred from the drive frequency, f_d , to the two new frequencies. (d) Poincaré sections of the dynamics of the second bead before (red, central point) and after (blue, surrounding points) the bifurcation. This Poincaré shows the classic intersection of a torus and a plane for quasiperiodic dynamics. The finite number of points is due to the finite length of the signal. (e) The PSD of the computational time series taken at the drive amplitudes indicated in (f) and using the same parameters as measured during the experimental runs. 97
- Figure 7.5: The experimentally measured bifurcation tongues observed in (a) one bead and (b) two bead systems. The color scale corresponds to maximum velocity amplitude (dB), and it demonstrates that as the mode moves further from its linear frequency, the change in dynamics becomes more drastic. The numerically calculated tongue edge is plotted directly on top of the experimental data as a black dotted line. c) and d) show the computational results for 1 and 2 bead chains, respectively (the units are non-dimensional). The solid points indicate where a bifurcation has occurred (i.e., a FM has left the unit circle). Red points indicate that gaps have opened between beads. The dashed rectangles indicate the parameter range for which the experimental measurements in (a) and (b). The vertical dashed lines correspond to the Floquet diagrams in (e-g). We show the unit circle to guide the eye. 101
- Figure 7.6: The interplay between finite size and dissipation. The points indicate a critical bifurcation amplitude, calculated using numeric. In (a) we hold the dissipation of the system constant ($Q=27$) and vary the size of the system. The individual tongues begin to overlap and the bifurcations begin to occur at higher amplitudes. In (b) the finite size ($N=15$) is held constant and the dissipation is varied. For lower dissipations the bifurcation tongues start at lower amplitude. All units shown are non-dimensional. 105
- Figure 8.1: Experimental time series of the force at the dynamic sensor at (a) $f = 10$ Hz and $A = 3.951 \times 10^{-7}$ m and (b) $f = 500$ Hz and $A = 3.775 \times 10^{-7}$ m. 109

Figure 8.2: Experimental time series of the force at the dynamic sensor at (a) $f = 3000$ Hz and $A = 3.408 \times 10^{-7}$ m and (b) $f = 5000$ Hz and $A = 3.75 \times 10^{-7}$ m.	111
Figure 8.3: Experimental Power Spectral Densities of the force time series of (a) Fig. 8.1b: $f = 500$ Hz, and (b) Fig. 8.2a: $f = 3000$ Hz.	112
Figure 9.1: (Left) PV diagram for a traditional thermal machine such as a steam engine. (Right) We propose an energy harvesting system inspired by a thermal machine, in which the constituent harvesting is now a nonlinear hysteretic spring.....	115
Figure 9.2: (Left) Force-displacement for the hysteretic damping mechanism observed in a granular crystal. (Right) The nonlinear amplitude response of the defect mode that results in the force-displacement relation to the left.	116
Figure 9.3: The string-cantilever system. (Left) The vibration coordinate of the string is defined as $z(t)$. (Right) The coordinate of the cantilever is defined as $x(t)$. As the amplitude of the string vibration increases there is an additional tension pulling on the cantilever.	118
Figure 9.4: The displacement of the cantilever modulates the resonance frequency of the string. (Left) This results in a amplitude response for the string that is modulated by the cantilevers displacement, and (Right) a force-displacement relation for the cantilever that has a similar hysteresis to a thermal machine.....	120
Figure 9.5: Cantilever (Top Left) time series and string (Top Right) time series. The string is driven by a harmonic signal, while the cantilever causes a slow variation of the resonance frequency. (Bottom Left) String time series for the high amplitude solution. (Bottom Middle) String time series for the low amplitude solution. (Bottom Right) String time series showing the transient dynamics.....	121
Table 9.1: Example of common mechanical energy sources for small energy harvesting/scavenging. Source: "Piezoelectric Energy Harvesting Devices for Low Frequency Vibration Applications" Dongna Shen, PhD Thesis, Auburn University (2009)	125
Figure 9.6: Experimental setup for a Spherical Bead Compressed Against a Piezoelectric Actuator. (a) A prototype schematic for the proof of concept energy harvesting device. This is mathematically represented in eq. 1. (b) An embedded piezoelectric sensor acts as a high impedance voltage source.	125
Figure 9.7: Nonlinear Detuning and Parametric Energy Harvesting. a, The parametric tongue separating regions of low and high amplitude oscillations for a single sphere particle. We would like to test the indicated cycle as a mechanism to collect mechanical energy. Initially the system would start at (1). By removing energy the system loses amplitude (2), causing the system to retune (3). This causes the amplitude to increase (4) until the nonlinearity again detunes the system (upper dotted arrow). b, The detuning of the natural frequency of the nonlinear spherical particle serves to stabilize and the dynamics. At higher amplitudes, the natural frequency decreases. (colorbar units are in dBs)	127
Figure A.1: Analytical modeling of the system. a Initial lattice with no deformation. The lattice consists of a chain of particles, where the central particle is a defect having a mass M smaller than the rest of the particles. The defect interacts with the neighbors through a nonlinear force $F_i(\delta_t)$, where δ_t is the total distance separating the defect and the neighbors. b Deformed lattice. The lattice boundary	

has been displaced by an amount x . **c** Simplified system used in the analytical approximation. For each fixed displacement value x , the interaction potential between the defect and the neighbors is approximated by a third order polynomial $F\delta$, where $\delta = \delta_t - \delta_0$, δ_0 being the equilibrium distance between the defect and the neighbors in the deformed lattice with no defect drive. All the other beads in the chain are approximated by two linear springs K_C , with K_C calculated independently for each deformation value x . **d** Simplified system with the defect in motion. The defect is displaced from equilibrium by an amount u_d . The two neighboring beads are statically pushed away from it by an amount Δ due to thermal expansion. 141

- Figure A.2: Analytical predictions and comparison to numerical results. **a** Defect response obtained by numerically integrating the equations of motion for the full system. **b** Defect response predicted by the analytical model **c** Force- displacement relation of the material obtained through numerical integration **d** Force-displacement relation obtained analytically. All panels are calculated for an excitation frequency of 10.5 KHz at increasing excitation amplitudes..... 145
- Figure A.3: Stiffness tuning to positive infinity. **a** Stiffness numerator corresponding to a power law potential $F = 1p\delta tp$ as a function of the exponent. Calculated for a chain of 9 particles with $\delta T = 1$. Parameters are $M = 1$ and $b = 0.025$. **b** Force-displacement curves for a 9-particle lattice with a power law interaction force exponent $F = Ap0.5$, $A = 5600$. The exponent 0.5 is indicated as a red dot in **a**. The curves correspond to an excitation frequency of 10.5 KHz and increasing excitation forces. **c** Map relating the applied excitation frequency and amplitude to the stiffness, for the same system as **b**. In all panels the interaction force law is assumed to be equal between all neighboring particles. For **b** and **c**, the defect's mass and damping are the same as in Fig A.2. 147
- Figure A.4: The displacement response of 1st, 3rd, 5th, and 7th beads of a 10 bead homogeneous chain under harmonic excitation with frequency in the attenuation zone. All units are non-dimensional. 150
- Figure A.5: The displacement response of the 10-bead homogeneous chain under harmonic excitation with frequency in the attenuation zone: (a) Response of the first bead superimposed to the excitation, and (b) detail of (a). All units are non-dimensional..... 151
- Figure A.6 (Color online) the displacement response of first bead of a 10-bead homogeneous chain with varying normalized excitation frequency and fixed normalized excitation amplitude equaling unity (dynamics deep inside the attenuation zone). All units are non-dimensional. 155
- Figure A.7: Spatial variation of permanent precompression (δ_y) in a 20 bead chain when the dynamics is deep in the attenuation zone. All units are non-dimensional..... 156
- Figure A.8: Correspondence between analytical and numerical response of the 2-bead system when the dynamics is in the attenuation zone. All units are non-dimensional..... 157

Chapter 1

INTRODUCTION

This research began with the idea that bifurcation phenomena in granular chains could be used to design materials to more efficiently harvest background vibrational energy. At times, this goal seemed out of reach. While the potential impact of granular mechanics on energy harvesting came in and out of focus, the research continued along a path that explores dynamical phenomena, some of which includes bifurcations, tunable band gaps, localized modes of lattices, tunable stiffness, finite size effects, and even vibrational bifurcations in guitar strings. In the end the research returned and finished with proposals for energy harvesting in nonlinear systems.

1.1 Motivation

Nonlinearity is ubiquitous and while oftentimes associated with damage or unwanted effects, it is also responsible for many of the remarkable phenomena found in materials. Thermal expansion occurs when atoms or molecules increase their average spacing due to an increased vibrational amplitude, a nonlinear effect arising from an asymmetric interaction potential^{1,2}. The equipartition of energy requires that modes interact nonlinearly, exchanging energy³. If interactions were purely linear the equipartition would not occur and materials would not relax to a thermal equilibrium. Umklapp phonon scattering is inherently nonlinear and significantly influences the thermal conductivity at higher temperatures. The above examples demonstrate that nonlinearity has some clear benefits: energy can be transferred between modes and frequencies, the natural frequencies of the system may depend on strain or other external

conditions^{4,7}, and the response of a nonlinear system can become extremely sensitive to varying parameters⁸. By leveraging these effects, we can look to use nonlinearity to design materials with targeted properties.

A fundamental theme of materials science is in understanding how materials derive properties from their structure. This could be how the different microstructures affect the Young's modulus and toughness, the effect of grain size on a solid's hardness⁹, or how the crosslinking in a polymer affects its viscoelastic response. We are interested in another example of structure: materials with broken periodicity. Periodicity is the regular arrangement of atoms, particles, or other repeat unit on a lattice. In a truly periodic material this regularity repeats forever, which leads to remarkable phenomena such as frequency band gaps¹⁰. These band gaps prevent the propagation of waves in material and can be used to reflect or localize energy¹¹. The discrete nature of periodicity leads to wave dispersion, in which different frequencies travel at different wave speeds.

Real materials are not completely periodic: there are grain boundaries to crystals, defect impurities, and an inherently finite size. This leads to a broken periodicity in which there is no longer complete translational symmetry. These imperfections in the periodicity of materials have an enormous effect on material properties and are a reason for the many interesting phenomena and effects in materials. A few examples of how defects affect material properties include electrical conductivity in semiconductors¹², thermal conductivity of graphene¹³, and mechanical strength of carbon materials^{14,15}.

More recently, the concept of periodicity has been extended in the context of metamaterials¹⁶, in which a periodic structure is engineered at a mesoscale into the system. So instead of looking for a material with a specific property, the goal is to tailor the structure of local interactions for particular properties. In mechanics, this resulted in materials with unexpected and extreme properties, including negative effective mass and modulus¹⁶⁻²¹. Since the scale of the engineered repeat units are larger than atomistic, the assumption of infinite size does not necessarily hold.

We expand ideas from metamaterials research by looking at nonlinearity as a different mechanism to tune material properties. In this thesis we look at granular crystals, a macroscopic array of nonlinearly interacting spherical particles where nonlinearity is introduced in the local interaction between granular particles. By arranging the particles in a one-dimensional array we can study a system with periodicity similar to that found in other materials. In a granular crystal, the nonlinearity originates from a change in the contact area as the neighboring particles are compressed²². This nonlinearity can be tuned across a complete range, encompassing linear, weakly nonlinear, and strongly nonlinear dynamics.

The finite size, mass defects, and resonant defects of granular crystals leads to broken periodicity. Nonlinearity in systems with broken periodicity is not well understood and offers an enhanced control over the vibration dynamics and propagation of waves in these structures. By using structural nonlinearity, we can design materials with extreme tunability. Although nonlinearity in other materials is oftentimes considered secondary, we study the physics that originates from the interaction of nonlinear localized modes with the extended modes of the

acoustic band of the granular crystal. This research acts as a model for designing nonlinearity into materials for targeted, extreme, and unusual properties.

1.2 Goals and achievements

We describe new ways to use nonlinear modes for enhanced control over the propagation and localization of mechanical energy. In addition, we show how nonlinearity and defect modes can be used in practical applications such as fully tunable stiffness and energy harvesting. We use the one-dimensional granular crystal for theory and experiments as a model system with nonlinearity, discreteness, and broken periodicity.

A significant portion of this research is related to nonlinear dynamic responses, i.e., how weak and strong nonlinearity can be used to alter frequency band gaps and wave propagation²³⁻²⁶. The dynamics in this research project expand the complete range of nonlinear responses, starting from near linear and going to completely nonlinear and non-smooth.

We start by studying dynamics in the linear limit, where resonant defect mode profiles can be externally tuned from localized to completely delocalized. This is the first theory and experimental observation of defect modes that can be externally controlled, eliminating the need to replace a defect due to changing application demands. This is in direct contrast with modes introduced by mass defects, in which the localization typically depends on the size of the defect and cannot be altered later²⁷. The simplicity of the physical model extends the impact of these results and potential applications to other material systems.

In the weakly nonlinear dynamical regime, we demonstrate how driving localized modes can be used to control macroscopic properties, providing the first example of fully tunable stiffness. By using the highly sensitive nature of nonlinearity combined with the thermal expansion we tune the incremental lattice stiffness to arbitrary values at any point on the force-displacement relation.

We also demonstrate how mechanical filters based on periodicity break down due to relatively weak nonlinearities at finite sizes. While previous work had examined this effect in diatomic granular chains, where the instability was connected to nonlinear discrete breather solutions^{28,29}, we show this instability in homogenous granular crystals. As the size of the granular crystal decreases the presence of instabilities increases and energy is more readily transferred between frequencies. We explore how bifurcations and energy transfer depend on the damping, finite size, nonlinearity, and breakdown of evanescent waves. Because energy is transferred to new frequencies that are in the propagating band of the system, the bifurcations affect wave propagation and result in the breakdown of mechanical filtering, which relies on frequency band gaps³⁰⁻³². We show how this dynamic response holds even when the dynamics become non-smooth and gaps open up between particles.

In the strongly nonlinear regime we explore frequency bands gaps in granular crystal that exhibit no linear speed of sound and therefore no linear coupling stiffness³³⁻³⁵. Since frequency band gaps in linear media are derived from the coupling stiffness, it is not necessarily clear how band gaps exhibit themselves in essentially nonlinear systems, where there is no possible linearization. While the dynamics are strongly nonlinear and quite different from linear media,

we demonstrate that the waves propagate as separate pulses instead of harmonic waves, and that the concept of a band gap still holds.

Studying the weak nonlinearities in granular crystals led us to propose two new models for energy harvesting. In the both models a nonlinear oscillator is driven intentionally to instability. Instability causes non-conservative forces in the system to no longer balance, i.e., dissipation no longer balances the energy driven into the system. As the system departs from its steady state solution, there is more energy being injected into the system than dissipated. By holding the system in this instable region one could efficiently transfer energy between the source and harvester without altering the state of the system, presenting a new paradigm for nonlinear energy harvesting systems.

1.3 Structure of the thesis

This thesis is a collection of self-standing articles of nonlinearity in systems with broken periodicity^{26,36,37}. The articles span from nearly linear dynamics, in which the nonlinearity enters as a tuning parameter, to the essentially nonlinear limit.

Chapter 2 presents the necessary background information and a review of previous literature in nonlinear granular chains. In chapter 3, we provide an overview of all the experimental and computational tools used in each experiment. Since the experimental setups for the self-standing results are similar but distinctly different, we first present a detailed description of experimental tools and their function and then describe the distinct experimental setups. In chapter 4, we follow the same structure as chapter 3, but for modeling tools. The following chapters discuss the results and potential applications of the work. In chapter 5, we start by

studying dynamics in the linear limit, where resonant defect mode profiles can be externally controlled. This is the first theory and experimental observation of defect modes that can be externally controlled, eliminating the need to replace a defect due to changing application demands. In chapter 6, we study the tuning of a lattices mechanical response using driven defect modes, providing the first example of fully tunable stiffness. By using the highly sensitive nature of nonlinearity combined with the thermal expansion we show the first example of how lattice stiffness can be tuned to arbitrary and extreme values at any point on the force displacement relation. In chapter 7, we demonstrate how mechanical filters based on periodicity may break down due to relatively weak nonlinearities at finite sizes. In chapter 8, we explore frequency bands in strongly nonlinear wave propagation. In chapter 9, we finish by presenting applications of the nonlinear dynamics in two models for energy harvesting. Although the two approaches aim to solve different problems in energy harvesting, both rely on pushing the dynamics into regions of nonlinear instability for more efficient energy harvesting.

Chapter 2

BACKGROUND INFORMATION

Periodic structure is found in many materials and systems. It is the regular arrangement of atoms, particles, or unit cells which results in both dispersion and band gaps. Due to the possibility of enhanced control over wave propagation, these remarkable properties have fed the growth of fields such as photonics^{11,38,39} and phononics^{40,41}. In addition, it is the periodic structure that allows scientists in photonics, phononics, and semiconductors to take inspiration from each other's previous work.

As a mathematical construct, periodicity continues ad infinitum. However, real world systems are not infinite, and the spatial periodicity of a lattice ends at some point. In atomic systems, the idea of periodicity can only be maintained if the grain size of a crystal is significantly large enough. In macroscopic systems, there is a similar problem. How big is big enough? Can we consider a system of 2, 3, or 4, or even a hundred repeating units as periodic? This finite size has a significant effect on the frequency band structure that originates from periodicity.

Granular crystals are an example of a nonlinear periodic mechanical structure, which is inherently finite and may have defects. In the following sections I present a review on media with broken periodicities, focusing on the literature for granular crystals and proceeding from nearly linear to strongly nonlinear.

2.1 Linear

Wave dispersion, in which the wave velocity depends on frequency¹⁰, is a result of the discreteness of a periodic system. This is in direct contrast with most continuous media waves which are typically non-dispersive, meaning the wave speed is constant and the frequency and wavelength are determined by the well-known relationship, $c = \lambda f$. In discrete media long wavelengths do not 'sense' the discrete nature of the media. However, when the wavelength grows shorter and begins to approach the size of the lattice spacing, the discreteness becomes extremely important. This dispersion causes wave packets with finite bandwidth to spread out spatially.

In addition, periodic media does not support wave propagation at all frequency ranges. Bands of frequencies that are exponentially attenuated and reflected are called band gaps. In 1987, the idea of a band gap inspired the field of photonics, where the original interest lay in using periodic dielectric materials for localizing and trapping light^{11,38}. In 1993 Kushwaha et al. presented the concept of acoustic bands in periodic composites⁴² and in 2000 Lui et al. demonstrated this in a sonic crystal as a method to reflect propagating sound¹⁷. In addition, phononic crystals are being used to enhance control over high frequency sound and heat⁴³. In periodic mechanical systems, such as the granular crystal, frequency band gaps have been introduced as a passive filtering mechanism^{30,31}.

In a monoatomic or homogenous 1D system, in which all particles are identical, there is a single acoustic band. Figure 2.1a shows a schematic of the acoustic band, indicated in red, for a homogenous granular crystal. The acoustic band rises up to a frequency that depends on the coupling stiffness and masses in the lattice. Above this cutoff frequency waves are reflected and do not propagate. The phase velocity, defined as the velocity of each frequency

component, $v_p = \omega(k)/k$, decreases for increasing frequency, a consequence of dispersion. The speed of sound of the discrete media is defined by the long-wavelength approximation.

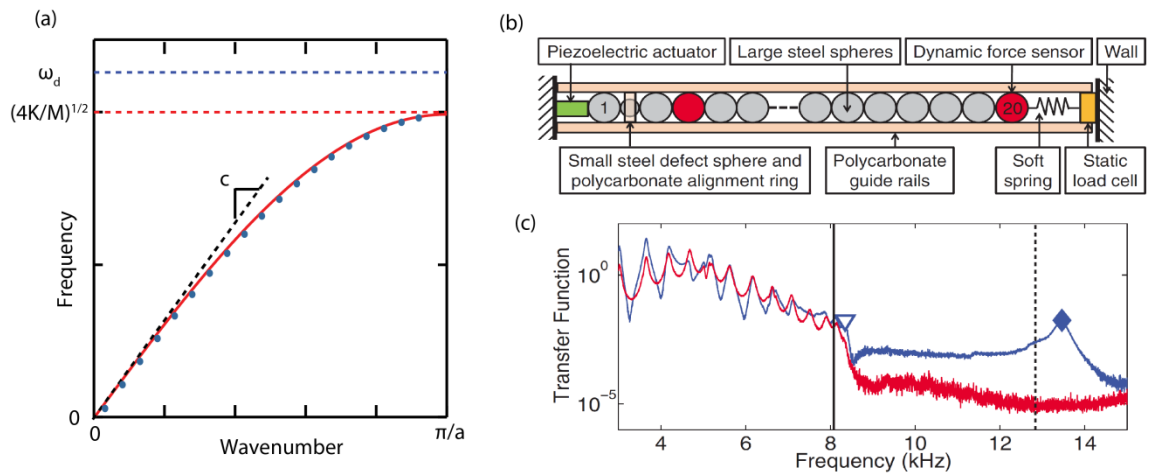


Figure 2.1: a) Schematic for the acoustic band (red) of a monoatomic granular crystal. Effects of broken periodicity, finite size, and a defect mode are shown in blue. The long wavelength speed of sound is shown as the tangent as the wavenumber approaches zero (black). b) Setup by Man et al.²⁷ to measure (c) the linear acoustic band and localized defect mode in a finite, 20 particle long, chain. Reprinted pending permission from American Physical Society²⁷, copyright (2012).

Broken periodic symmetry affects the frequency bands primarily in two ways: through finite size and defects. Finite size limits the number of degrees of freedom, so what previously was an acoustic band with an infinite number of modes becomes a collection of a finite number of modes with frequencies up to the acoustic band edge. This is schematically shown in Figure 2.1a. Because the system is no longer infinitely periodic, all waves are not completely reflected. Instead the system filtering rolls off, with the imaginary component of the wavenumber also affected. As the lattice gets smaller the filtering effects are reduced, and the discreteness play a larger role. While Man et al. explored defect modes in a linear finite granular crystal, they also

presented the finite size effects in the linear monoatomic chain. The transfer function in Figure 2.1c shows the individual resonant peaks, and the localized defect mode.

Defects have an enormous effect on material properties: electrical conductivity in semiconductors¹², thermal conductivity¹³, and mechanical strength^{14,15} are just a few examples. These effects may be due to a strain the defect imposes on the lattice, impurity scattering, or even defect-defect interactions. In otherwise periodic materials, defects destroy the lattice's translational symmetry and alter the fundamental modes of the system, which carry propagating wave information. Localized modes may result from a defect in an otherwise periodic media⁴⁴⁻⁴⁷. As briefly mentioned above, periodicity leads to frequency band gaps that do not support propagating waves. Therefore, if a mode exists in this forbidden frequency range, it will be spatially confined, i.e., any energy at this frequency cannot travel in either direction and will be locally trapped. In granular crystals, when a mass defect is smaller than the other particles in the lattice it may result in a defect mode, where the mode frequency and spatial profile depend only on the mass ratio between the defect and the rest of the lattice²⁷. Man et al. provides an approximation to finding the frequency of the localized mode using a reduced three particle model. In our analysis for local to extended transitions using resonant defects³⁷, we provide an analytic approach to finding the frequency and spatial profiles for weakly localized waves, in which the three particle approximation breaks down.

Acoustic and mechanical metamaterials have been proposed for protecting structures against low frequency waves, by engineering sub-wavelength structures as local resonances. In these materials the locally resonant structure can be approximated as a frequency dependent effective mass⁴⁸. At certain frequencies the effective mass appears negative and this causes a

low frequency band gap to open. This was designed in granular crystals as a proof of concept and has also been shown in other structures with local resonances as a means to control wave speed^{19,49-51}.

2.2 Weakly nonlinear

Nonlinearity affects a broad range of disciplines and describes the response of real systems, for example, the amplitude dependence of a simple pendulum⁵², the reaction-diffusion in biological systems⁵³, the butterfly effect in weather systems⁵⁴, the synchronization between fireflies⁵⁵, and the contact law for spheres compressed against each other²². Frequently in applications nonlinearity is either essential to how a device works or how it breaks down. Here we look at nonlinear effects and then at how they manifest themselves in nonlinear lattices.

2.2.1 Introduction to nonlinear phenomena

Almost all systems have some sort of frequency dependence. In linear system theory, this is embodied in the transfer function of a system, and in materials science this frequency dependence presents itself in variety of ways: two examples are the band gaps in periodic materials or the plasma frequency of a metal. But until now we have disregarded any notion of a dependence on amplitude. This is where nonlinearity becomes essential.

Nonlinearity describes how a system, e.g., a material's force response, a child's swinging, or a stress wave, depends on amplitude⁸. This is in direct contrast with a linear response, in which the force-displacement, or stress-strain relationship, is amplitude independent. However, when

the incremental change in spring constant, stiffness, or modulus are no longer constant but depend on the excitation amplitude, the system is characterized as nonlinear.

The idea of nonlinearity should be somewhat familiar. In mechanics we typically think of this as originating from one of two sources, either a constitutive nonlinear response or a geometric nonlinearity. Rubbers, foams, and carbon nanotube foams⁵⁶ present examples of materials with constitutive nonlinear responses. In these examples the material microstructure results in the nonlinearity, and the material does not follow Hooke's Law under compression or tension. For example, a foam's densification causes an overall increase in the stiffness of the material. For contrast, a geometric nonlinearity develops through a change in the geometry. An example of this occurs for a beam in axial compression. As the compression is increased, there is a point where the boundaries can no longer be ignored and the beam would rather bend than undergo further compressive strain⁵⁵. This causes a change in the incremental stiffness. Granular crystals present a geometric nonlinearity when two spheres come into contact²². Initially the contact is a point. As the beads are compressed the contact area grows and the stiffness correspondingly increases²². Due to either geometric or constitutive effects, nearly all mechanical responses becomes nonlinear at high enough amplitudes. Therefore nonlinear systems and their dynamics are an essential part of our physical world.

But nonlinear systems are also quite difficult to study. Many of the mathematical tools used to study linear systems are no longer available: linear superposition of states does not apply, tools from Fourier analysis which rely on linear transnationally invariant systems are no longer accessible, and in some cases multiple solutions to the same problem exist. Nonlinear systems are relatively difficult to fully characterize and even more difficult to use in an engineering

application. However, nonlinearity presents dynamics that are not accessible in linear systems that could allow for new applications and designs.

One particular advantage of nonlinear systems over their linear counterparts is the ability to transfer energy between modes at different frequencies^{52,57}. In optical systems this led to sum frequency generation⁵⁷ and is used today in mechanical systems for nondestructive evaluation techniques and failure prediction^{58,59}. The nonlinearity communication between modes allows them to exchange energy⁵², and nonlinear wave mixing has been used for granular crystals for acoustic logic elements⁶⁰. We show how energy transfer between modes can lead to the breakdown of finite size periodic mechanical filters.

Weakly nonlinear dynamics are characterized by a smooth transition from linear dynamics in which a perturbation scheme presents an appropriate method to solving the problem. In dynamical nonlinear systems, such as the classic nonlinear Duffing oscillator or a granular crystal, this can be seen as a slow transition away from the linear dynamics. The system is initially linearized at some point, but as the amplitude of oscillations grow, the potential is not strictly harmonic (i.e., not linear) and higher order terms become important. As oscillation amplitudes grow resonance responses become asymmetric and the amplitude can change rapidly due to small system changes.

2.2.2 Weakly nonlinear lattices

Up until now I have presented nonlinearity and periodicity as two separate phenomena. However in a granular chain, the lattice we study, these two phenomena meet. Before introducing a granular chain, it is important to present a brief overview of the different

nonlinear lattices that have been studied, influential problems and results, as well as the approaches to solving these problems, and follow up with a discussion of how our research in granular crystals fits in among these other mechanical lattices.

Initially, interest in nonlinear lattices primarily grew from two distinct events: the first observation of a soliton in 1834 by John Scott Russell, and a surprising computational experiment by Fermi, Pasta, and Ulam more than a hundred years later^{61,62}. A soliton is a type nonlinear wave that travels at a constant velocity, maintaining a constant spatial profile⁶¹. John Scott Russell first observed this type of wave in a shallow water channel and followed the pulse for miles before he finally lost it. This inspired some of the initial work on nonlinear waves⁶³. The constant spatial profile of the wave is achieved through a system that has both nonlinearity and dispersion⁶⁴. Because nonlinear lattices contain both these properties they can also support this class of unique waves. The nonlinearity has a tendency for higher amplitude waves to travel faster, causing a steepening of the wave, while dispersion, due to the discrete nature of the lattice, tends to spread out a wave packet. When these two phenomena balance a soliton results. In granular crystals, solitary waves have been extensively studied and were first proposed by Nesterenko using a long wavelength approximation for the discrete granular chain³⁵.

The computational result by E. Fermi, J. Pasta, and S. Ulam in 1955 examines the energy transferred between the modes of a simple mass spring lattice, with a weakly nonlinear nearest neighbor coupling. They initialized the system with a long-wavelength oscillation, and expected the system to effectively thermalize by distributing its energy over all modes, a consequence of ergodicity. Instead, they found energy transferred to the other modes of the system, but

periodically returned back to the initial mode. This was later explained in the context of solitons breaking up and coming back together by Zabusky and Kruskal in 1965⁶⁵. Together, the discovery of solitons and this computational result inspired significant interest in the dynamics of 1-D discrete lattice systems. Important for our purposes, the granular lattice can be approximated by dynamics in a the weakly nonlinear FPU type lattice⁶⁶.

However, even in perfectly periodic systems many of the dynamics depend on the underlying lattice. One way nonlinear lattices can differ is due to different coupling potentials, e.g., the 6-12 Lennard Jones Potential, the Morse Potential, or the potential from a magnetic dipole interaction. In the weakly nonlinear limit this results in Taylor expansions with different coefficients. An additional significant differentiating factor is how the nonlinearity enters. In a lattice of pendulums coupled through torsional springs, the nonlinearity appears as a geometric nonlinearity at each pendulum site. As the pendulum swings to larger amplitudes the linear approximation breaks down. The nonlinearity is not in the coupling, but in an onsite potential introduced at each lattice point. This type of lattice can be characterized as a Klein-Gordon lattice and can be written as,

$$\ddot{u}_i = k(u_{i-1} + u_{i+1} - 2u_i) + V'(u_i). \quad (2.1)$$

Other lattices, such as the Fermi-Pasta-Ulam(FPU) lattices or the Toda lattice, may have no onsite potential but instead the lattice is coupled through nonlinear springs. The granular lattice that we study fits into this second category. These can be written as,

$$\ddot{u}_i = V'(u_{i+1} - u_i) - V'(u_i - u_{i-1}), \quad (2.2)$$

Where u_i represents the displacement of the particle at lattice site i , k is a coupling parameter, and V is either the onsite potential for the Klein Gordon lattice or the coupling potential for the FPU lattices.

In driven weakly nonlinear crystals, there has been extensive study of physics previously predicted in FPU lattices, including phenomena related to broken lattice periodicity⁶⁷. Marin et al. discuss the effects of finite size on discrete breather instabilities, a type of localized modulation instability in diatomic chains^{28,29}. They discuss how shorter lattices increased the magnitude of the instability. Boechler et al. demonstrated discrete breathers in a diatomic granular chain⁶⁸, and explored stability in the different dynamical regimes⁶⁶. In diatomic granular chains Hoogetboom et al looked at the hysteresis loop that occurs when driving the system past a bifurcation⁶⁹. Theocharis et al. looked at the stability of nonlinear localized impurity modes that resulted from mass defects⁷⁰. Finally, Boechler et al. used a granular crystal with a local defect mode and broken mirror symmetry to engineer an acoustic rectifier³². This design was based on using local resonances to transfer energy to lower frequency propagating modes (Figure 2.2). These dynamics are for the granular crystal in the weakly nonlinear regime with a broken periodicity due to either defects or finite size.

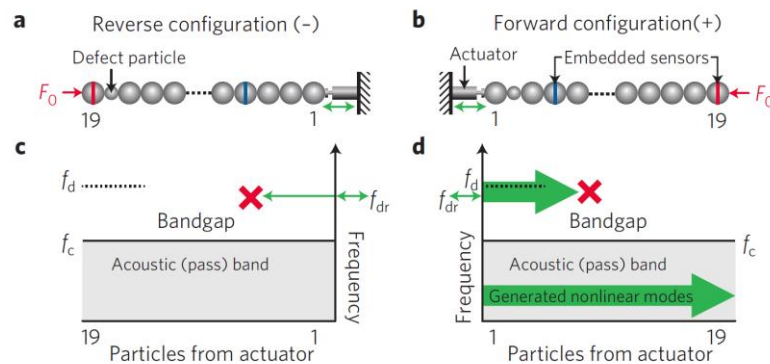


Figure 2.2: Acoustic rectification by Boechler et al.³² in the weakly nonlinear regime. The nonlinear resonance of a localized defect mode is only excited in one direction due to the broken mirror symmetry. Energy is transferred through nonlinearity to lower frequency propagating modes when the defect mode is excited. Reprinted by permission from Macmillan Publishers Ltd: Nature Materials³², copyright (2011).

2.3 Strongly nonlinear

In weakly nonlinear systems, a common approach is to initially linearize the system and then use a perturbation analysis to study the effect of increasing amplitude when nonlinear terms cannot be ignored. In contrast, strongly nonlinear systems cannot be studied through a perturbation scheme. The dynamics are drastically different from the linear case and must be approached differently. In the granular crystal this can easily be seen when the system has no initial pre-compression. The Hertz law is piecewise continuous at this point and is essentially nonlinear. The granular crystal in the absence of pre-compression has no speed of sound, i.e., a sonic vacuum³³. Nesterenko shows how this leads to the inability for acoustic waves to propagate, but instead energy propagates as highly localized pulses^{71,72}.

One key advantage of granular crystals is that they present both weak and strong nonlinear dynamic responses³⁵. The granular crystal can be tuned to have an effectively linear response (at high pre-compressions), weakly nonlinear response (at intermediate pre-compressions), or essentially strongly nonlinear response (in the absence of pre-compression). This tunability, i.e., the variability of their dynamic response, has attracted significant interest to the granular crystal system, especially in its ability to propagate solitary waves^{35,73} and be used as a shock absorbing

protection⁷⁴. This has been extended to two dimensional granular crystals as a mechanism for controlling the directionality of wave fronts⁷⁵.

In granular crystals with broken periodicity the work can be separated into either driven dynamics or solitary wave propagation interacting with defect or boundaries. Jayaprakash et al. examined the time periodic nonlinear normal modes in finite size, essentially nonlinear granular chains⁷⁶. The exploration of solitary waves interacting with broken periodicity began with Nesterenko studying the breakup of a solitary wave at the boundary between two different essentially nonlinear media⁷². Daraio et al. experimentally investigated this in an array of granular chains adjacent to an array of stainless steel spheres^{74,77}. Job et al. have studied how solitary waves in essentially nonlinear granular chains interact with boundaries⁷⁸ and localized mass defects⁷⁹. Especially interesting in this case of the mass defect is that because the interactions are strongly nonlinear, the mass defect can oscillate at frequencies higher than the incident wave spectrum.

2.4 Energy harvesting

The nonlinear phenomena that we just explained present a host of advantages over linear systems. They have the ability to transfer energy between frequencies, to show amplitude dependent behavior, and to go through sharp bifurcation transitions. In many energy harvesting these differences could mean new paradigms for harvesting systems with significantly greater efficiency.

Energy harvesting is the practice of converting ambient energy, i.e., energy sources that are nonconventional, small, and or broadband, into a more usable form. In vibrational energy

harvesting, ambient vibrations are typically converted into electrical energy by using coupled piezoelectric devices or some other electromechanical coupling^{80,81}. While linear systems have been a good first step, recent nonlinear designs suggest leveraging nonlinearity could lead to greater efficiencies.

The traditional approach is to enhance the total energy harvested by matching the linear resonant frequency of the piezoelectric mass system with the resonance of the mechanical structure. This then causes an increase in the strain on the piezoelectric, a voltage across the terminals, and the possibility for energy to be transferred. In this approach the dynamics are completely linear. This allows for easy implementation, but does not necessarily address some of the inherent differences of energy harvesting, for which a linear system is not ideally suited. Roundy talks about the general approach of defining efficiency in electromechanical harvesting systems⁸¹, while Anton and Sodano review the application and implementation of piezoelectric energy harvesting⁸².

A main issue in energy harvesting is that sources are not ideal energy sources; they are both not harmonic and not infinite in size. Linear systems are inherently limited by a quality factor bandwidth relationship. When the damping of the system is high the harvesting occurs better over a broader frequency range, but also now has more internal damping. When the damping is low, the energy harvester harvests only from a narrow range of frequencies⁸³.

Nonlinear systems have the possibility of overcoming this limitation, since in nonlinear systems energy can be transferred between frequencies. This has inspired a broad range of interest in the field of nonlinear energy harvesting. For highly broadband signals, Cottone,

Vocca, and Gammaitoni presented an seminal approach based on a bistable duffing oscillator in which noise is converted to higher amplitude motion as the system jumps between two stable minima^{84,85}. Here the authors show that this bistable system has the possibility to effectively convert energy from a noise signal to a resonance through stochastic resonance. Although the authors include electromechanical coupling in the equation, the effect is negligible for the parameters chosen. The nonlinear mechanics of similar systems have been subsequently studied⁸⁶⁻⁸⁹. A different approach is based on driving a Duffing oscillator into its high amplitude state⁹⁰. This approach relies on tuning the device to follow the resonant frequency of excitation and requires that the electrical coupling be small enough to stay in the high amplitude state.

In general in the nonlinear energy harvesting community, the energy sink that is introduced by electrically coupling the electrical system to the mechanical is swept to the side or ignored. However, this is inherently one of the most important pieces to the problem; damping affects amplitude, and in nonlinear systems, the amplitude affects the state of the device operation and solution. In addition, by ignoring electromechanical coupling, or choosing poor weak back coupling, the energy harvesting device is doing inherently bad. In this case the energy in the mechanical system is not being effectively transferred to the electrical load.

We present two nonlinear mechanical systems to address some of the limitations and problems in vibrational energy harvesting. Both ideas are based on pushing a system into an instability in order to create transient dynamics. When the dynamics of the system are transient and the amplitude of the solution grows, there is a mismatch between the neoconservative forces. This

allows us to use electrical dissipation to move the system from an unstable state to a stable one and harvest this additional energy. This is presented in chapter 10.

Chapter 3

EXPERIMENTAL SETUP

The majority of the experimental tests have a similar setup with different measurement and excitation techniques depending on the particular experimental goals. In this section I present the basic experimental setup, the recurring measurement techniques, and the more subtle differences required for each experiment.

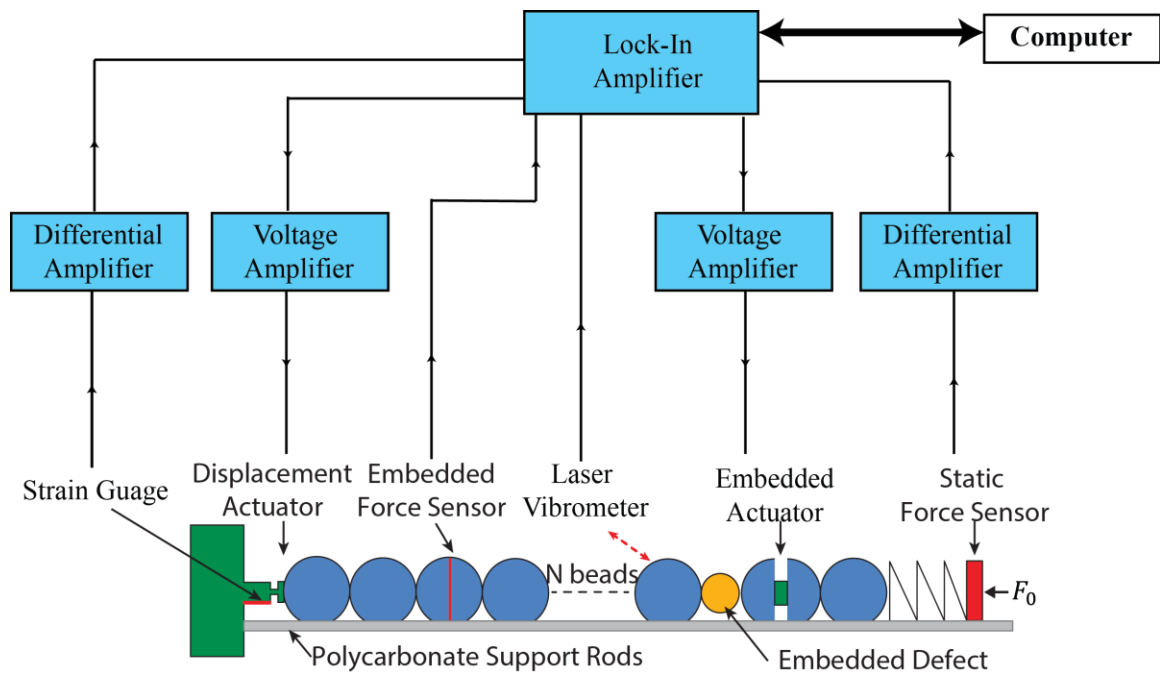


Figure 3.1: (Top) Picture of the experimental setup used in the tunable stiffness experiments (chapter 6). (Bottom) Schematic of the Experimental Setup. Each of the different parts of the experimental setup are indicated with text. We use the different input and output channels of the Lock-In amplifier to both excite and monitor the state of our system. The physical setup consists of an array of spherical particles aligned between two boundaries. In the schematic the boundary conditions are considered as fixed boundary conditions. The particles are supported by polycarbonate rods and are excited using piezoelectric actuators (green). These actuators can be both embedded in particles in the array and placed at the end of the array. Measurements are taken using either dynamic force sensors, static strain measurements, or velocities from the laser vibrometer (red). The voltage signals that need to be processed are indicated in blue. Each part of this setup is described in the following section.

3.1 General experimental setup and tools

The 1-D granular crystal is a periodic array of grains or particles³⁵. In our system our repeat unit particle is a stainless steel type 316 sphere (McMaster-Carr) with a measured radius $R = 9.525 \text{ mm}$, measured mass $m = 28.84 \text{ g}$, Youngs Modulus $E = 193 \text{ GPa}$, and Poisson ratio $\nu = 0.3$.⁹¹ These particles are aligned using two polycarbonate rods and are fixed between a piezo-electric actuator and a force sensor or soft spring which provide fixed or force controlled boundary conditions, respectively. The overall mechanical structure and support of the system is similar to previous experimental studies of granular crystals^{27,31,32,68,69}.

Most of the dynamics that we are interested in are either nonlinear resonances or linear resonances, and all the experimental studies include a harmonic drive source. It is therefore extremely important to be aware of the different frequency responses and resonances of the building blocks of the system, nearby noise sources, and also the measurement tools. The masses and coupling stiffness between particles leads to an acoustic band up to 7kHz when compressed at 10 N. Since our system is nonlinear the actual frequencies of interest change depending on the initial compression. I present these numbers as a baseline to keep in mind

which frequency ranges we are interested in. The principal mode of vibration of a single bead will be much higher ($\sim 30\text{kHz}$) than the dynamics we are interested in. This can therefore initially be ignored. In addition the steel blocks, acting as a boundary condition, and the supporting table have resonances at low frequencies, less than 1 kHz. These resonances can be ignored when studying systems at higher frequencies but must be either filtered or accounted for when the frequencies of interest are lower.

In the experiments, it is important to always consider the boundary conditions and how this may affect the involved dynamics. We have two primary methods to apply an initial compression to the granular chain. One boundary will always be a stiff wall. This could be a force sensor or a piezoelectric actuator attached to a large steel block. The important thing to consider here is that the piezoelectric actuator or force sensor is stiffer than the Hertzian contact stiffness. In this configuration the boundary condition is displacement controlled. The second boundary condition that we use is a soft spring, to allow more control over the static compression of the chain. In this configuration, the soft spring should be many orders of magnitude lower than the contact stiffness, and the boundary condition is considered to be a force controlled boundary.

The choice piezo actuator has inherent tradeoffs. We utilize a variety of piezo actuators that are chosen to either excite or displace the system. The resonances of the piezo stack actuators should always be chosen so that the frequency response of the actuator is flat over the excitation range and the resonance is far above the band or spatially separated from the dynamics. This means that the larger displacement actuators (with resonances at 3-4 kHz) should only be used to compress the system when studying dynamics localized at a distance

from the actuator. Smaller displacement actuators used for excitations should have resonances high above the band ($\sim 30\text{kHz}$) and be driven using amplifiers designed for high impedance capacitive loads.

We use polycarbonate rods of 6.4 mm radius to support and align the granular particles. The polymer rods have two important considerations. The first is to reduce the coupling between the stainless steel particles and the supporting structures. The choice of polymer rods instead of steel rods enhances the impedance mismatch. The second consideration is low friction. Although the particle displacements are quite small, the velocities are significant. It is therefore important to reduce frictional dissipation mechanisms that are external to the granular crystal. These may be highly variable and also difficult to predict and quantify.

3.2 Measurement tools and techniques

In the granular chain we have three different measurement tools including, static load cells, dynamic force sensors, and a laser vibrometer, to study the dynamics of the system. Each of these tools have advantages, limitations, and important considerations.

The static load cells (Transducer Techniques SLB-25 and Omega LCMFD-50N) rely on a wheatstone bridge technology. This is the circuit for a strain gauge that relies on a constant voltage source and outputs a small differential voltage in response to strain which can be translated directly to force. The voltage is amplified using a differential amplifier and then filtered using a low pass 4th order filter, in order to reduce high frequency noise. As is indicated by their name the static load cells should not be used under dynamic loading conditions. The primary function of the static load cells in the granular chain is to measure the

initial static compression of the system. Due to the nonlinearity of the system, the dynamics change from weakly nonlinear to strongly nonlinear depending on which compression regime the experiments are performed. It is therefore important to monitor the static force in the granular crystal.

We use two types of dynamic force sensors. One is a commercial quartz sensor (PCB 208C01) and the second is an embedded piezoelectric disk⁷⁷. The commercial sensor has a corresponding signal conditioner which uses a current source to amplify the signal at the source, thus minimizing noise problems. Therefore the commercial sensor is desired when possible, but due to its size we implement it only at the ends of the chain. The piezoelectric sensor is smaller and can be embedded in particles for in-situ force measurements. The disadvantage is the low voltage signal in response to strain. The voltages can be quite low and are subject to noise problems. We therefore use lock-in amplifiers and filtering techniques to gain accurate amplitude and phase information for the signal. Finally, when measuring or amplifying the piezo signal it is important to have a high input impedance compared to the relatively high impedance of the piezo. We present an extended description of the dynamics of this device in section 4.2.2.

We use a Doppler laser vibrometer (Polytec CLV-2534) to measure the velocity of the beads. The primary advantage of this technique is that it is completely non-invasive, meaning the measurement does not affect the dynamics of the granular chain. We assume that the motion of the particles is completely aligned with the chain, with no off-axis component. Using this assumption, the measured velocity is just the particles velocity projected onto the laser measurement direction. The laser can be translated to sequentially measure velocities of

different particles in the chain. We use the laser vibrometer with an internal low pass filter at 100KHz and a high pass filter at 100Hz. For our experiments the laser vibrometer is used in conjunction with a lock-in amplifier, therefore measuring the steady state velocities. This provides an advantage in providing information not only about the amplitude of a harmonic signal, but also phase information. This phase information allows us to relate the steady state velocities of neighboring particles and therefore image the steady state amplitude profile (i.e., the mode profile) over the entire chain with a single measurement tool.

The measurements are digitized and subsequently analyzed using either a data acquisition board (National Instruments NI-6115) or a lock-in amplifier (Stanford Research Systems SR830 or Zürich Instruments ZI-HF2LI). The data acquisition board (DAQ) from National Instruments provides an ideal way to measure transient and non-harmonic dynamics of the system. The DAQ board measures time series of the waveform and can measure changes due to a system bifurcation and features of the waveform when it is not sinusoidal. The measurements across channels are simultaneous and each channel has its own analog to digital converter, allowing high time resolution without suffering any cross-talk between channels. In addition, the device has 12 bit resolution, allowing for better amplitude resolution than many 8 bit oscilloscopes.

The lock-in amplifier acts as a very powerful measurement tool to gaining information about a steady state response. This measures the sinusoidal characteristics of a system by computing the Fourier component at a reference frequency. The principal function is to output a amplitude and phase of a voltage signal with respect to a reference wave. This allows us to sweep over frequency or another variable of our system and watch how the system response

changes. This works well to see the linear response of the chain and the nonlinear bending of modes. In addition, since we know the phase relation of neighboring particles we can plot experimentally measured modes. The downside of using a lock-in amplifier is the time needed to get accurate measurements. The lock-in operates by multiplying the reference signal and measured voltage signal and low pass filtering, i.e., integrating. This prevents us from observing the transient dynamics and is therefore limited to the steady state response. In addition, it means that the total settling time is related to the time constant of the low pass filter. We must integrate long enough to allow both the system and the lock-in dynamics to settle. Typically in our measurements we use a time constant on the order of, $\tau \sim 30 \text{ ms}$, and a 4th order filter. This is sufficiently long enough to measure the steady state dynamics at $3 - 15 \text{ kHz}$.

3.3 Specific experimental setups

3.3.1 Local to extended transitions of resonant defect modes

For this experiment (results in chapter 5), we introduce a resonant defect in the granular chain by attaching an external ring structure to one of the particles⁴⁹. This structure has a mechanical resonance measured experimentally at 6.2 kHz . We embed this resonant defect in the center of a 31-particle chain, with 15 stainless steel spheres (type 316, 9.525 mm radius) placed on both sides of the resonant defect. This is a one-dimensional finite crystal with a defect in the center. The particles are aligned between a $90 \mu\text{m}$ compression actuator (Physik Instrumente P-841.60) and static force sensor (Omega LCMFD-50N). A laser vibrometer (Polytec OFV-534) sequentially measures velocities of half the chain and the defect particle. Embedded force

sensors are placed next to the defect and at the end of the chain. All dynamic measurements are taken at steady state using a lock-in amplifier (Zurich Instruments ZIHF2LI). We drive the defect's resonating mass and measure the forces and velocities of different particles in the lattice.

During the experimental analysis, we measured the defect mode's velocity profile at each static compression and then used this profile to calculate the mode's localization. During this compression, we follow the entire mode's evolution and can observe the transition from a localized to a delocalized mode.

3.3.2 Extraordinary stiffness tunability

The experiments are carried out on a 1-D lattice of 9 spheres of 9.525 mm (results in chapter 6). We replace the central bead by a defect bead with a radius of 4.763 mm, and we replace the bead next to the defect by a piezoelectric actuator (Physik Instrumente PD050.31) held between two stainless steel cylinders with a radius of 10 mm and a length of 4 mm.

The amplitude of vibration is measured using a laser Doppler vibrometer (Polytec CLV-2534) pointing at the particle next to the defect, and the compression force is measured using a static load cell (Omega LCMFD-50N) and amplified with a gain of 100. The electrical outputs from the sensors are measured with a lock-in amplifier (Zurich Instruments ZI-HF2LI). The strain on the lattice is prescribed using a high-stroke piezoelectric actuator (Physik Instrumente P-841.60). The force-displacement curves are obtained at a steady state by waiting 1.5 seconds to ensure quasistatic behavior.

3.3.3 Nonlinear resonance in finite granular chains

We assemble a one-dimensional (1D) homogeneous granular chain made of N stainless steel spheres between an excitation actuator and a soft spring (results are in chapter 7). We excite the system with a harmonic displacement for approximately 400 ms, enough time to reach stationary dynamics, using a low voltage piezoelectric actuator (blocking force 800 N, resonance frequency 40 kHz, PST 150/5/7 VS10 provided by Piezomechanik). The actuator is mounted on a steel block fixed to the table. N spheres (with N ranging between 1 and 50) are then aligned with the head of the actuator and supported by polycarbonate rods. We excite with a range of static and dynamic loading that allows access to both the weakly and strongly nonlinear dynamical regime. We use a non-contact laser vibrometer to measure the dynamic response of the short granular systems (i.e., $N \leq 2$) at the last bead, ensuring no effects of the measurement system on the results. In longer systems, we use calibrated sensor particles, placed in the third and last bead, similar to Job et al.⁷⁸ The applied static load is measured using a calibrated static force sensor.

3.3.4 Essentially nonlinear frequency bands

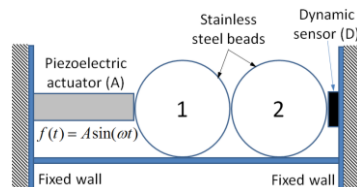


Figure 3.2: Schematic of the experimental setup used for the essentially nonlinear frequency bands, chapter 8.

In this experiment, we consider a system of two beads placed between a dynamic sensor (PCB 208C01) and a piezoelectric actuator (PST 150/5/7 VS10)⁹² (Fig. 3.2). The actuator is used to harmonically excite the first bead. The dynamic force sensor measures transmitted force and is used to infer the dynamics and state of the system, i.e., whether the system is driven in a strongly or weakly nonlinear regime. We adjust the offset bias of the actuator to achieve dynamics at near zero static compression.

Chapter 4

MODELING

4.1 Discrete particle model for the granular chain

We model the granular crystal as an array of masses and springs coupled by a nonlinear Hertzian contact law^{22,93}. The Hertzian contact law defines the force, F , needed to achieve a certain overlap, δ , between two compressed spherical particles,

$$F = A\delta^{3/2}. \quad (4.1)$$

The Hertzian contact factor, A , is a function of spheres radii, R_i , Youngs modulus, E_i , and

Poissons ratio, ν_i , for the materials of the two particles, $A = \frac{4}{3} \left(\frac{1-\nu_i^2}{E_i} + \frac{1-\nu_j^2}{E_j} \right)^{-1} \left(\frac{R_i R_j}{R_i + R_j} \right)^{1/2}$.

The exponent of 3/2 is caused by a geometric nonlinearity. At zero compression the spheres are in contact at a single point. However, as two particles are compressed, there is an increase in the contact surface area. This causes an increase in the incremental stiffness and results in the nonlinear force interaction^{22,94}.

4.1.1 Hamiltonian approximation

The complex features of wave propagation in an array of spherical particles can be greatly simplified by considering a simple mass spring model. Nesterenko first used this model in granular media to predict solitary waves³⁵, where the nonlinearity and dispersion necessary for the formation of these waves are provided by the nonlinear contact and the periodicity, respectively. Each point mass is equivalent to the mass of the spheres and the nonlinear

springs are described by the Hertzian force law. This allows us to write an equation of motion for each of the beads displacements (4.2), u_i , using Newton's second law for inertia, where each bead is subject to a force due to each adjacent bead³⁵,

$$m_i \ddot{u}_i = A_i \delta_i^{3/2} - A_{i+1} \delta_{i+1}^{3/2}, \quad (4.2)$$

where δ_i is the overlap of two adjacent beads and can be described in terms of their neighboring equilibrium positions and an initial static overlap, δ_0 ,

$$\delta_i = \delta_0 + u_{i-1} - u_i. \quad (4.3)$$

This discrete particle model seems like an oversimplification of the dynamics that occur in the real system but can be supported if each mass can be considered a point mass. The assumption is valid only as long as none of the internal resonances of the spheres are present. This is equivalent to having the spheres' first structural resonance frequency high above the dynamic range of interest. Below this frequency, the sphere moves as a rigid body and can be considered a point mass. It is important to check this assumption. When the internal resonance frequency of the single particle is low enough the internal resonances of the particle cannot be ignored. Interest in metamaterials in granular systems is based on this concept, in which materials gain remarkable properties by designing each periodic unit to have an internal resonant structure⁴⁹. In fact, our study of tunable localized modes in periodic media relies on an internal resonance which interacts with the normal extended modes of the system.

4.1.2 Nonconservative elements

In our experiments the dynamics are not Hamiltonian, but are instead a driven damped system. This means that we need to add nonconservative terms to the Hamiltonian system presented above. To account for the damping that is inherently present in real systems we add a linear dissipative term, $m_i \dot{u}_i / \tau$, where τ is a linear dissipation time constant. This linear dissipation time constant can also be measured through a non-dimensional quality factor, $Q = \omega_0 \tau$, where ω_0 is the linear resonance frequency, or using the exponentially decaying envelope of the signal oscillation. In cases when there are mass defects and the dissipation of all the particles becomes important, it may be more appropriate to use a mass normalized dissipation, $b \dot{u}$, where $b = m_i / \tau$. This leads to a modified equation of motion,

$$m_i \ddot{u}_i = A_i \delta_i^{3/2} - A_{i+1} \delta_{i+1}^{3/2} + m_i \dot{u}_i / \tau. \quad (4.4)$$

In order to include the non-conservative inputs signals, we consider the nature of the excitations. In our system all the excitations are provided by piezoelectric elements that are nearly two orders of magnitude stiffer than the Hertzian contact interaction. Therefore we assume that the piezoelectric actuator can expand freely, and that the excitation is a displacement controlled signal. To model this we modify the local overlap of the contacts,

$$\delta_i = B_i \cos \omega_d t + \delta_0 + u_{i-1} - u_i. \quad (4.5)$$

This notation can be used to represent a moving wall or an expanding piezoelectric actuator between two particles, and has the effect of adding or removing energy from the system depending on the relative phases of the drive and particle motion.

4.2 Linear eigenanalysis and state space

Most of the dynamics that we explore are weakly nonlinear. It is therefore good to start by understanding the linearized system. By taking an appropriate linearization of the equations of motion (4.2), assuming oscillatory solutions for the particles, $\mathbf{u}_i = e^{i\omega t}$, and ignoring dissipation, we can formulate an eigenvalue problem^{70,95},

$$-i\omega^2 \mathbf{M}\mathbf{u} = \mathbf{K}\mathbf{u}, \quad (4.6)$$

where ω is the frequency of the oscillation, \mathbf{M} is the diagonal mass matrix describing the system, and \mathbf{K} is stiffness matrix describing the coupling between masses in the system. We can then solve this for the eigenvectors (normal modes) and eigenvalues (resonant frequencies) of the system. The extended normal modes of crystal are responsible for propagating wave energy at each of the frequencies. In the infinite system the solution can be found using Bloch conditions, which results in continuous frequency bands⁹⁵. The linearized equations of motion for the granular crystal (4.6) are the same form of equations used to model the acoustic and optical bands for phonons in materials⁹⁵. In finite systems the frequency bands are no longer continuous, but instead there are finite numbers of modes that lie along the continuous dispersion relation.

If dissipation and an excitation are included in the model we can also find a linear transfer function using state space analysis³¹. This numerical technique is a particularly fast and computationally inexpensive route to obtaining the linear response that corresponds to a particular experimental excitation and measurement arrangement. This allows us to numerically observe the band gaps that occur as a result of the periodicity of the lattice. In

addition, because our system has more than one degree of freedom and possibly different dissipation for each particle, fitting the dissipation of a single mode may not accurately represent the dissipation across the lattice. State space analysis can provide a powerful mechanism to fitting to different linear dissipation models.

4.3 Nonlinear modeling: integration and perturbation analysis

4.3.1 Integration

The equations of motion are inherently nonlinear, and therefore must be integrated if we want to predict any of the nonlinear dynamical phenomena. To integrate the equations of motion for n beads, we must transform the n 2nd order ODEs into a system of $2n$ first order ODEs⁹⁶. The integration allows us to observe and predict bifurcation phenomena, transient dynamics, and mode bending. We use two integration schemes, either a 4th order Runge Kutta or the MATLAB ode45 function. For both integration schemes, it is essential to choose tolerances or time-steps that are small enough, ensuring that energy is conserved and/or that the integration captures the interested dynamics. Generally we use a time step of 50 ns in the 4th order Runge Kutta. In the matlab solvers, we use a relative tolerance of 1e-4 and an absolute tolerance of 1e-14. As solutions get close to bifurcation points, it may be necessary to significantly increase the accuracy by reducing the tolerance or integration time step.

4.3.2 Perturbation analysis for limit cycle solutions

A significant portion of this research involves studying the phenomena close to instability points or when dynamics are unstable and go through a bifurcation. In general the equations of motion can be recast into a system of 1st order ordinary differential equations of the form,

$$\dot{\mathbf{x}} = \mathbf{h}(\mathbf{x}, \dot{\mathbf{x}}, t) \quad (4.7)$$

where \mathbf{h} is a vector function describing the dynamics of the evolution and \mathbf{x} is the solution. In our case the equations depends on time because there is an external forcing. In the limit of small excitations, far from any bifurcations, the solution to our system is periodic with the same period of the excitation. Dissipation will cause any of the transient signals to decay and the steady state response will be at the excitation frequency. Therefore our system settles to a periodic orbit. Limit cycles are a closed periodic orbit in a systems phase space, and Floquet analysis is a tool that enables the study of the stability of limit cycle orbits. As the system's amplitude grows beyond the linear limit, nonlinearity grows in importance. The nonlinearity can cause the stable periodic solution to suddenly become unstable and result in a wealth of new dynamics. Floquet analysis can tell us the stability of the limit cycles and when a limit cycle becomes unstable, what new dynamics may appear. This tool is a linear perturbation analysis tool from the periodic limit cycle. It therefore also gives us insight into how fast the system reacts to perturbations^{8,28}.

Algorithm

Floquet analysis has been used in damped driven systems^{28,29,97} and in granular crystals. Normally, one searches for both the period of the limit cycle and the limit cycle itself in phase space. One option to finding the a periodic orbit is to simply integrate the system for long times and wait for the system to approach a periodic attractor⁹⁷. However this does not allow

convergence to the desired attractor and may take a long time. Since in a driven damped system the period may be known beforehand, we can also solve for the limit cycle (see Applied Nonlinear Dynamics Ch. 6.5.2 section on Nonautonomous Systems)⁹⁷. A limit cycle can be defined as a closed periodic orbit, or equivalently,

$$\mathbf{x}(T) = \mathbf{x}^0, \quad (4.8)$$

where \mathbf{x}^0 is the initial condition and T is the period. In Floquet Analysis, we are looking for a matrix that describes the perturbations to the initial condition that satisfies this relation. That is, we are looking to see how the solution one period later responds to a small change in the initial condition, \mathbf{x}^0 . This idea is embodied in a variational matrix, which describes how the sensitivity of the orbit on the choice of initial condition,

$$\mathbf{V}(t) = \frac{\partial \mathbf{x}(t)}{\partial \mathbf{x}^0}. \quad (4.9)$$

When time equals that for a single period $t = T$, the variational matrix describes the deviation of the solution at full period later. This can be more easily envisioned in a two-dimensional system, schematically shown in Fig 4.1, in which the small deviation in the initial condition leads to a non-closed orbit after one period, T .

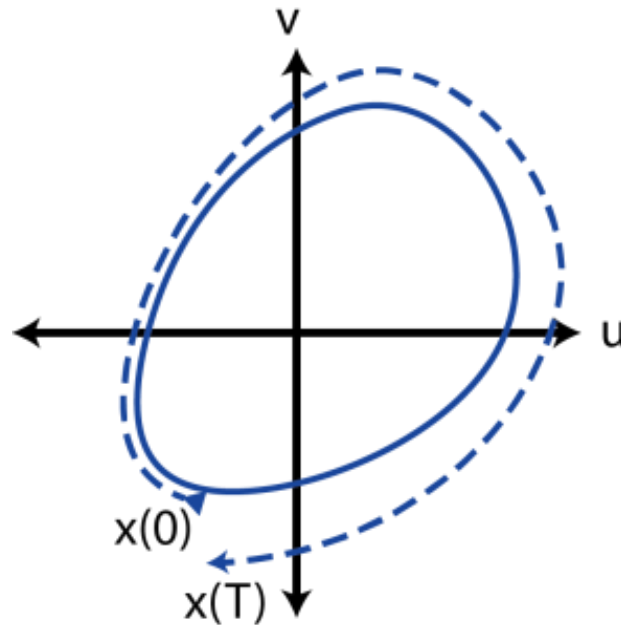


Figure 4.1: A schematic representation of a periodic orbit in a system with two degrees of freedom, position, and velocity. The solid line indicates a closed limit cycle orbit while the dotted line shows that changing the initial condition to a point slightly off the orbit results in a orbit that is not closed. The variational matrix, V , describes this sensitivity.

Since every orbit is not necessarily a closed orbit, and we do not know the initial condition that will provide a closed orbit, we must search for a closed orbit solution. This means finding a solution of map,

$$\mathbf{f}(\mathbf{x}^0) = \mathbf{x}^0 - \mathbf{x}(T) = 0. \quad (4.10)$$

The value $\mathbf{x}(T)$ depends on the integration from the initial condition \mathbf{x}^0 . We begin with an initial guess and then modify that initial guess using Newton's Method until we find the solution that provides a closed orbit,

$$\mathbf{x}_{i+1}^0 - \mathbf{x}_i^0 = \left(\mathbf{J}_n(\mathbf{x}_i^0) \right)^{-1} \mathbf{f}(\mathbf{x}_i^0), \quad (4.11)$$

where \mathbf{x}_i^0 is the approximation of the initial condition \mathbf{x}^0 after i iterations. The Jacobian matrix, \mathbf{J}_n , is for the defined for the function, \mathbf{f} , and is

$$\mathbf{J}_n = \frac{\partial \mathbf{f}}{\partial \mathbf{x}^0} = \frac{\partial}{\partial \mathbf{x}^0} [\mathbf{x}^0 - \mathbf{x}(T)] = \left[\mathbf{I} - \frac{\partial \mathbf{x}(T)}{\partial \mathbf{x}^0} \right] = \mathbf{I} - \mathbf{V}(T). \quad (4.12)$$

$$\mathbf{J}_n = \mathbf{I} - \mathbf{V}(T)$$

The Newtons method then becomes,

$$\mathbf{x}_{i+1}^0 = \mathbf{x}_i^0 + (\mathbf{I} - \mathbf{V}(T))^{-1} (\mathbf{x}^0 - \mathbf{x}(T)) \quad (4.13)$$

which depends on both the solution of the system, $\mathbf{x}(T)$, and the variational matrix, $\mathbf{V}(T)$, after integrating for a full period. The equations to integrate for the system are defined by \mathbf{h} .

However, we need to define the evolution of the variational matrix,

$$\dot{\mathbf{V}} = \frac{\partial}{\partial t} \frac{\partial \mathbf{x}(t)}{\partial \mathbf{x}^0} = \frac{\partial}{\partial \mathbf{x}^0} \frac{\partial \mathbf{x}(t)}{\partial t} = \frac{\partial}{\partial \mathbf{x}^0} \mathbf{h}(\mathbf{x}(t), \dot{\mathbf{x}}, t). \quad (4.14)$$

Since the system of ODE's \mathbf{h} depend on $\mathbf{x}(t)$, which definitely depends on the initial guess, we must apply chain rule,

$$\dot{\mathbf{V}} = \left(\frac{\partial}{\partial \mathbf{x}} \mathbf{h}(\mathbf{x}(t), \dot{\mathbf{x}}, t) \right) \frac{\partial \mathbf{x}}{\partial \mathbf{x}^0}, \quad (4.15)$$

and the first factor in the product is simply the Jacobian of the system \mathbf{h} , and the second factor in the product is the variational matrix itself. Therefore the time evolution of the variational matrix is

$$\frac{d}{dt}\mathbf{V} = \mathbf{J}_{sys}\mathbf{V}. \quad (4.16)$$

Using this we can now perform the Newton method after integrating each initial guess for one full period.

Comments on the resolution and the algorithm tolerance

We integrate the ODE and search for the following condition numerically. However, there is inherently an error to the Newton method in solving this problem. Therefore, we stop the algorithm when the condition for the Newton method is below some tolerance.

$$\mathbf{f}(\mathbf{x}^0) = \mathbf{x}^0 - \mathbf{x}(T) < tol. \quad (4.17)$$

This defines the resolution and accuracy of the time periodic solution for which we are searching. When we are far from a bifurcation this tolerance can be relatively large since the system itself is stable. However, near a bifurcation the system is less stable, and perturbations have the tendency to grow. This means that for the algorithm to converge the tolerance of the integrator may need to be reduced. We typically look for solutions with a tolerance, $tol = 10^{-14}$, which should be compared with the static overlap of the system, $\delta_0 \approx 10^{-7}$.

Comments on the variational matrix

After integrating the variational matrix for a full period we find,

$$\mathbf{V}(T) = \frac{\partial \mathbf{x}(T)}{\partial \mathbf{x}^0}. \quad (4.18)$$

When the system is on a limit cycle the initial condition and final state of the system are equivalent, $\mathbf{x}(T) = \mathbf{x}^0$. This means that the matrix tells us the linear sensitivity that a perturbation has on the final state, where the eigenvalues, λ_i , of \mathbf{V} describe the growth of a perturbation in the associated eigenvector direction. The eigenvalues of the matrix are complex and give us information both about the stability of the limit cycle and when the limit cycle is stable, i.e., the speed of the system^{8,97}. The magnitude of the eigenvalue, $|\lambda_i|$, dictates the growth rate of the perturbation, and the argument tells the frequency of the growing perturbation, $f_N = \text{Arg}(\lambda_i)/(2\pi T)$. When the system is Hamiltonian, multipliers sit on the unit circle in the complex plane. However, when the system is damped, as in our case, the multipliers lie on a circle of with a radius dependent upon the linear dissipation, $e^{-T/(2\tau)}$, where τ is a linear dissipation time constant²⁸. This reflects the notion that transients decay in a dissipative system, and the rate of decay is dictated by this value. A perturbation acts as a small transient. Therefore, when the magnitudes of the multipliers are less than one, perturbations die, and the rate of the exponential approach back to the limit cycle is dictated by the magnitude of the Floquet multiplier. As the magnitude of this multiplier approaches unity, the time constant to return to the limit cycle approaches infinity. At the bifurcation point the time is infinite and the system is sitting on top of a saddle node. A small perturbation does not decay. Finally, when the magnitude is greater than one the perturbation grows exponentially and the limit cycle is not stable.

4.4 Modeling specific tools

4.4.1 Lock-in amplifier

We frequently connect the measurable experimental parameters to a lock-in amplifier. The measured variable could be the velocity of particle i , the force at the boundary, or the force in the middle of a bead. The lock-in amplifier multiplies the measured variable by the sine and cosine at the reference frequency, low pass filters the signal, and outputs the Fourier component of the measured variable at the reference frequency. This process can be modeled using a system of n first order ODEs, where n is the order of the low pass filter and τ is the time constant of the low pass filter of the lock-in amplifier. The ODE for measuring a variable, x_{input} , can be written as,

$$\begin{aligned}
 \dot{y}_1 &= x_{input} * \cos(\omega_{ref}t) - y_1 \\
 \dot{y}_2 &= (y_1 - y_2)/\tau \\
 &\dots \\
 \dot{y}_n &= (y_{n-1} - y_n)/\tau \\
 \dot{y}_{n+1} &= x_{input} * \sin(\omega_{ref}t) - y_{n+1} \\
 \dot{y}_{n+2} &= (y_{n+1} - y_{n+2})/\tau \\
 &\dots \\
 \dot{y}_{2n} &= (y_{2n-1} - y_{2n})/\tau.
 \end{aligned} \tag{4.19}$$

This amplitude, A , and phase with respect to the excitation signal, ϕ , of the measured variable are described by the equations,

$$\begin{aligned}
 A &= 2\sqrt{y_n^2 + y_{2n}^2} \\
 \phi &= \tan^{-1}\left(\frac{y_{2n}}{y_n}\right)
 \end{aligned} \tag{4.20}$$

4.4.2 Embedded piezoelectric sensor

There has been extensive use of an embedded piezoelectric element for sensing purposes^{31,32,68,77}. Two important considerations when using embedded piezoelectric sensors are the input impedance of the measurement device and the frequency of operation. When the impedance between the terminals is relatively large compared to the impedance of the piezo, the force and voltage can be proportionally related. The time constant of the piezoelectric measuring circuit is also important. When using the piezo as a sensing device, the measurement frequency should always be well above the reciprocal of the time constant. If a low resistance is placed in parallel with the piezo, this affects the time constant and accurate sensing is pushed to a higher frequency regime.

Studies on granular crystals have proposed their potential application in energy harvesting devices⁹⁸. For this, the associated circuit and configuration becomes extremely important, and has previously been ignored. The goal is to convert mechanical energy into electrical energy, and therefore the electro mechanical coupling must be incorporated in the equations of motion for the mechanical and electrical systems. I present here equations of motion for the piezoelectric disk embedded in a sphere. These are more generally and do not make assumptions about small strains on the piezo, flat frequency response, or rigid body motion. These equations (or similarly derived depending on differing geometries) need to be checked when considering energy harvesting in a granular chain.

We use a Lagrangian approach, which allows us to derive equations of motion from the constitutive response of a piezoelectric disc and use generalized coordinates, so that the approach can be easily adopted for different circuits or mechanical geometries. The approach closely follows that presented by A. Preumon⁹⁹. The constitutive laws of a piezoelectric disk

$$\begin{pmatrix} D \\ S \end{pmatrix} = \begin{bmatrix} \varepsilon^T & d_{33} \\ d_{33} & s^E \end{bmatrix} \begin{pmatrix} E \\ T \end{pmatrix}, \quad (4.21)$$

can be integrated over the volume, inverted, and then used to define a coenergy function,

$$W_e^*(\Delta, \lambda) = \frac{C(1 - k^2)}{2} \lambda^2 + nd_{33}K_a \lambda \Delta - \frac{K_a}{2} \Delta^2, \quad (4.22)$$

where λ is the generalized coordinate, chosen as the flux linkage across the piezo. The other parameters follow correspond to coefficients as in Preumont's derivation⁹⁹ and the IEEE standards for piezoelectricity¹⁰⁰. They are defined in the table.

ε^T	Permittivity	$k = \frac{d_{33}^2}{s^E \varepsilon^T}$	Electromechanical coupling factor
d_{33}	Piezoelectric Constant	$K_a = \frac{A}{s^E t}$	Short circuit stiffness
s^E	Compliance	t	Thickness
A	Area	$Q = AD$	Charge
D	Charge Displacement	$\Delta = St$	Total Displacement
S	Strain	$f = TA$	Force
T	Stress	$V = Et$	Voltage
E	Electric Field	$C = \frac{\varepsilon^T A}{t}$	Capacitance

Table 4.1: IEEE Notation for derivation of the electromechanical coupling for piezoelectric disks embedded between two half spheres.

The coenergy function can be included in the Lagrangian for the system as,

$$L = T - V + W_e^*, \quad (4.23)$$

where T is Kinetic energy and V is the Potential energy of the system. By defining a kinetic energy and a potential energy of the system presented in the figure below, we can then derive the equations of motion using Lagrange's equations.

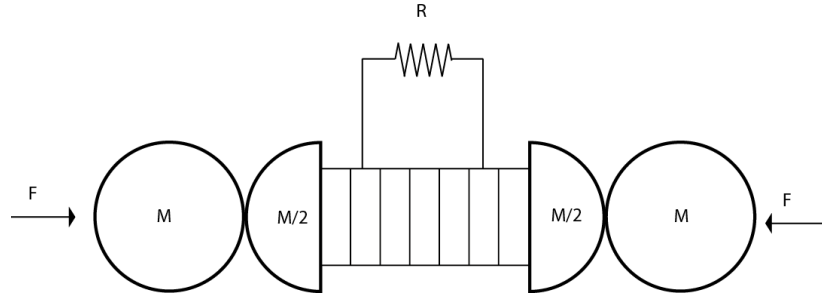


Figure 4.2: A schematic of the embedded piezoelectric element and connected circuit. Under certain conditions the electromechanical coupling can be ignored and we can assume voltage is proportional to the applied force³⁴. However, in many applications such as energy harvesting, the dynamics of the electrical circuit becomes essential.

The figure shows two beads in contact with the central bead with the embedded piezoelectric disk. The coordinates of the two neighboring beads only enter in the equations of the potential of the system, since the equations of motion for these particles can be easily derived from Newtonian mechanics. This leads us to define the kinetic minus potential energy of the system as,

$$T - V = \frac{1}{2}\dot{u}_{2L}^2 + \frac{1}{2}\dot{u}_{2R}^2 - \frac{2}{5}A(\delta_0 - u_{2L} + u_1)^{\frac{5}{2}} - \frac{2}{5}A(\delta_0 - u_3 + u_{2R})^{\frac{5}{2}}, \quad (4.24)$$

where u_1 and u_3 are the equilibrium positions of the two neighboring beads and u_{2L} and u_{2R} are the equilibrium position for the two half beads that are attached to the piezoelectric sensor.

The coenergy function for the piezo is defined above, and all that must be added is a dissipation function for the non-conservative elements,

$$D = \frac{b}{2}\dot{u}_{2L}^2 + \frac{b}{2}\dot{u}_{2R}^2 + \frac{1}{2R}\dot{\lambda}^2, \quad (4.25)$$

where b is the dissipation constant for the mechanical system and R is the electrical resistance. By taking the various derivatives for the Lagrange equations, we can write the full equations of motion describing the electromechanical coupling between the piezoelectric circuit and the two half beads,

$$\begin{aligned} m\ddot{u}_{2L} + b\dot{u}_{2L} &= -nd_{33}K_a\dot{\lambda} + K_a(u_{2R} - u_{2L}) + A(\delta_0 - u_{2L} + u_1)^{\frac{3}{2}} \\ &\quad + b\dot{u}_{2L} \\ m\ddot{u}_{2R} + b\dot{u}_{2R} &= nd_{33}K_a\dot{\lambda} - K_a(u_{2R} - u_{2L}) - A(\delta_0 - u_3 + u_{2R})^{\frac{3}{2}} \\ &\quad + b\dot{u}_{2R} \\ C(1 - k^2)\ddot{\lambda} + nd_{33}K_a(\dot{u}_{2R} - \dot{u}_{2L}) + \frac{\dot{\lambda}}{R} &= 0. \end{aligned} \quad (4.26)$$

These equations of motion fully define the electromechanical coupling. By looking at the mechanical equations of motion it is clear that the circuit acts as an energy sink. When this damping is on the order of the mechanical damping then it may have a significant effect. Inductive damping occurs when there is an additional inductor placed in series with the resistance⁹⁹. This leads to a modified Lagrangian, $L = T - V + W_e^* - W_m$, where $W_m = \lambda^2/2L$ is the energy stored in the inductor. The resulting RCL circuit (and equations of motion) now has its own resonance and can be tuned to couple more or less with the mechanical system.

4.5 Modeling for specific experiments

4.5.1 Local to extended transitions of resonant defect modes

This modeling is for the experimental setup described in section 3.3.1. The results are shown in chapter 5. We model our system as masses coupled by springs with a single defect site. All particles other than the defect are spherical with $R = 9.525 \text{ mm}$ and a mass, $m_s = 28.8 \text{ g}$. The equations of motion are,

$$\begin{aligned} m_s \ddot{u}_i &= k_c(u_{i+1} + u_{i-1} - 2u_i); \quad i \neq 0 \\ m_0 \ddot{u}_0 &= k_c(u_1 + u_{-1} - 2u_0) + k_r(u_r - u_0) \\ m_r \ddot{u}_r &= k_r(u_0 - u_r), \end{aligned} \quad (4.27)$$

where u_i is the displacement of the i th sphere around its equilibrium position. The equations represent a one-dimensional lattice with a local resonance at the defect site. The defect's dynamics are contained in the second two equations, and the rest of the lattice in the first. The defect has a mass located in the chain array, which is $m_0 = 47.8 \text{ g}$, and has a displacement from equilibrium, u_0 . The defect's resonant mass, $m_r = 0.18 \text{ g}$, is coupled with a stiffness, $k_r = 2.64 \times 10^5 \text{ N/m}$, to this particle and has a displacement, u_r . This displacement is the additional degree of freedom for the resonator. We define the characteristic frequency of the resonator, $f_r = \sqrt{k_r/m_r}$, which is totally independent of the lattice, and we stress that this is not equal to the defect mode's frequency. The stiffness coupling of all other particles within the chain is found by linearizing the Hertzian contact law, $k_c = \frac{3}{2} A^{2/3} F_0^{1/3} \left[\frac{N^{2/3}}{\mu m} \right]$, where F_0 is the compression, $A = \frac{4}{3} \sqrt{\frac{R}{2}} \left(\frac{E}{2(1-\nu^2)} \right)$, $E = 193 \text{ GPa}$, and $\nu = 0.3$. This is where the

nonlinear nature of our lattice is important. This allows a change in the coupling stiffness between adjacent particles through compression, while the resonant coupling stiffness, k_r , stays constant. Finally, the boundary conditions are modeled as fixed walls with $u_{-16} = u_{16} = 0$.

The dynamics we are interested in are linear, and therefore we solve the eigenvalue problem that results from assuming oscillatory solutions. In section 5.4 we show our analytical derivation, which is used to fit for experiments and demonstrates that boundary conditions do not become important until just before the mode transitions from local to extended dynamics.

4.5.1.1 Modeling the resonant defect

The resonant defect is essential to our investigation of actively controlled localization, and the defect itself is modeled as two separate parts. To characterize the defect's behavior, we perform a separate experimental and numerical analysis. A portion of the defect particle's mass, m_0 , is localized in the lattice array and coupled to the other particles through the same nonlinear Hertzian Contact. Another part of the mass, m_r , is in the resonating ring. This mass is determined using Finite Element simulations in Comsol Multiphysics®. The spring constant, $k_r = m_r f_r^2$, coupling the masses is calculated using the linear mode's frequency, f_r . This frequency is found by measuring the transmission properties of a single resonator where the frequency f_r is the anti-resonance. A schematic of the experimental setup is shown in Fig 4.3a, with the transmission spectra shown in Fig 4.3b. The blue curve plots the experimental results, and the red curve is the corresponding numerical results from a linear state space analysis.

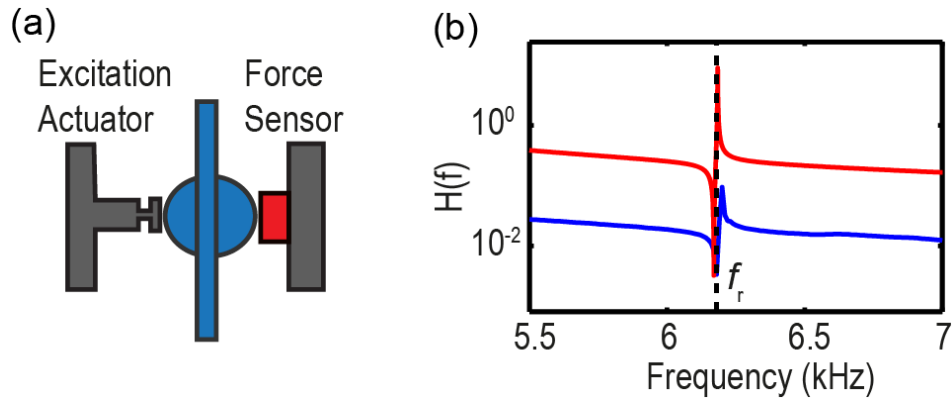


Figure 4.3: Experimental Analysis of the Resonant Defect Particle. (a) The schematic of the experimental characterization system. (b) A comparison between the theoretical and experimental transmission spectra for the system in (a).

4.5.2 Extraordinary stiffness tunability

This modeling is for the experimental setup described in section 3.3.2. The results are shown in chapter 6. We use a discrete particle model to simulate the dynamics. The table below lists the values used in the simulations, which are either measured experimentally or fit for. We fit for two parameters in our model.

The first is the lattice's Hertzian contacts at the ends. We found that the experimental support expands slightly as a result of its finite stiffness. We include this by modifying the contacts at the edges of the chain, A_1 and A_{10} . This does not affect the dynamics at the defect site. Figure 4.4 shows the Hertzian fit used to find the total stiffness of the chain and supporting structure,

$$A_{fit}^{-2/3} = \sum_i A_i^{-2/3}. \quad (4.28)$$

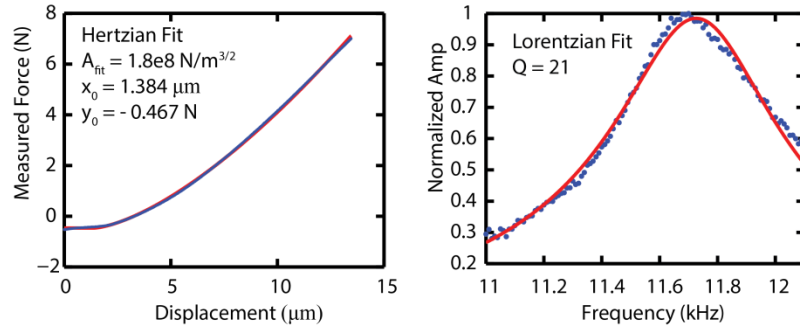


Figure 4.4: Experimental Fits to determine Numerical Parameters. (Left) Fit of the static response of the chain to Hertzian Force Law. (Right) Fit of the linear amplitude response of the defect to a Lorentzian to determine the linear dissipation of the chain.

The second we fit for is the linear dissipation of the particles. To find this we perform a frequency sweep at low amplitude drive excitations in the experiment and fit the measured amplitude response to a Lorentzian. We measure the quality factor of the mode and then choose a dissipation time constant for the numeric that results in the same quality factor for the defect mode.

The contacts at the excitation particle are modified to include the sinusoidal expansion of the chain. Because the stiffness of the piezoelectric disk is much larger than the Hertzian contacts, the piezo expands in proportion to the voltage applied, and the assembled structure can be assumed to move as a single expanding bead.

$A_i = 9.7576 \text{ N/μm}^{3/2}, \quad i \neq 1,5,7,10$	Sphere – sphere contact stiffness
$A_1 = A_{10} = 1.7106 \text{ N/μm}^{3/2},$ $i = 1,10$	Boundaries contacts stiffness
$A_5 = 7.9670 \text{ N/μm}^{3/2}$	Defect sphere contact stiffness
$A_7 = 13.799 \text{ N/μm}^{3/2}$	Excitation particle – sphere contact stiffness
$m_i = 28.4 \text{ g}, \quad i \neq 6,7$	Sphere mass
$m_6 = 3.6 \text{ g}, \quad m_7 = 20.2 \text{ g}$	Defect mass, and excitation particle mass

$\delta_i = \left(\frac{F_0}{C_i}\right)^{2/3}, \quad i \neq 6,7$	Equilibrium spatial overlap
$\delta_i = \left(\frac{F_0}{C_i}\right)^{2/3} + \frac{B}{2} \cos(2\pi f_d t),$ $i = 6,7$	Spatial overlap including the harmonic signal applied to the excitation particle
$\tau = 0.275ms$	Dissipation time constant

Table 4.2: Model Parameters (A_1, A_{10} , masses, τ are experimentally measured).

*Chapter 5*LINEAR DYNAMICS IN NONLINEAR LATTICES: LOCAL TO EXTENDED
TRANSITIONS OF RESONANT DEFECT MODES

We study the localized modes created by introducing a resonant defect in a mechanical lattice. We find that modes introduced by resonant defects have profiles that can be tuned from being extremely localized to totally delocalized by an external force. This is in direct contrast with modes introduced by traditional mass or stiffness defects, in which the modes' profiles stay constant. We present an analytical model for resonant defects in one-dimensional nonlinear lattices, computationally demonstrate the equivalent effect in a two-dimensional lattice, and experimentally observe the mode profiles in a granular crystal. While our study is concerned with nonlinear mechanical lattices, the generality of our model suggests that the same effect should be present in other types of periodic lattices.

5.1 Introduction

The ability to actively control a material's properties through external stimuli is rare and is a goal of materials design^{16,101}. Defects have an enormous effect on material properties: electrical conductivity in semiconductors¹², thermal conductivity¹³, and mechanical strength^{14,15} are just a few examples. This is in part because defects in periodic lattices allow for local modes of vibration that interact with propagating waves and affect material properties⁴⁴⁻⁴⁷.

The periodicity of crystals lattices may result in frequency bands and band gaps¹⁰. Modes that are in the frequency band extend the entire length of the crystal. In contrast, a mode with

frequency in the band gap is not extended but spatially localized. A defect breaks the symmetry of the lattice and can introduce such a localized mode. The mode's spatial extension depends on where its frequency lies in the band gap. As the mode's frequency gets closer to a band, the mode profile becomes more delocalized. In traditional mass or stiffness defects, external effects that shift the band frequencies also introduce a proportional shift in the defect mode frequency, rendering the profile of the defect mode insensitive to external influences. This means that for most defects, the localization is determined by the defect to lattice mass ratio²⁷. We show that for a resonant defect the prescribed relationship between mode frequency and band frequency does not exist, and hence the mode profile can be tuned by an external force. This is due to an additional degree of freedom provided by the displacement of the secondary mass⁴⁸. Control over the localization is interesting to applications of defect modes^{50,102-104}, since many properties, for example the wave speed in coupled resonant optical waveguides^{50,105} and the coupling of phonon-photon interactions¹⁰², depend on the spatial overlap of modes.

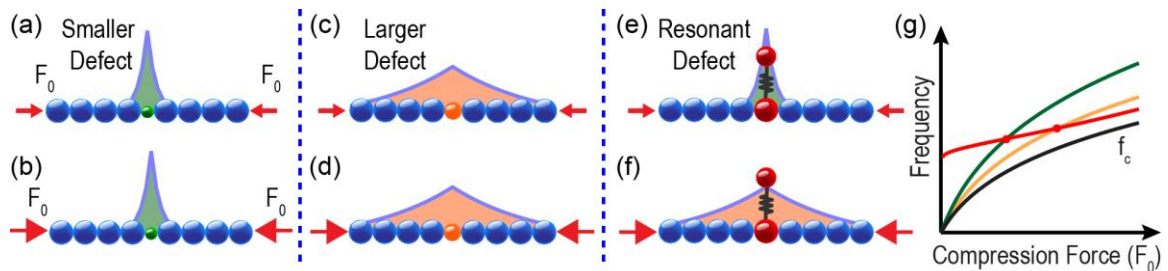


Figure 5.1: A schematic illustrating defect induced local modes and resonant defect tunability. (a),(c), and (e), represent the lattice subject to lower compression, while (b),(d), and (f) represent a higher compression. (a) and (b) show a mode due to a small defect (green) that is highly localized and does not change its profile between low (a) and high compression (b). (c) and (d) show that the mode due to a larger (red) defect is less localized and still does not depend on compression. (e) and (f) show a mode created by a resonant defect (red) in which the localization can be tuned to from highly localized to completely delocalized. (g) illustrates the origin of this tunability. The small (green) and large (orange) defect frequencies maintain a

constant proportion with the band cutoff frequency, resulting in an unchanged localization. In the case of the resonant defect (red) frequency, this constant proportionality is not prescribed. Thus, compression changes the spatial profile of a resonant defect mode.

5.2 Tuning mode profiles

We study the dynamics of a local mode and observe how it transitions from highly localized to completely delocalized as a result of an external compression. Figure 5.2 shows the steady state force measured in the particle next to the resonant defect (Fig. 5.2a) and at the end of the chain (Fig. 5.2b). This dynamic force results from a harmonic excitation at the defect's resonating mass. The measured force is a function of the excitation frequency and static compression. On top of the experimental results, the theoretical expression for the band edge in a granular crystal is plotted as a white dotted line, $f_c = 4.9 \cdot F_0^{1/6}$ [kHz]. Below this line, we see the individual modes of the band rise up in frequency as the compression increases. Since the force sensor in Fig. 5.2a is next to the defect, this measures both local and extended dynamic forces. Figure 5.2a shows the presence of the defect resonance mode (varying slightly around 6.2 kHz) at all compressions. This defect mode frequency increases only a few Hz as a result of increasing compression. This is due to the small mass participation, m_r , of the resonating structure. Figure 5.2b shows the force in the sensor at the end of the chain. This sensor measures only the extended modes, i.e., effects far away from the defect. This sensor does not detect the defect mode until the band edge crosses the mode's frequency at approximately 4 N. Beyond this compression, the defect mode becomes extended and the excitation propagates through the crystal. This shows that a single resonant defect can be tuned to an arbitrary effective size.

More insight on the defect mode's dependence on compression can be seen in Fig. 5.2c, 5.2d, and 5.2e, which show the mode's spatial profile at three increasing compressions, corresponding to the dashed vertical dashed lines in Fig. 5.2a and 5.2b. The left two panels (Fig. 5.2c and 5.2d) are measured at compressions while the mode is still localized, before the dynamics are extended. As the granular crystal is compressed and the acoustic band edge approaches the mode and the mode begins to delocalize, i.e., the exponential attenuation decreases. Above a certain compression the acoustic band rises above the defect mode frequency and the dynamics transition to extended. An analogous tuning and transition has been achieved by geometrically altering defect cavity layers in phononic superlattices¹⁰⁴. The rightmost panel (Fig. 5.2e) shows the extended mode profile at a higher compression. This reveals why there is little force observed in Fig. 5.2b until high compressions.

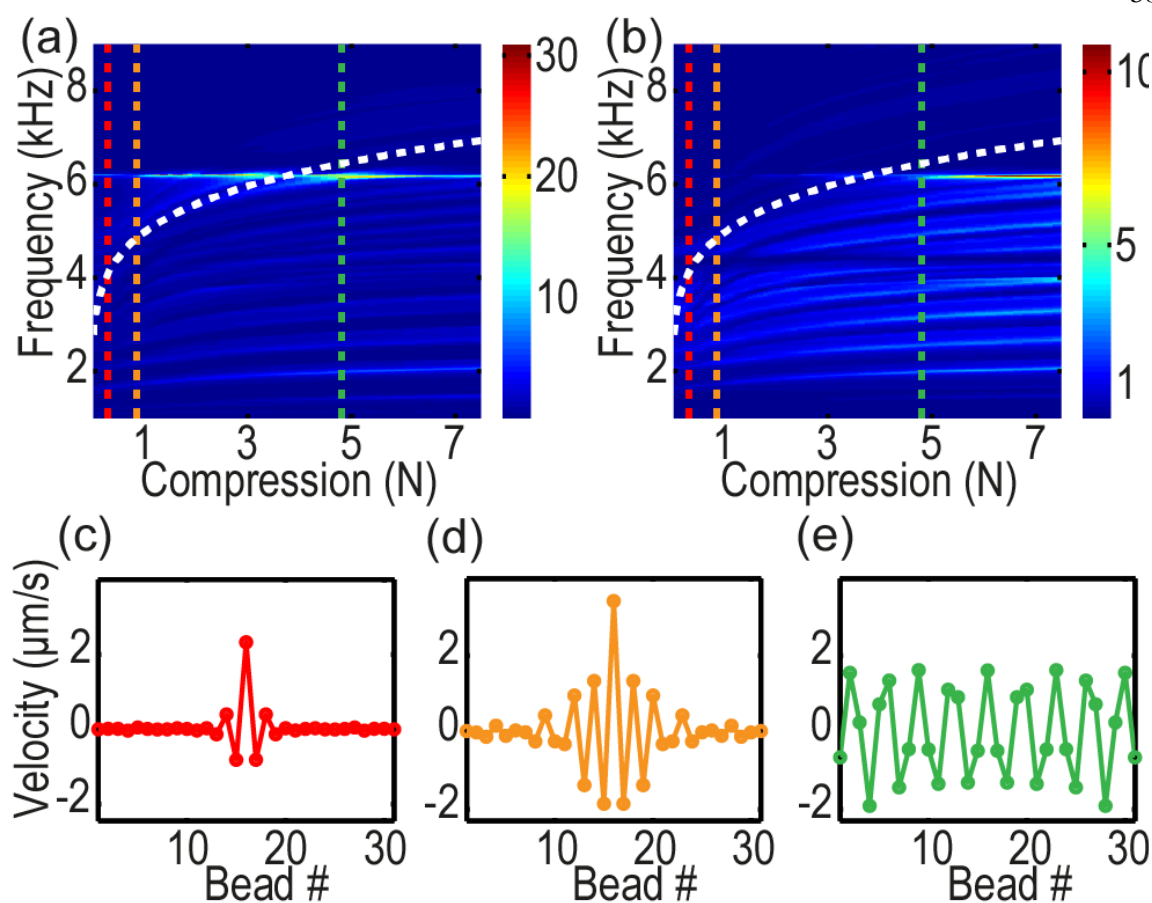


Figure 5.2: The acoustic band and defect mode profile evolution. The color scale shows the steady state amplitude at the embedded force sensors as a function of the frequency and the static compression (a) next to the defect and (b) at the crystal's edge. The defect mode, around 6.2 kHz, appears in the force sensor at the crystal's edge only after the band edge rises above the frequency of the defect mode (at 4 N). The mode's frequency increases very slightly as the lattice is compressed. The dotted curve is the theoretical edge of the acoustic band. (c),(d), and (e) show the local mode profile measured at three different compressions (0.3 N, 0.9 N, and 4.8 N), which are indicated as dotted vertical lines in (a) and (b). At higher compressions, shown in (e), the mode transitions to being completely extended and the dynamics are delocalized. The measurements are performed for half of the chain and we plot their mirrored image of the other half for clarity.

The underlying physics of the problem can be understood through an analytical model for a resonant defect between two semi-infinite generic lattices (see Section 5.4). We quantify the mode's spatial localization using an exponential decay factor, L , defined as the ratio of the

displacement amplitude between neighboring particles. This localization depends explicitly on the ratio, f_c/f_d , of the band edge cutoff to the defect mode's frequencies,

$$L = \frac{2f_d^2}{f_c^2} \left[1 \pm \sqrt{1 - \frac{f_c^2}{f_d^2}} \right] - 1. \quad (5.1)$$

Therefore, a resonant defect mode's localization can be controlled by changing this ratio, which is accomplished through an external compression. However, since the defect mode is actually a mode of the entire lattice, the defect mode frequency also depends on the compression, or equivalently on the band edge, $f_c \propto F_0^{1/6}$. The defect mode frequency can be found solving the implicit equation,

$$\frac{m_r}{m_0} = \left(1 - \frac{f_d^2}{f_r^2} \right) \left[\frac{m_s}{m_0} \left(1 \pm \sqrt{1 - \frac{f_c^2}{f_d^2}} \right) - 1 \right]. \quad (5.2)$$

Together these two equations describe the defect mode localization's dependence on compression, or equivalently on the acoustic band edge.

Figure 5.3a shows a comparison between the analytical solution in an infinite lattice with computational results for solving the eigenvalue problem for a finite chain of 31 particles. We can see that the boundary effects play a negligible role until just before the mode theoretically delocalizes. Figure 5.3a shows three horizontal dashed lines, corresponding to the localization calculated for three different simple mass defect diameters, 11.1 mm, 14.3 mm, and 17.5 mm. The smallest defect results in the greatest localization. This demonstrates that by changing the

external compression, the resonant defect mode localization is similar to that of mass defects of differing sizes.

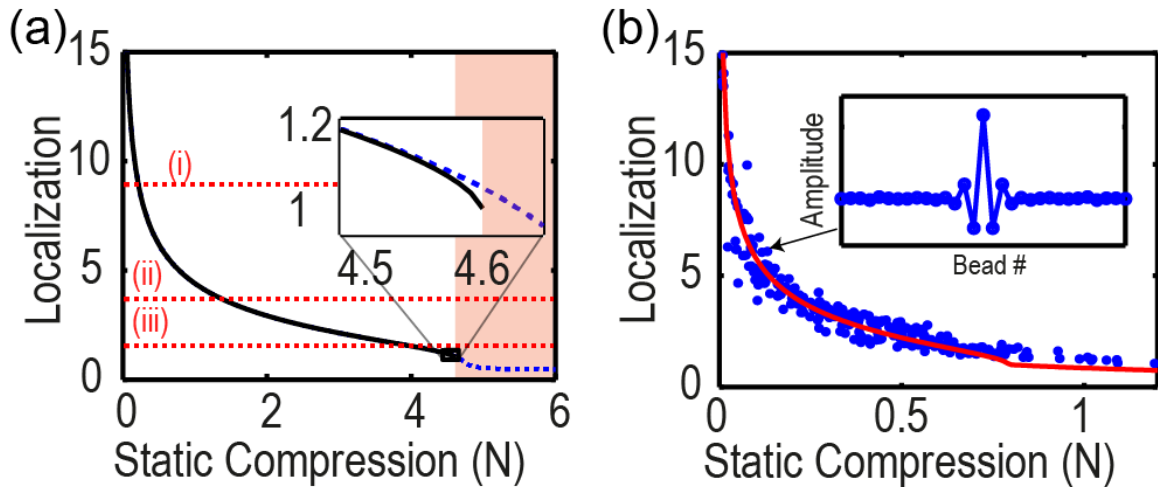


Figure 5.3: Tunable Localization of a resonant defect mode. (a) Localization factor predicted analytically (solid line) for an infinite lattice and calculated computationally for a 31 particle chain (dashed line). Three horizontal dashed lines (i), (ii), and (iii) show localizations for different defect diameters, 11.1 mm, 14.3 mm and 17.5 mm, respectively. In addition, all parameters used in the computation are the derived from the experimental setup. The inset in (a) is an enlarged view, showing the deviation of the computational and analytical results close to the when the defect frequency and band edge meet. (b) The experimentally measured localization and a fit (red line) to the analytical prediction. Each experimental run is shifted along the compression axis to have the same zero point. The inset shows the mode profile used to measure the experimental localization for the run indicated by the arrow.

The experimental measurements of the localization factor as a function of different compressions are shown in Fig. 5.3b, for over 26 independent tests. We fit these experimental results to our analytical model (Eq. 5.2). The analytical model accurately captures the localization's dependence on compression. We attribute the disagreement between the theoretical (Fig. 5.3a) and experimental (Fig. 5.3b) compression scale to friction effects, originating from the large mass of the resonator and significant contact area between the particles and supporting rods.

We computationally study resonant defect modes in a two-dimensional hexagonal lattice with nearest neighbor interactions. Although, the dynamics become more complex due to the presence of both transverse and longitudinal acoustic modes of the crystal, the defect modes' profiles can still be tuned through an external pressure. To understand the dynamics without a defect present, we first found the longitudinal and transverse branches applying periodic Bloch conditions (see section 5.3) and solving the eigenvalue problem. Then we include the defect mode, and confirm that as the defect mode frequency passes below the upper edge of the longitudinal acoustic band, the mode delocalizes, similar to the case of the one-dimensional granular crystal. Figure 5.4 illustrates the mode profile of a resonant defect in a finite lattice at two different isotropic compressions.

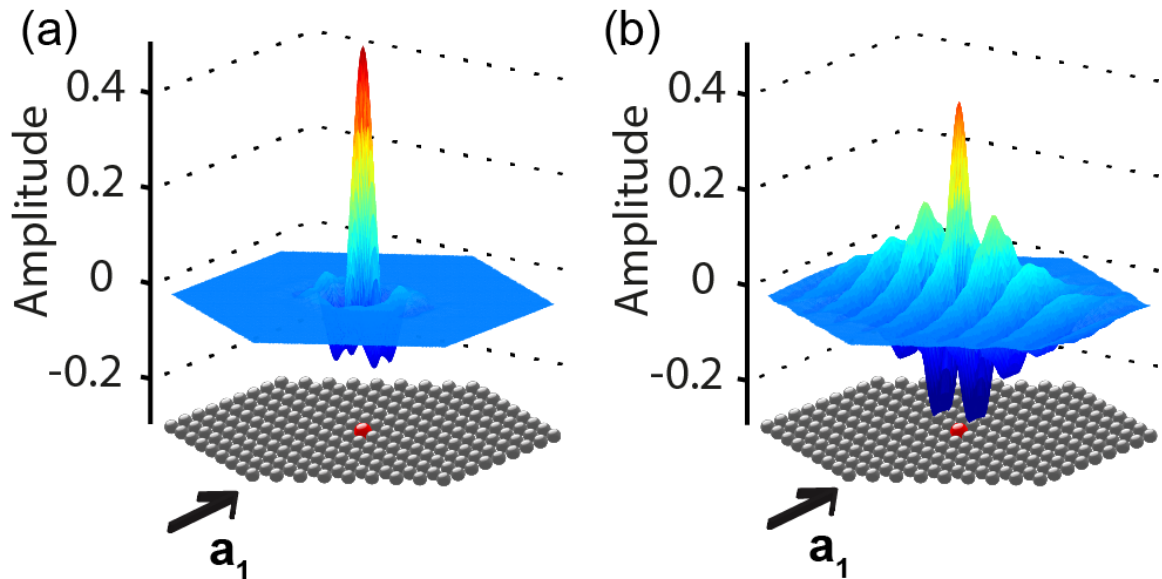


Figure 5.4: Resonant Defects in Hexagonal Lattices. The normalized mode profile due to a resonant defect (red) placed in a two dimensional hexagonal lattice (grey). We plot the amplitude of the particles displacement in the nearest neighbor direction, \mathbf{a}_1 . The mode becomes less localized as it goes from low (a) to high (b) isotropic compression.

5.3 Applications of tuning mode profiles

Ultraslow wave propagation

Coupled resonant optical waveguides use tunneling between strategically placed defects to enable the optical transmission of information. The placement and separation between the defects is used to control the speed of wave propagation[16]. Using this as inspiration, we can flip this idea and control the effective separation by dynamically changing the mode's localization. When a defect mode is highly localized the periodically placed resonant defects are effectively further apart. For weakly localized defect modes, the modes overlap more, and are effectively closer together. Therefore, controlling the localization of the modes also affects their coupling, and the wave speed can be dynamically tuned.

We have demonstrated this concept numerically by solving the system shown in Fig. 5.5a when subjected to periodic Bloch wave conditions. The periodicity of the system leads to a narrow band region in which the wave energy is primarily located in the resonant masses. This bandwidth is an effective measure of the average group velocity for a wave packet located at this frequency and can be tuned to achieve ultraslow acoustic wave propagation in materials. Fig. 5.5b illustrates the extent of the dynamic control and the potential for ultraslow velocity propagation.

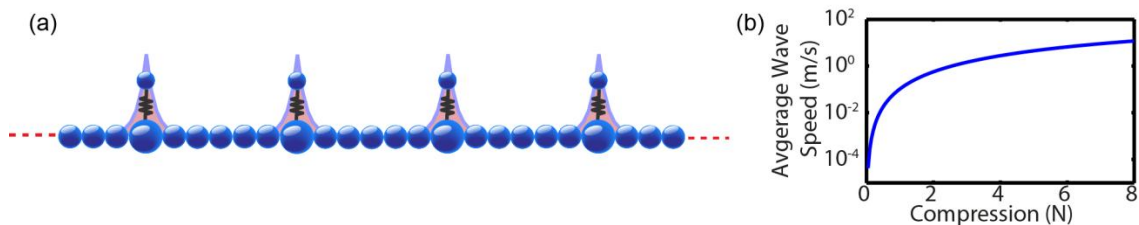


Figure 5.5: Ultraslow velocity wave propagation. (a) A design proposal for achieving tunable ultraslow acoustic or phononic propagation. (b) The wave velocity of the

high frequency narrow band waves in the schematic shown in (a). These results were numerically calculated by applying Bloch conditions to the six particle unit cell.

Tunable scattering relaxation times

Thermal conductivity depends strongly on phonon scattering mechanisms of a crystal. These scattering phenomena can be quantified by the relaxation time constant, τ , which is a result of a variety of effects: Rayleigh scattering from mass or density fluctuations in a crystal, Umklapp scattering between phonons, boundary effects, and resonance scattering from localized modes. The time constants from each effect contribute to the total time constant as a sum of reciprocals,

$$\tau^{-1} = \sum_i \tau_i^{-1}. \quad (5.3)$$

Pohl et al. and Wagner demonstrated that a type of resonance scattering due to localized modes in a crystal makes a significant contribution [7,35]. In the model two phonons collide and are temporarily trapped in an excited state of the localized mode. The scattering relaxation time of this effect is directly dependent on the exponential localization of the mode. We show that this can be localized and controlled through an external stimulus, therefore also giving control over phonon scattering.

2D numerical analysis

We examine the tunability of local defect modes in a hexagonal lattice in two dimensions with nearest neighbor coupling. For a two dimensional system, the coupling stiffness can also be tuned through compression. By applying periodic Bloch conditions, we find the band structure for the monoatomic lattice dynamics (Fig. 5.6). In order to study a tunable defect in this

lattice, we construct a model for an isotropic resonant defect placed at the center of a finite crystal. Since the host lattice has a transverse and longitudinal phonon branch, introducing a defect results in two additional modes, one for each degree of freedom. The two modes delocalize at different compressions.

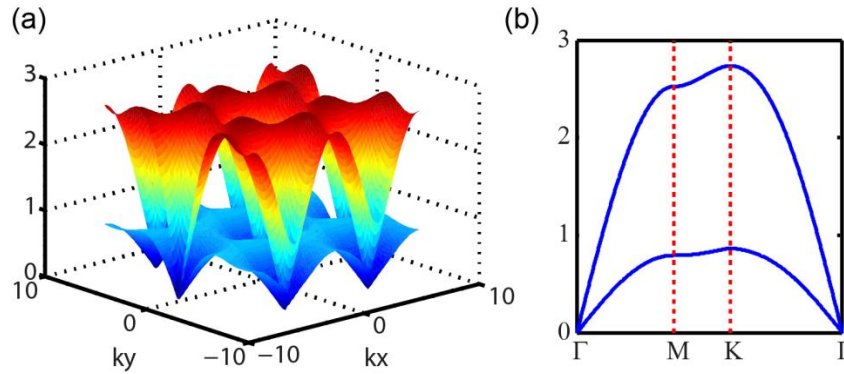


Figure 5.6: Phonon Band Structure for a two dimensional hexagonal lattice . (a) The 2-D band surface with associated cuts (b) along high symmetry directions of a hexagonal lattice. This figure illustrates the acoustic transverse and longitudinal phonon bands.

5.4 Analysis

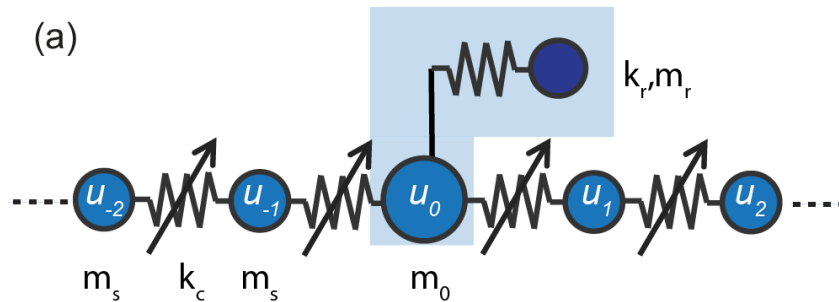


Figure 5.7: Analytical model. (a) A schematic for the analytical model including relevant parameters.

We start by combining the solution for an infinite chain[11] with the frequency dependent effective mass[13] of a resonator particle (Fig. 5.7). If we consider a solution above the

acoustic band of the crystal then the known solution is oscillatory and exponentially localized. This means that the amplitude decays exponentially in both directions by a localization factor L ,

$$u_{-i} = u_{+i} = \frac{u_0}{(-L)^i}. \quad (5.4)$$

In 1-D linear lattices solutions for the j^{th} particle in the equations of motion are described by $u_j = e^{i(kj - \omega t)}$. When the wavenumber is real the solution is extended. However, when the frequency is above the acoustic band edge, the wavenumber has a nonzero imaginary component, and the solution decays. The localization factor that we present is the ratio of amplitudes and is related to the wave number as, $L = -e^{\pm ik}$. When the wavenumber is complex the localization is real.

By considering the solution in one of the semi-infinite lattices, at either side of the defect, $i \neq 0$, we can find how this localization factor depends on frequency. The equation of motion is,

$$-m_s \omega^2 u_i = k_c (u_{i+1} + u_{i-1} - 2u_i). \quad (5.5)$$

By both assuming an oscillatory solution at frequency ω and using the above relation, the equation for particle i 's displacement, u_i , becomes a quadratic equation for L ,

$$L^2 + (2 - 4\omega^2/\omega_c^2)L + 1 = 0, \quad (5.6)$$

where $\omega_c = 2\sqrt{k_c/m_s}$ is the frequency of the acoustic band edge. The solution to (Eq. 5.6) gives the localization factor, L ,

$$L = \frac{2\omega^2}{\omega_c^2} \left[1 \pm \sqrt{1 - \frac{\omega_c^2}{\omega^2}} \right] - 1. \quad (5.7)$$

The equation for L has two solutions where $L_+ = 1/L_-$. This reflects the perspective of the exponential attenuation. In one direction the amplitude is decaying and divided by the factor L , while in the other direction the amplitude is increasing and is multiplied by L . The equation illustrates that the defect mode localization only depends on the ratio of the defect mode frequency to the band edge frequency.

Now we consider an infinite lattice with a single defect at site $i = 0$. The system can be described by the set of equations:

$$-\omega^2 m_i u_i = k_c (u_{i-1} + u_{i+1} - 2u_i), \quad (5.8)$$

where $m_i = m_s$ for all $i \neq 0$. The defect has a frequency dependent effective mass, $m_{eff} = m_0 \left[1 + \frac{m_r}{m_0} \left(1 - \frac{\omega^2}{\omega_r^2} \right)^{-1} \right]$. This replaces the two masses, m_r and m_0 , and spring constant, k_r , describing the defect with $\omega_r = \sqrt{\frac{k_r}{m_r}}$. With a little algebraic manipulation, and again, assuming an oscillatory and exponentially decaying solution supp. (1) , the equation of motion (Eq. 5.8) for the defect particle becomes,

$$m_{eff}\omega^2 = 2k_c \left(\frac{1}{L} + 1 \right). \quad (5.9)$$

Now we can easily plug in for the localization, L , and effective mass, m_{eff} , to arrive at the analytical expression comparing mass ratio and frequencies:

$$\omega^2 m_0 \left(1 + \frac{\frac{m_r}{m_0}}{\left(1 - \frac{\omega^2}{\omega_r^2}\right)} \right) = 2k_c \left(\frac{2\omega^2}{\omega_c^2} \left[1 \pm \sqrt{1 - \frac{\omega_c^2}{\omega^2}} \right] \right). \quad (5.10)$$

By plugging the equation for the direction of L_+ and changing angular frequencies to real frequencies we arrive at the following equation:

$$\frac{m_r}{m_0} = \left(1 - \frac{f_d^2}{f_r^2} \right) \left[\frac{m_s}{m_0} \left(1 \pm \sqrt{1 - \frac{f_c^2}{f_d^2}} \right) - 1 \right]. \quad (5.11)$$

The masses, m_r , m_0 , and characteristic frequency, f_r , of the resonant defect depend on geometry and material, and are therefore a design consideration and do not lead to any dynamics control. In the granular crystal the cutoff frequency depends on static compression

$$f_c = \frac{1}{2\pi} \sqrt{\frac{6}{m_s}} A^{1/3} F_0^{1/6}.$$

Comparison with simple mass defect

Now we can compare this expression with that derived for a mass defect. The equation describing a mass defect can be derived in the same way, except the mass is not an effective mass but instead m_0 .

$$\frac{m_0}{m_s} = \left[1 \pm \sqrt{1 - \frac{\omega_c^2}{\omega^2}} \right]. \quad (5.12)$$

This equation can easily be solved for the frequency of the mode.

$$\frac{\omega^2}{\omega_c^2} = \left[1 - \left(\frac{m_0}{m_s} - 1 \right)^2 \right]^{-1}. \quad (5.13)$$

It is clear from this equation, that the frequency of the mode (and therefore the localization) depends only on the mass ratio.

Limiting case

Now we will consider what happens as the static compression gets large. We start with Eq. 5.11 for comparison. In this case the frequencies of the defect and the band edge both grow, as a result of larger static compressions, but everything else stays constant. In Eq. 5.11, the ratio f_d/f_r grows large and the added 1 in the first factor can be ignored. By rearranging we arrive at,

$$\left(-\frac{f_r^2}{f_d^2} \right) \frac{m_r}{m_0} = \left[\frac{m_s}{m_0} \left(1 \pm \sqrt{1 - \frac{f_c^2}{f_d^2}} \right) - 1 \right]. \quad (5.14)$$

The term on the left approaches zero and we are left with the relation for a simple mass defect.

$$\frac{m_0}{m_s} = \left(1 \pm \sqrt{1 - \frac{\omega_c^2}{\omega^2}} \right) \quad (5.15)$$

Therefore, in the case of extremely large compressions (and when the defect mass is smaller than the masses in the lattice, $m_0 < m_s$), the resonant defect acts as a simple mass defect, m_0 .

Control through design

By designing resonant defects with different geometries, we can tune several properties of the defect mode: the frequency of the defect mode (Fig. 5.8a), the rate at which the mode's profile changes with compression, the compression at which the mode becomes completely delocalized, and the mode's limiting profile at large compression forces (Fig. 5.8b). These properties can be adjusted through design by choosing the total mass, $m_0 + m_r$, resonating mass, m_r , and resonance frequency, f_r . Although somewhat counterintuitive, the frequency of defect modes with a smaller resonating mass are less affected by changes in compression of the lattice, as can be seen in Fig 5.8a. In addition, when the defect mass, m_0 , is less than the rest of the lattice, $m_0 < m_s$, the mode never becomes completely delocalized. Instead, as the compression is increased the mode profile approaches the shape of a simple mass defect mode with mass m_0 . The analytical section below illustrates how this design control manifests itself.

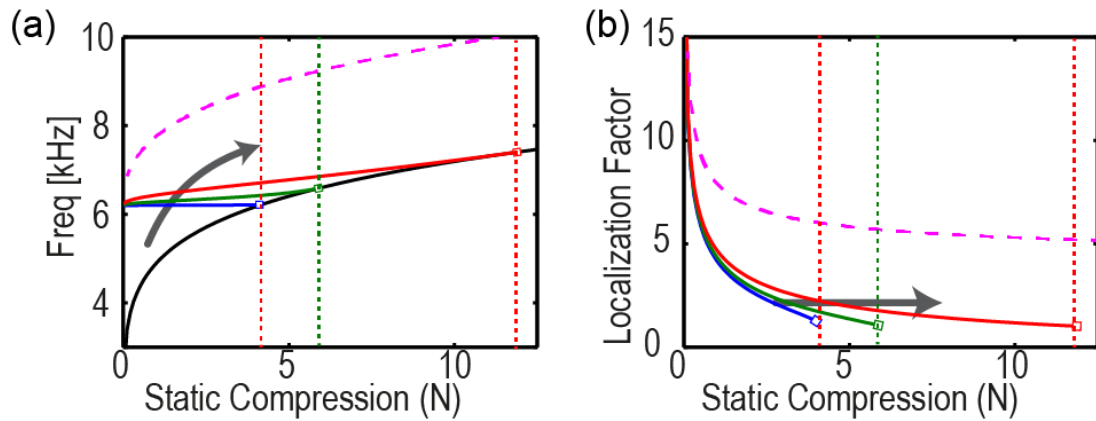


Figure 5.8: Tailoring the Resonator Design. (a) The effect of varying defect parameters on the mode frequency. The results for three resonant masses, m_r (solid lines) and one m_0 (dashed line). The arrow shows increasing m_r . (b) The localization of the defect mode for the same parameters shown in (a). For $m_0 < m_s$ (dashed line) the mode never delocalizes but asymptotically approaches the value of the localization for a mass defect of equivalent size, m_0 . The three vertical dashed lines indicate the compression at which the modes delocalizes when $m_0 < m_s$.

5.5 Conclusion

We have presented a method to actively control the localization of a defect mode in a nonlinear lattice of one and two dimensions. The results are easily extendable to three dimensions. The defect mode that results from a resonant defect has an additional degree of freedom that allows this tunability. This is the first time that a defect mode profile can be actively controlled and tuned without having to change the defect itself. In addition, since the same underlying principles of band tunability apply to a broad range of material systems, we anticipate that these results will impact current device and material applications.

5.6 Author contributions

The results from this chapter are from “Local to Extended Transitions of Resonant Defect modes”³⁷. Joseph Lydon and Marc Serra-Garcia developed the system concept and contributed

equally to the project. Joseph Lydon developed the numerical analysis and Marc Serra-Garcia developed the analytical study. Joseph Lydon and Marc Serra-Garcia performed the experimental work. Chiara Daraio contributed to the analysis. All authors contributed to the writing and editing of the section.

**WEAKLY NONLINEAR DYNAMIC REGIME: EXTRAORDINARY STIFFNESS
TUNABILITY THROUGH THERMAL EXPANSION OF NONLINEAR DEFECT MODES****6.1 Introduction**

Incremental stiffness characterizes the variation of a material's force response to a small deformation change. Typically materials have an incremental stiffness that is fixed and positive, but recent technologies, such as super-lenses¹⁰⁶, low frequency band-gap materials¹⁷ and acoustic cloaks^{107,108}, are based on materials with zero, negative, or extremely high incremental stiffness. So far, demonstrations of this behavior have been limited either to a narrow range of frequencies¹⁷, temperatures¹⁰⁹, stiffness¹¹⁰ or to specific deformations^{21,111}. Here we demonstrate a mechanism to tune the static incremental stiffness that overcomes those limitations. This tunability is achieved by driving a nonlinear defect mode in a lattice. As in thermal expansion, the defect's vibration amplitude affects the force at the boundary, hence the lattice's stiffness. By using the high sensitivities of nonlinear systems near bifurcation points, we tune the magnitude of the incremental stiffness over a wide range: from positive, to zero, to arbitrarily negative values. The particular deformation where the incremental stiffness is modified can be arbitrarily selected, varying the defect's driving frequency. We demonstrate this experimentally in a compressed array of spheres and propose a general theoretical model. This approach opens a new paradigm to the creation of fully programmable materials.

Research on materials with mechanical properties not found in natural systems is a very active field. This research effort has resulted in different solutions: metamaterials¹⁸, materials undergoing phase transitions^{109,112,113} or buckling instabilities²¹, and materials with

electromagnetic coupling between constituents^{110,114}. Metamaterials are periodic systems with local resonances that can present negative or zero effective mass and stiffness^{17-19,48}; however, their practical application is limited to a narrow band around the local resonance frequency¹⁸. Materials that operate around phase transitions^{112,115} or buckling instabilities²¹ can achieve extreme negative values of the incremental stiffness, but their operation is limited to the deformation or temperature where the instability occurs¹⁰⁹. Negative stiffness inclusions in a matrix, used to achieve positive extreme stiffness, suffer from stability problems¹¹⁶. Finally, many of the proposed solutions are limited in the range of attainable stiffness¹¹⁰.

In order to address those limitations, we demonstrate tuning the incremental stiffness of a lattice using a method based on the thermal expansion of defect modes. Thermal expansion is an ubiquitous property of anharmonic lattices⁹⁵, in which the lattice can be made to expand or contract by increasing or decreasing its vibrational energy. In our method, we drive a defect mode in a lattice with a harmonic signal. As a consequence of anharmonicity in the lattice, an external deformation moves the defect mode in and out of resonance, affecting its vibrational amplitude. These changes in vibrational amplitude affect the thermal expansion of the defect, and therefore the force at the boundary. This alters the incremental stiffness of the lattice. We use this concept to achieve negative stiffness (Fig. 6.1a).

6.2 Tuning the incremental stiffness in a granular chain

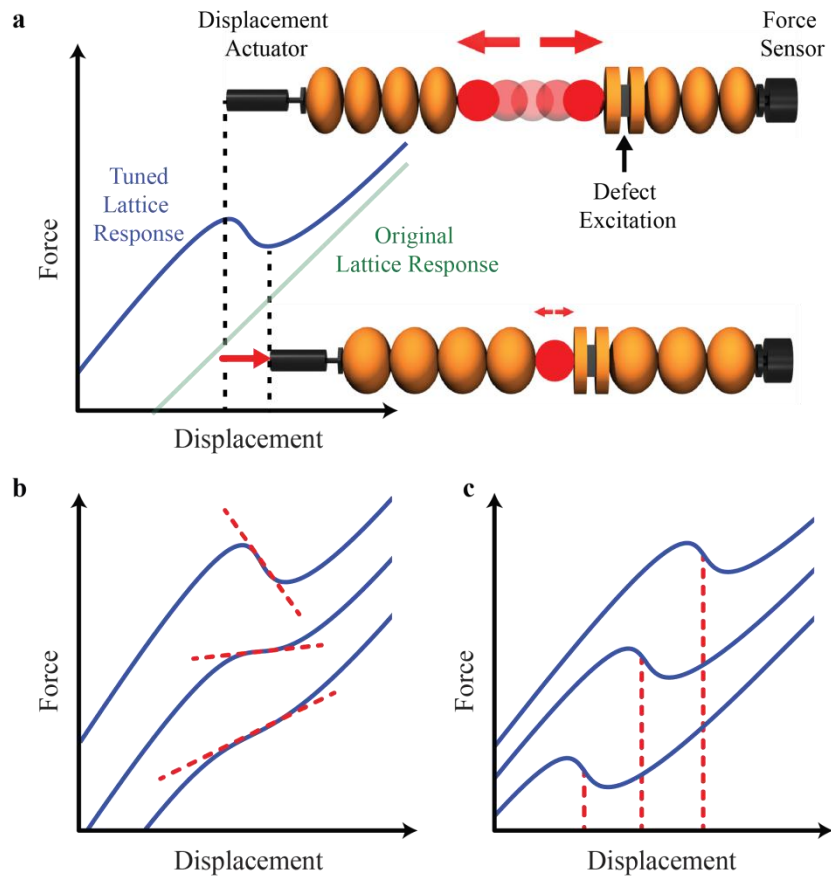


Figure 6.1: Tuning stiffness through thermal expansion. **a.** Schematic diagram of the tunable stiffness mechanism illustrated in a 1-D granular chain. The diagram shows the static force on the lattice due to a prescribed displacement while harmonically driving the defect mode. As the lattice is compressed (blue arrow), the defect vibrational amplitude decreases (red arrows). This results in a negative incremental stiffness due to thermal contraction of the defect mode. **b.** Changes in the driving frequency and amplitude of the excitation control the incremental stiffness, and **c.** the strain point at which the stiffness is being modified. The curves are offset for clarity.

We demonstrate the concept in a one-dimensional lattice of coupled spheres (see Fig. 6.1a). The spheres interact through a nonlinear Hertzian contact²⁷. The central particle is a defect that allows the existence of a localized vibrational mode^{27,117,118}. A piezoelectric actuator is embedded in the vicinity of the defect particle and is used to harmonically excite the defect mode. We monitor the defect mode vibration using a laser vibrometer. We acquire the quasi-

static force-displacement relation of the lattice, by prescribing an external deformation and measuring the force at the opposite boundary. The vibration of the defect mode affects the force-displacement relation. The amplitude and frequency of the defect excitation are the two control variables that determine the mechanical response. Using these variables we can select both the incremental stiffness magnitude (Fig. 6.1b) and the displacement point where the incremental stiffness is being modified (Fig. 6.1c). This allows tuning the force-displacement response of a lattice at a selectable displacement value, a capability that exists so far only in biological organisms¹¹⁹.

In our system the measured force depends on both the applied displacement and on the amplitude of the mode, $F(x, A)$. Therefore, the incremental stiffness, defined as the total derivative of the force with respect to the displacement, is given by the equation:

$$\frac{dF}{dx} = \left(\frac{\partial F}{\partial x}\right)_A + \left(\frac{\partial F}{\partial A}\right)_x \frac{\partial A}{\partial x}. \quad (6.1)$$

The first term on the right side of the equation gives the stiffness of the lattice, neglecting any change in the defect mode's amplitude. The second term describes the effect of the oscillation of the defect mode. The function $(\partial F/\partial A)_x$ is the change in the force due to a change in amplitude of the defect mode and quantifies the intensity of the thermal expansion. From a dynamical point of view, this arises due to an asymmetry of the interaction potential⁹⁵ and in our lattice is always positive (see Appendix, 1.1). Finally, the effect of the strain on the amplitude of the mode is contained in the quantity $\partial A/\partial x$.

The vibration amplitude's dependence on strain is a consequence of the harmonic excitation and of the nonlinearity present in the chain. The harmonic excitation results in a defect mode resonance, which occurs when the defect mode's frequency matches the excitation frequency. The nonlinearity relates the mode's frequency, ω_d , to the lattice strain, δ_0 . In our system the Hertzian contact results in the relationship, $\omega_d \propto \chi_0^{1/4}$. As a result, straining the lattice causes a change in the mode's frequency (Fig. 6.2a). If the mode's frequency approaches the excitation frequency, the mode gets closer to resonance, and therefore the oscillation amplitude increases. Conversely, if the mode frequency moves away from the excitation frequency, the oscillation amplitude decreases (Fig. 6.2b). This strain controlled resonance results in a dependence of amplitude on strain and therefore, in a non-zero $\partial A / \partial \chi$.

Different excitation frequencies cause the resonance to happen at different strain values (Figs 6.2a,b). This is due to aforementioned frequency strain relationship, which associates a particular resonance strain to each excitation frequency. By choosing the excitation frequency we are able to set the displacement region where the system is in resonance and the stiffness is being modified (Fig. 6.2b).

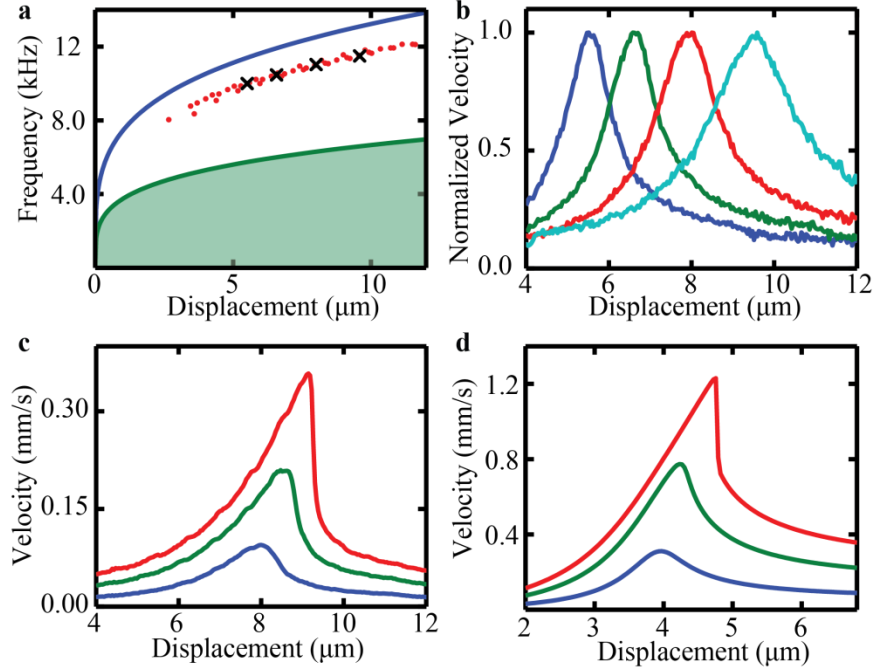


Figure 6.2: Response of the nonlinear defect mode. **a.** Theoretical defect mode (blue) and acoustic band (green) frequencies' dependence on prescribed displacement. Experimental measurements are plotted as red dots with the four curves in panel **b** marked with black crosses. **b.** Normalized experimental velocity of the defect mode as a function of displacement of the lattice. Curves correspond to excitation frequencies of 10(blue), 10.5(green), 11(red), and 11.5 kHz (cyan). **c.** Experimental velocity of the defect mode for drive amplitudes of 4.2 (blue), 9.8 (green), and 15.4 nm (red) all at 10.5 kHz. **d.** Numerical results corresponding to **c**, for defects driven at 20, 50, and 80 nm, respectively. Our simplified model (see Methods) qualitatively reproduces the experimental results, but is unable to make precise quantitative predictions.

The effect of the excitation amplitude on the defect's vibration is shown in Fig. 6.2c,d. As expected, driving the defect with larger harmonic forces results in larger oscillations. Furthermore, as the excitation amplitude gets larger the resonance response becomes increasingly asymmetric. This is a common property of driven nonlinear oscillators close to a bifurcation⁸. As nonlinear system's approach bifurcation points, oscillations become extremely sensitive to the strain¹²⁰; in our system the magnitude of $\partial A/\partial x$ approaches minus infinity. This allows us to achieve arbitrarily large negative values of incremental stiffness.

These extreme negative values have been attained experimentally. The measured force-displacement curves at four different drive amplitudes are shown in Fig. 6.3. The incremental stiffness at our selected strain progressively decreases as the defect excitation is increased (Fig. 6.3a-d). For the largest excitation amplitude, the incremental stiffness reaches negative infinity (Fig. 6.3d). In order to validate that this effect is due to the defect's vibration, we simultaneously measure the defect's mode amplitude, presented below each force-displacement curve in Fig. 6.3a-d. The greatest change in the incremental stiffness happens where the slope, $\partial A/\partial x$, is the most negative. This occurs because larger changes in vibrational amplitude are accompanied by larger changes in thermal expansion. It should be noted that the negative stiffness values are stable because our experiment is done under prescribed displacement boundary conditions.

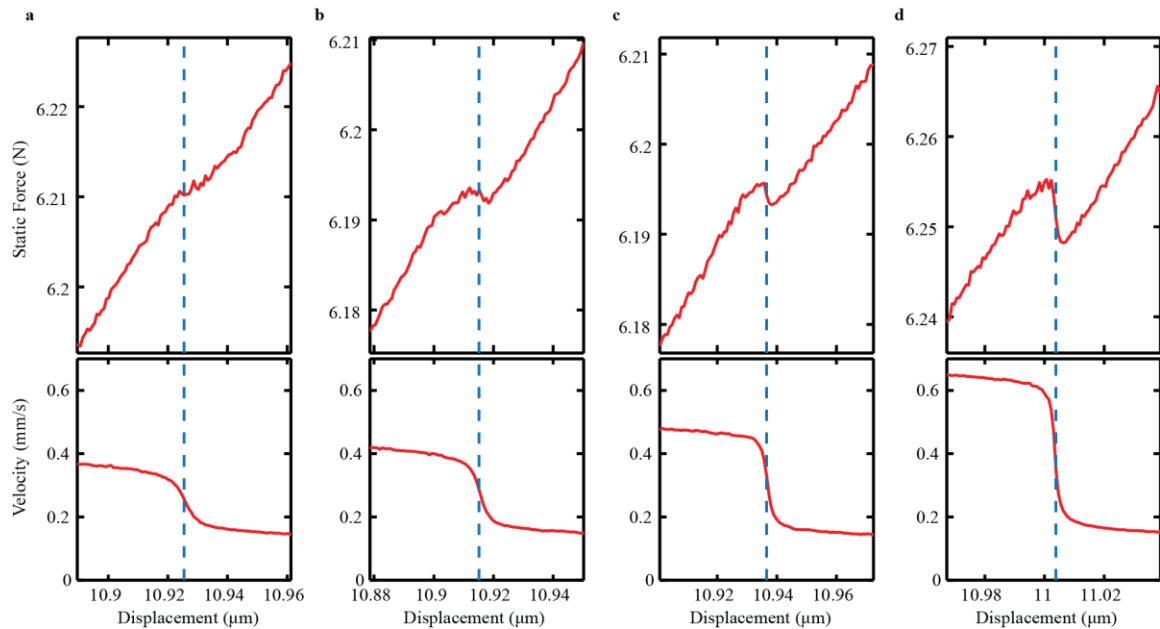


Figure 6.3: Experimental tuning of the incremental stiffness. Force-displacement curves for excitation amplitudes of **a.** 5.9 nm **b.** 6.4 nm **c.** 7.54 nm **d.** 10.9 nm. Shown below are the defect mode velocities (proportional to the mode amplitude, $A(x)$) as a function of the overall displacement, x , of the lattice.

Each pair of drive frequency and amplitude results in a determined incremental stiffness at a particular displacement point. We explore this relationship analytically (see Appendix 1.1) in Fig. 6.4a. The blue lines show contours at the same excitation amplitude and the red lines at the same frequency. To get a particular stiffness at a desired displacement, we select the excitation parameters corresponding to the lines passing through this point. While we only show a finite number of constant lines, all possible values in the shaded region are attainable.

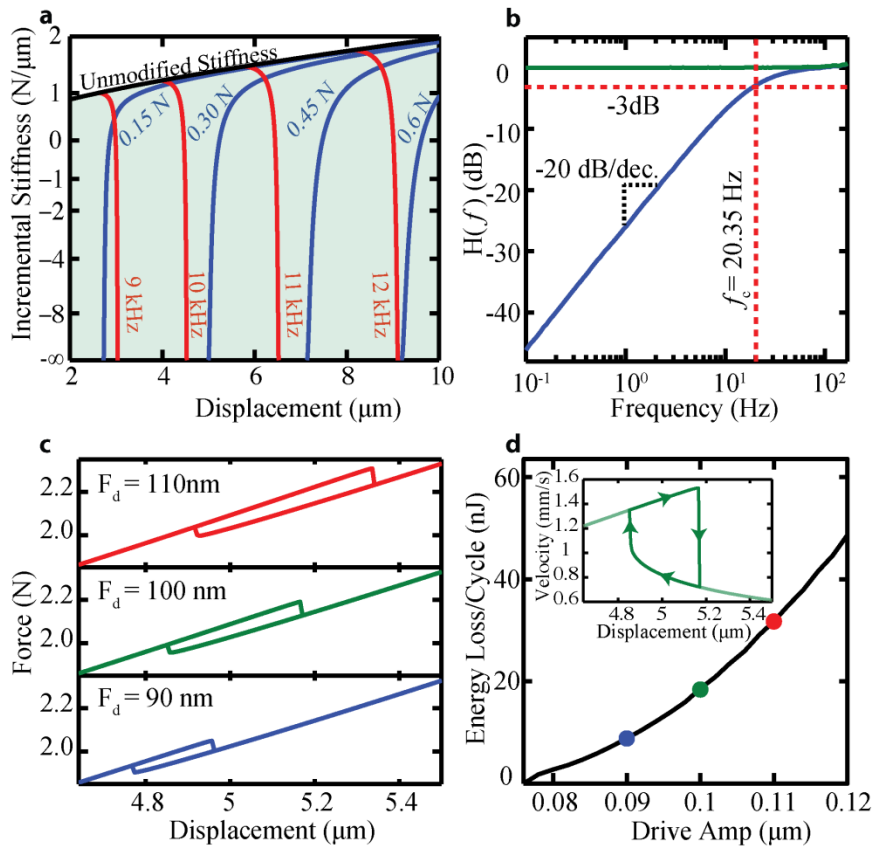


Figure 6.4: Theoretical Investigation. **a.** Map relating the excitation parameters with the modified incremental stiffness and displacement point. **b.** Zero frequency band gap obtained by choosing excitation parameters corresponding to zero stiffness for the lattice. The blue and green line show the force transmitted with the defect drive on and off, respectively. The dotted red line shows the band edge frequency, f_c . When the drive is on, there is a band gap, and when the drive is off the lattice acts as a linear spring. **c.** Force-displacement relationships of the system when it is driven above the bifurcation amplitude. The presence of a tunable hysteresis allows the system to be used as a tunable damper. **d.** As the drive amplitude increases past

the bifurcation, the hysteretic losses per cycle increase. The highlighted points correspond to the results in **c**. The inset in **d** shows the hysteresis in the defect vibration amplitude as the lattice is compressed cyclically.

A remarkable feature of the tuning mechanism presented is that it can achieve zero incremental stiffness. In this region the material will support a load, but it will not transmit any vibration to it, which is of great practical relevance¹²¹. In the zero stiffness region the lattice will have a zero frequency band gap. We simulate this band-gap using our numerical model. In the simulation, we apply a very small amplitude periodic deformation in one end of the chain, and monitor the transmitted force at the other end (Fig 6.4b). We can see that the band gap exists only at low frequencies, and that at high frequency deformations can propagate without attenuation. We quantify the width of the band gap by fitting the transmission to a first order high pass filter, $H(f) = (f/f_c)/\sqrt{1 + (f/f_c)^2}$. This results in a cutoff frequency of $f_c = 20.35 \text{ Hz}$. The upper end of the band-gap is a consequence of the fact that the tuned force versus displacement relationship corresponds to the defect mode oscillating in steady-state. When we change the deformation of the lattice, the steady-state oscillation of the defect is perturbed. The system cannot recover the steady state motion instantaneously. The time it takes for the defect mode to relax back to its steady state limits the upper frequency of the band gap. The speed of the system can be analyzed by using a linear perturbation method (Floquet analysis, see section 6.3).

At the point where the stiffness reaches minus infinity, the dynamics undergoes a bifurcation. At this bifurcation point the system goes from having a single solution to having multiple

stable solutions⁸. This leads to a hysteretic force-displacement response, with the system following different paths when contracting or expanding (Fig. 6.4c). The area of the hysteresis loop corresponds to the loss of energy incurred as the lattice is driven around a compression cycle. This energy is dissipated by the damping acting on the beads and the excitation force at the defect. Since changing the drive amplitude can control the area enclosed in the hysteresis loop, the system can also act as a tunable damper (Fig. 6.4d).

This work allows tuning bulk material properties using the excitation of localized defect modes. We anticipate that these results will extend to a variety of materials containing defects. Several questions remain to be answered. Driving multiple defects at different frequencies presents an opportunity to design materials with an arbitrary stress-strain response. Our analytical model shows that by using different nonlinear couplings it is possible to extend the dynamic range of this technique and achieve positive infinite stiffness (see Appendix 1.1). In two- and three-dimensional materials this mechanism could lead to controllable anisotropy.

6.3 Transient Analysis

In this system we are driving a defect mode and utilizing the changes in the resonance that occurs as we approach the bifurcation. Essential to this phenomenon of tunable stiffness is the assumption that system remains at the steady state response. Each time there is an incremental change in the overall displacement of the lattice, there is also a perturbation to the steady state. This means that changes to the incremental stiffness are limited to lower frequencies. So a natural question that arises is, how slow is slow enough?

In the linear model the time that it takes for a system to relax back to the steady state solution is dictated by the dissipation, i.e., the quality factor of the system. The perturbation that results from compressing the system decays exponentially. The life of the transient is determined by the system dissipation. However, as the nonlinear system approaches the bifurcation, the slope on one side of the resonance becomes steeper. At the bifurcation point the slope is infinite, and there are two solutions. From a stability point of view, at exactly this point the system is on top of a saddle and does not prefer one solution over the other. Therefore a perturbation takes an infinite amount of time to proceed to the next solution. This means that the time it takes perturbations of the system to relax to the steady state is between the linear dissipation time constant and infinity (which occurs only at the bifurcation point).

The incremental stiffness is limited up to a certain cutoff frequency. From the above qualitative argument when the stiffness is only slightly modified (i.e., in a small amplitude case where the linear assumption holds) the system should react at the speed of the dissipation (quickly). However, when the incremental stiffness is being modified more significantly the system is closer to the bifurcation and the perturbations take longer to settle.

Floquet analysis in driven-damped systems is an ideal tool to study the reaction speed of the system. In the context of nonlinear ODE's, Floquet analysis describes a systems relaxation back to a periodic, limit cycle solution. The magnitudes of the Floquet multipliers, λ_i , of a system describe how linear perturbations to a periodic orbit either grow or decay after a single period, T .

$$\mathbf{v}(t + T) = \lambda_i e^{i\phi_i} \mathbf{v}(t). \quad (6.2)$$

This equation relates the solution, \mathbf{v} , of the ODE from one period to the next. The phase, ϕ , indicates a frequency content of the associated multiplier. When there is dissipation the magnitudes of the multipliers are less than one, $\lambda_i < 1$, indicating that the transients decay. This means that a perturbation decays to the time periodic solution with decay factor, λ , each period. We can therefore evaluate an effective time constant that depends on how close the system is to the bifurcation,

$$\tau = \frac{T}{\ln(\lambda_{max})}, \quad (6.3)$$

where T is the period of the driving frequency and λ is the magnitude of the largest Floquet multiplier. It is clear here that as the magnitude of the multiplier approaches one, the denominator goes to zero and the time constant approaches infinity.

As the system approaches the bifurcation (i.e., as the drive amplitude is increased) Floquet multipliers collide along the positive real axis, and one begins to increase in magnitude. The magnitude of the multiplier, or equivalently the time constant, limits the speed at which tuned incremental stiffness can be achieved. As the system reaches the bifurcation, where infinite stiffness occurs, the Floquet multiplier has a magnitude of one and the time constant is undefined.

Figure 6.5 shows the time constants (a), amplitude response (b), and stiffness (c) as the lattice is compressed. The time constant reaches a maximum as the system approaches a bifurcation.

This can be seen in the steepening of the amplitude response. This also corresponds to regions of highly modified incremental stiffness. It is important to emphasize that although we are discussing dynamics from the point of view of being slow enough, the system actually reacts quite fast for many practical applications.

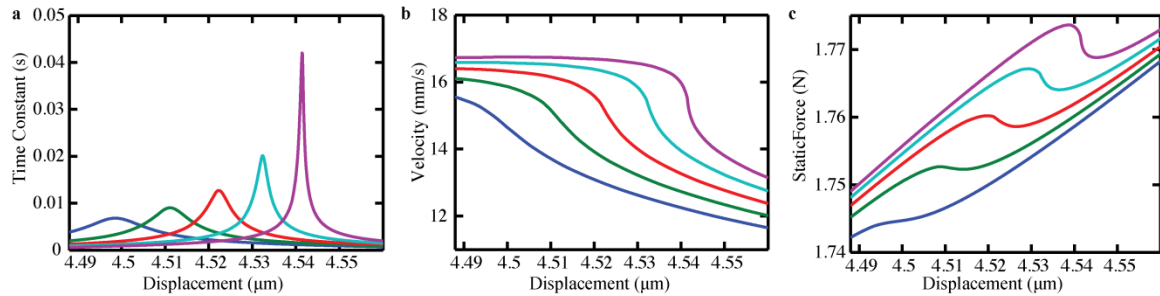


Figure 6.5: Transient Analysis. **a** Time constants that dictate the speed of the relaxation back to steady state. **b** As the system approaches a bifurcation, the amplitude response becomes steeper, and **c** the stiffness is modified more significantly. This is accompanied by longer relaxation time constants, which limits the speed of the system.

In Figure 6.4 we show a band gap at zero frequency. The band gap is not due to a local potential, but instead by tuning the stiffness to zero. This discussion indicates that above a certain frequency the system should not be able to react quickly enough to the perturbations applied by the excitation. We calculate the time constant at the excitation required for the zero frequency band gap, $\tau_0 = 7.807 \text{ ms}$. The time constant that we calculate using Floquet analysis predicts the frequency cutoff remarkably well, $f_\tau = 1/(2\pi\tau) = 20.39$, compared to the frequency cutoff from Figure 6.4, which is calculated from fitting to the first order filter, $f_c = 20.35$. The frequency cutoff here is due to a completely different effect than the linear band gap in a periodic crystal. In a traditional band gap, the wave vector becomes imaginary and is reflected. Here, the stiffness of the system is simply zero.

6.4 Author contribution

The results from this chapter are from “Extraordinary stiffness tunability through thermal expansion of nonlinear defect modes”. Marc Serra-Garcia and Joseph Lydon developed the system concept and contributed equally to the project. Marc Serra-Garcia performed the experimental work and the analytical study. Joseph Lydon developed the numerical analysis. All authors contributed to the analysis of the data and to the writing of the manuscript.

WEAKLY NONLINEAR DYNAMIC REGIME: NONLINEAR RESONANCES AND ENERGY TRANSFER IN FINITE GRANULAR CHAINS

Abstract – In the present work we test experimentally and compute numerically the stability and dynamics of harmonically driven monoatomic granular chains composed of an increasing number of particles N ($N=1-50$). In particular, we investigate the inherent effects of dissipation and finite size on the evolution of bifurcation instabilities in the statically compressed case. The findings of the study suggest that the nonlinear bifurcation phenomena, which arise due to finite size, can be useful for efficient energy transfer away from the drive frequency in transmitted waves.

7.1 Introduction

Acoustic imaging, sensing, energy harvesting, and communication all rely on a firm understanding of the physics of wave propagation and energy transport. To advance these and other applications and to create new materials with enhanced acoustic properties, phononic crystals and acoustic metamaterials have been extensively studied^{122,123}. These are a class of engineered/structured materials that allow control over wave propagation properties by exploiting geometry and periodicity of sub-wavelength structures. One important consequence of periodicity in an infinite material is the presence of frequency band gaps, which results in the complete reflection of excitations with frequencies in the band gap. In reality, all materials are inherently finite, dissipative, and not completely periodic. In systems with finite size, nonlinear instabilities become increasingly more important, even for relatively small dynamic

excitations. In this work, we study the nonlinear dynamic phenomena that result from finite size, while considering dissipation. The presence of these nonlinear effects in a finite system could be very useful in the design of phononic crystals and metamaterials for practical applications.

To further advance the development of acoustic materials, the complex behavior of nonlinear media offers enhanced (i.e., amplitude and frequency dependent) control over the wave propagation. By introducing nonlinear responses in the design of materials, it is possible to control acoustic propagation properties, achieve greater tunability on the acoustic response of given systems, and observe new physical phenomena. For example, nonlinear systems have a distinct advantage over linear systems in their ability to transfer energy between frequencies. Common examples of energy transfer in the frequency domain are subharmonic and superharmonic bifurcations⁵². While these bifurcations can be destructive and are oftentimes avoided (as suggested by von Karman in the design of parts in an airplane¹²⁴), they are also frequently engineered into systems, e.g., sum-frequency and second harmonic generation in nonlinear optics devices¹²⁵. In acoustics, this nonlinear transfer of energy resulted in the development of rectification devices^{32,126} and has been used in non-destructive evaluation and imaging techniques.¹²⁷

In this work, we study the propagation of energy in finite periodic systems that results from similar nonlinear processes, in which energy is exchanged between different frequencies of the system. As mentioned above, in linear periodic materials excitations in the band gap are completely reflected. However, the presence of nonlinearity allows energy to propagate down the chain. This can occur through nonlinear supratransmission in which the energy of a signal

in the frequency band gap is transmitted by means of nonlinear modes^{24,128,129}. This is shown in a series of papers investigating nonlinear supratransmission in sine-Gordon and Klein-Gordon²³, Josephson ladders²⁴, and Fermi-Pasta-Ulam chains¹²⁸. Here, we explore similar nonlinear phenomena in systems of finite size. We accomplish this by studying granular chains of particles as fundamental models for nonlinear periodic structures. We study the bifurcations arising in these systems, and we explore the transition regime bridging the response of finite systems with theoretical predictions based on infinite periodic assumptions.

Granular chains are a class of nonlinear periodic media governed by a highly tunable Hertzian contact interaction between particles¹³⁰: this allows the system to access near-linear, weakly nonlinear, and strongly nonlinear dynamic behavior.³⁵ In weakly nonlinear regime, the granular chains' dynamics are similar to Fermi-Pasta-Ulam systems, and they have demonstrated defect energy localization,⁷⁰ discrete breathers,^{29,68} higher order harmonic wave generation,¹³¹ as well as chaotic dynamics.⁶⁹ In the highly nonlinear regime, coherent travelling waves were predicted to exist such as highly localized solitary waves³⁵ and periodic traveling waves.¹³² Granular chains have been suggested for application in tunable mechanical filtering³⁰ and acoustic rectification.³² In the field of dense granular materials, frequency-mixing processes have been reported for elastic waves¹³³. Their experimental tractability makes granular chains excellent platforms for studying lattice dynamics with highly dependent amplitude and frequency behavior. In addition, the granular chain is an ideal model to study phenomena that occur across different dynamical regimes. When the dynamics are weakly nonlinear and smooth the granular interaction potential can be approximated by a polynomial expansion. This extends the applicability of the results in this regime to similar lattice systems with weak nonlinearities.

We demonstrate that the bifurcations presented occur both in the smooth weakly nonlinear regime and also the strongly nonlinear regime, in which gaps open between beads.

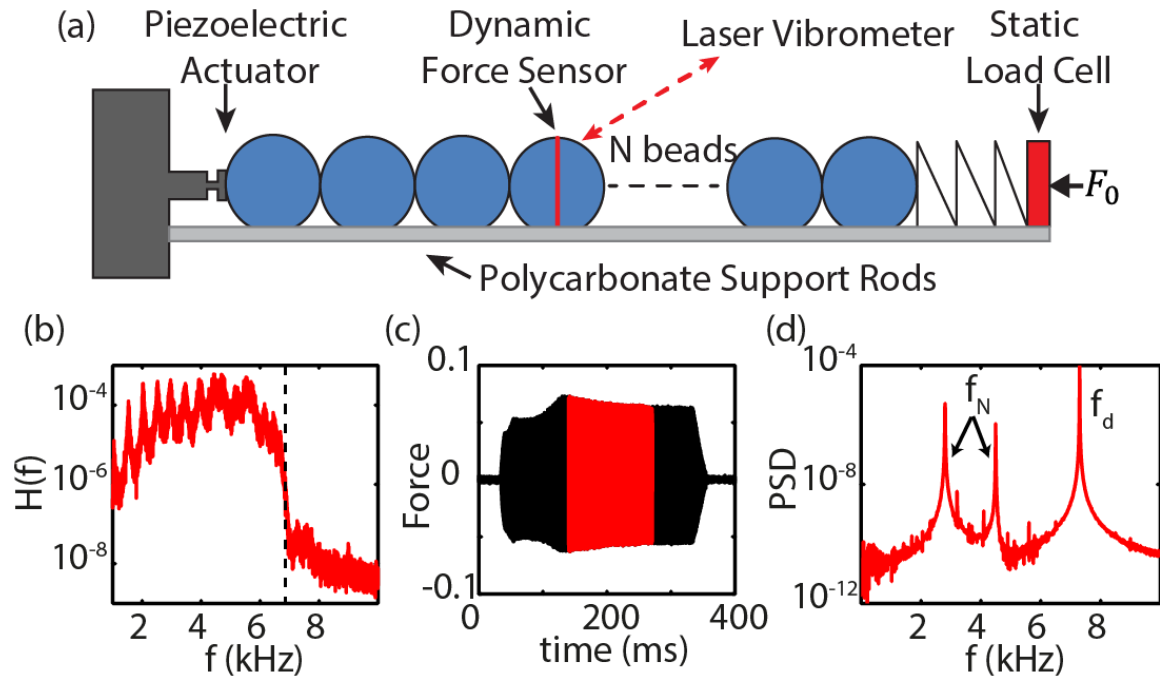


Figure 7.1: (a) Schematic of the experimental setup where the chain's length is varied between 1 and 50 beads. For 1 and 2 bead systems there was no embedded sensor. (b-d) The experimental bifurcation dynamics in a 15 bead chain statically compressed at 8 N and driven at 7.3 kHz. (b) The linear transfer function measured using a white noise excitation. The dotted line at 6.8 kHz indicates the band cutoff frequency measured at the half power point of the last peak. The drive frequency (7.3 kHz) for the force time series in (c) is therefore in the band gap. (c) The force time series measured at the end of the chain shows how the bifurcation results in the amplitude growth and stabilization. (d) The power spectral density (PSD) of the red portion of the force signal in (c) shows that energy is transferred from the drive frequency, $f_d = 7.3$ kHz, to two new frequencies, f_N . We study how this bifurcation results from the finite size of a 1-d system.

In this paper, we explore the nonlinear bifurcations that result from a system's finite size. We motivate the research by showing a typical bifurcation in a chain of 15 beads in Fig. 7.1(b-d). Figure 7.1b shows the linear transmission band and the frequency band cutoff as a dotted line at 6.8 kHz. When driving the system at 7.3 kHz above a threshold amplitude, the oscillations

grow and energy is transferred from the drive frequency to new frequencies. A stable quasiperiodic state is reached. The new frequencies and amplitudes depend sensitively on the drive frequency. Even though the system is driven in the stop band, energy can still propagate through the lower frequency modes. Because the dynamics for systems with many degrees of freedom are quite complex, we observe a slightly different result (i.e., the stable amplitudes and frequencies) for each experimental run. This means that the amplitude of the bifurcation and the newly generated frequencies depend sensitively on the initial compression. To understand the bifurcation structure governing this energy transfer, we start by studying smaller systems, i.e., a single bead oscillator and a two-bead system, and then proceed to larger chains. The goal of this study is to understand the energy transfer of signals above the band gap to lower frequency modes that result from bifurcations. The systems of one and two beads illustrate the fundamental physics of the bifurcations and explain the dynamics present in larger systems. Therefore we build up from these two specific systems.

7.2 Results and discussion

At small drive amplitudes, $B/\delta_{act} \ll 1$, the system's nonlinearity can be ignored and the response is nearly harmonic. However, as the drive amplitude increases, the system becomes nonlinear. The nonlinearity of a system can be described as either softening or stiffening depending on whether the maximum frequency response moves down or up as the drive amplitude is increased. Figure 7.2a shows the experimental nonlinear softening of the mode of a single bead. As the amplitude of the drive is increased the response becomes asymmetric, bending to lower frequencies (i.e., a softening nonlinear potential), deviating from the classic linear Lorentzian response. The amplitude dependent mode profile that we observe here is a

property of nonlinear oscillators commonly studied in the driven damped Duffing oscillator⁵². Figure 7.2b shows experimental data demonstrating a similar nonlinear softening response for each of the modes of a two-bead system. This mode softening is important to the dynamics at higher amplitudes after the bifurcation occurs. It illustrates the nonlinear behavior of the system and explains asymmetry seen later in Fig. 7.5. The numerical counterparts to Fig. 7.2a and 7.2b are shown in Fig. 7.2c and 7.2d. The nonlinear softening of the system is qualitatively similar in these plots. We notice a significant difference in the quantitative amplitudes observed for the nonlinear softening. We believe the quantitative difference in the measured and computed values could be due to one or a combination of many effects. Some of these could include the variation of the surface roughness of the sphere, frictional nonlinearities that become important at low amplitudes, or inaccuracy in measurement and excitation techniques at these extremely low amplitudes. A further investigation of this deviation from the Hertzian contact law at low drive amplitudes would be an interesting future study. However, the key result for our study is the observation that the dynamics are nonlinear, and that there is a softening of the resonance, i.e., the maximum of the frequency moves to lower values as the drive amplitude is increased. We discuss later how this softening could account for the asymmetry bifurcations in frequency.

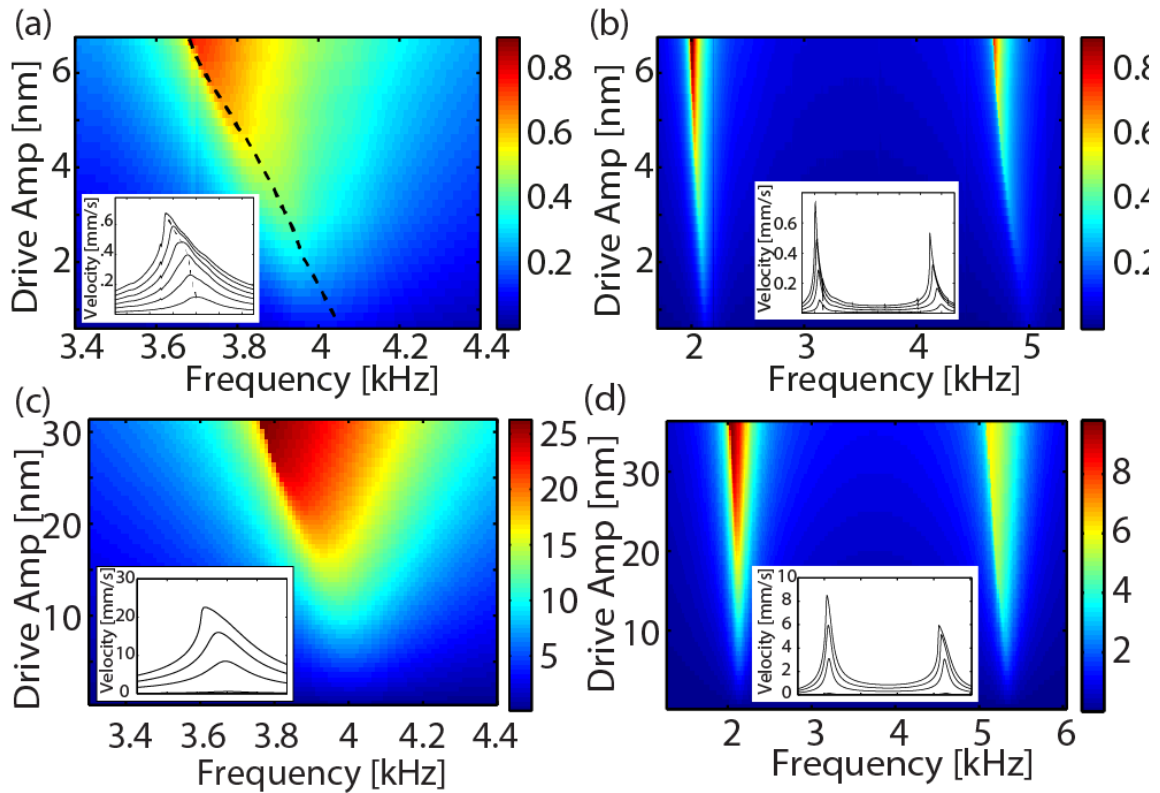


Figure 7.2: Color maps of the experimentally measured RMS velocity [mm/s] of single bead (a) and two bead (b) systems as a function of the drive amplitude and frequency. The velocity is measured in the second bead for the two bead system. The dotted line in (a) indicates the maximum at each drive amplitude. This clearly displays the mode softening to lower frequencies as the amplitude of the excitation increases. The insets show cross sections at increasing drive amplitudes. The asymmetry and the mode softening is a result of the nonlinear Hertzian contact interaction. The measurements are taking using a lock in amplifier to reduce noise. In addition, the low amplitude response is used to estimate the dissipation coefficients used in the one and two bead computational results. Panels (c) and (d) are the computational counterparts to (a) and (b). The system depends sensitively on the initial compression, F_0 , and the diagrams are fit to have the same linear (low amplitude) frequency as the experimental plots. This corresponds to a 8.67 N static compression for the single bead and 4.36N for two beads.

We are interested in changes of the wave dynamics before and after the bifurcation. Figure 7.3 shows an experimentally measured bifurcation in a single bead system when the particle is driven at approximately twice the natural frequency. Initially, a stable harmonic solution develops (Fig. 7.3a), but as the drive amplitude is increased, the velocity sharply increases and

the dynamic response changes (Fig. 7.3b). The data in Fig. 7.3c shows a sudden jump in the dynamic response at a critical drive amplitude, $B_{crit} = 0.07 \mu m$. The power spectral density (PSD) (see Fig. 7.3d and 7.3f) shows that this solution went from being composed of the single drive frequency to being dominated by a subharmonic, $f_d/2$. Figure 7.3e shows the Poincaré section change from a single grouping of points to two distinct groups, indicative of a subharmonic bifurcation⁵⁵. After the bifurcation, approximately 20 times more energy is transferred to the bead, indicating much more efficient coupling between the particle chain and the actuator. In addition, the increase in the oscillation amplitude of the bead, as a result of the bifurcation, depends on the drive frequency. Figure 7.3g shows the computationally calculated hysteresis diagram that corresponds to the experiment. The disagreement observed in the predicted and measured velocity amplitudes can be explained by uncertainty in measurements of the static compression applied to the chain, even though all qualitative features of the bifurcation are maintained.

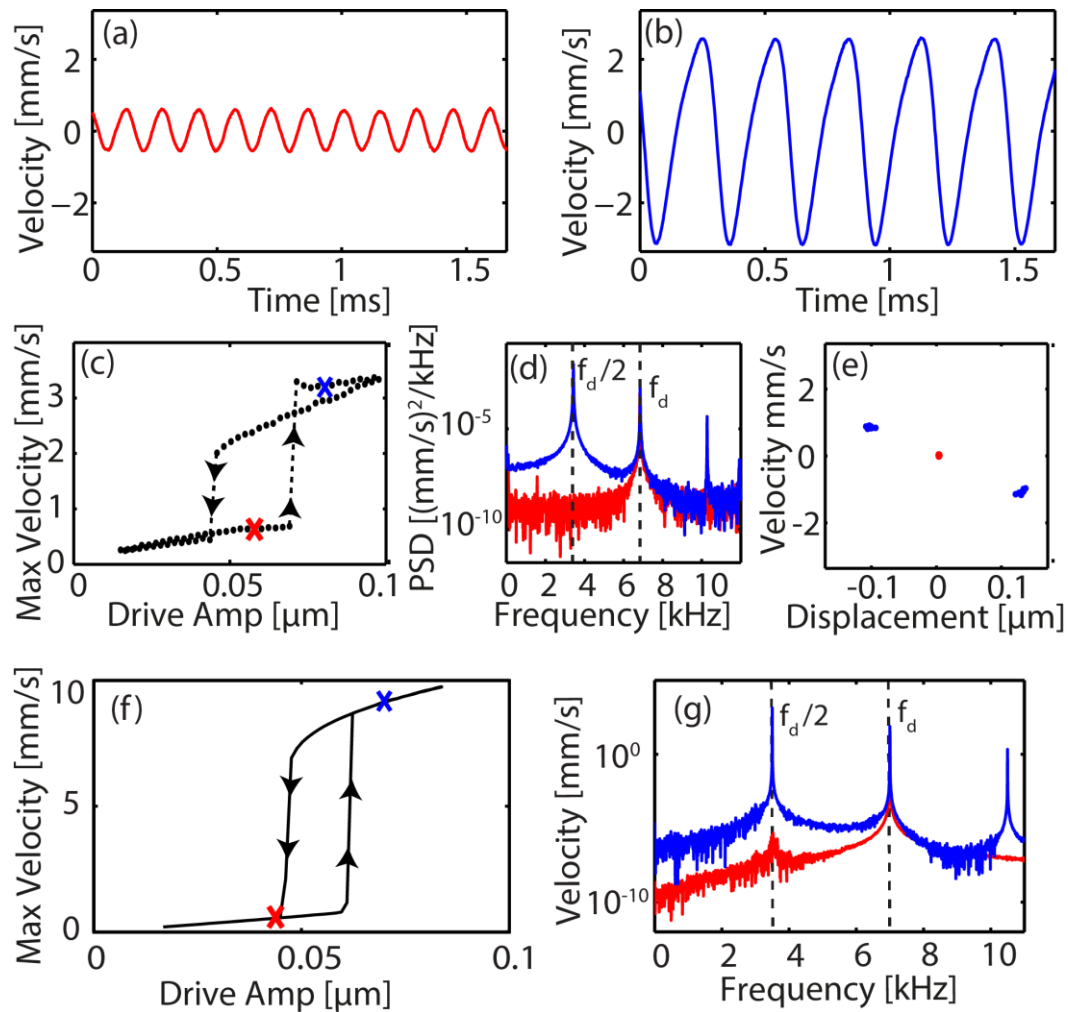


Figure 7.3: The experimental nonlinear resonance and bifurcation behavior of a single bead driven at 6.85kHz. (a,b) The velocity of the bead (a) before and (b) after the bifurcation. (c) The maximum velocity measured at each drive amplitude. (d) The corresponding PSD of two time series, showing the dominant subharmonic frequency at $f_d/2$. (e) the Poincaré section of the dynamics of the bead before (red, central points) and after (blue, side points) the bifurcation. The splitting of the section from one point to two points is characteristic of a period doubling subharmonic bifurcation. Panels (f) and (g) are the computational plots that correspond to the experimental panels (c) and (d). (g) The PSD clearly shows that a sub-harmonic bifurcation occurs after the critical amplitude is crossed.

In longer chains, there is more than one natural frequency, and therefore the system can undergo bifurcations resulting in both subharmonic or quasiperiodic dynamics. When the drive frequency is a multiple of a linear mode's frequency, a subharmonic bifurcation emerges,

and the dynamics are qualitatively similar to the results shown for a single bead. However, when the drive frequency is near the sum of the system's two natural frequencies, quasiperiodic dynamics may arise. Fig. 7.4 shows the response of a two-bead system that goes from a sinusoidal response (Fig. 7.4a) to a solution that is quasi-periodic (Fig 7.4b). Quasiperiodic dynamics occur because the ratios between the drive frequency f_d and new frequencies f_{N1} and f_{N2} are not necessarily rational. Figure 7.4c shows the PSDs of the signals, and illustrates the transfer of energy to the two lower modes. Figure 7.4d shows the Poincaré section of the second bead. It contains points forming a closed curve coming from the intersection of the torus flow in phase space (characteristic of quasiperiodic dynamics) with a plane. In summary, the system goes through a bifurcation in which the dynamics drastically change. There is an order of magnitude change in the amplitude, the total energy transferred to the system, and fraction of energy localized around the drive frequency. To confirm the quasiperiodic behavior, we also performed a computational integration using the same parameters as in the experiment. Figure 7.4e shows the power spectral density before and after the critical amplitude of the bifurcation. The values are shown in the hysteresis plot of Fig. 7.4f. The dynamics agree quite well, and the qualitative disagreements can be attributed to uncertainty in the static compression and reconfigurations of the system coming from misalignment of the spheres during each experimental run.

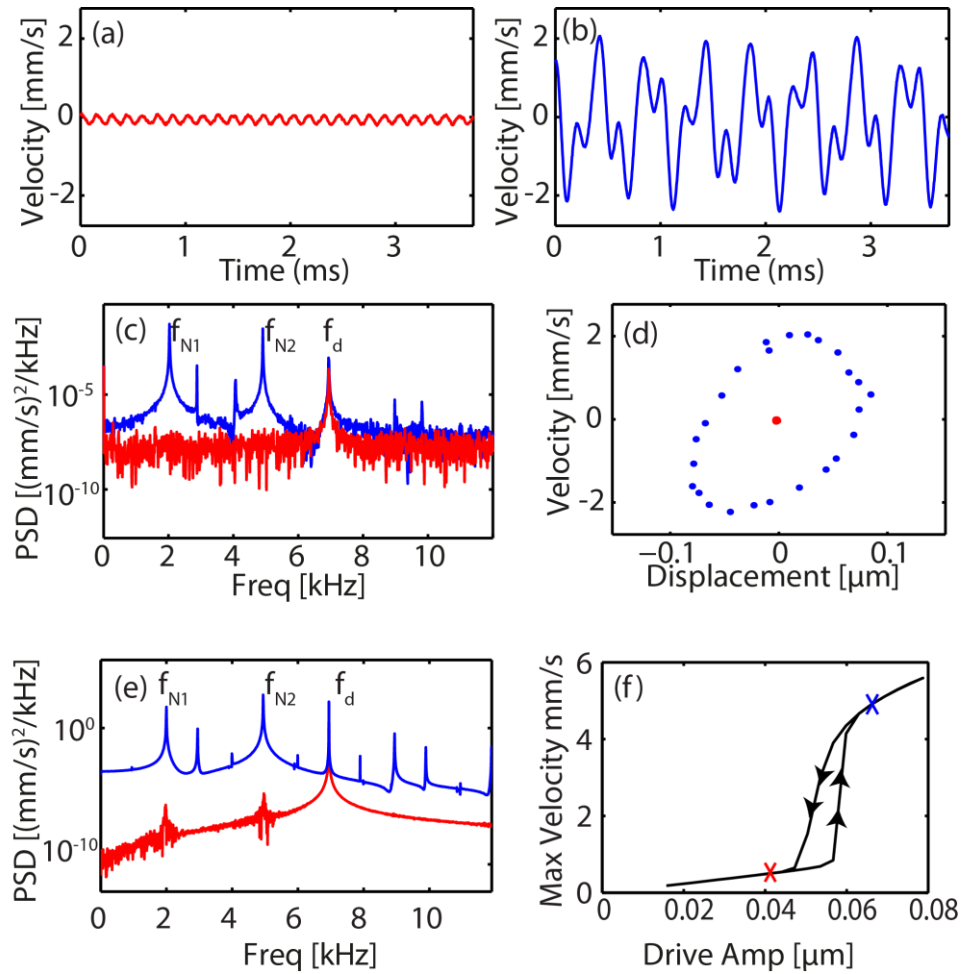


Figure 7.4: Experimental nonlinear resonance and quasiperiodic bifurcation behavior in a system of 2 beads driven at 6.94kHz. (a,b) The velocity of the second bead (a) before and (b) after the bifurcation. (c) The corresponding PSD of two time series, showing the new frequencies f_{N1} and f_{N2} supported by the nonlinearity of the system, where $f_{N1} + f_{N2} = f_d$. The PSD of the time series clearly show that energy is transferred from the drive frequency, f_d , to the two new frequencies. (d) Poincaré sections of the dynamics of the second bead before (red, central point) and after (blue, surrounding points) the bifurcation. This Poincaré shows the classic intersection of a torus and a plane for quasiperiodic dynamics. The finite number of points is due to the finite length of the signal. (e) The PSD of the computational time series taken at the drive amplitudes indicated in (f) and using the same parameters as measured during the experimental runs.

The analysis for one and two bead systems illustrates the two fundamental types of bifurcations that occur in granular chains. Figure 7.5 shows how the bifurcations depend on the different parameters of the system, i.e., drive amplitude and drive frequency. We observed

that these bifurcations occur in certain areas of the parameter space and call these regions tongues, due to their similarity with parametric tongues. This region indicates that, where a sharp transition in the dynamics occurs, the stable solution goes from sinusoidal to either subharmonic or quasiperiodic. The tongues are centered around the multiples and sums of the linear mode frequencies in each system. Numerically we can determine where to sweep these frequencies by solving the eigenvalue problem associated with the equations of motion (1), and experimentally we measure the linear mode frequencies using a broad range frequency sweep. We start by showing the experimental and computational bifurcation tongues of a one and two bead system and then proceed to larger systems. The edge of the tongue shows the edge of a stable harmonic solution. Above the critical drive amplitude the system exhibits either subharmonic or quasiperiodic dynamics.

Figure 7.5a shows the experimentally observed nonlinear tongue for a single bead oscillator. Here, the entire tongue is characterized as subharmonic. The minimum of this region corresponds to twice the frequency of the linear mode. The disagreement between the minimum of the tongue in Fig. 7.5a (7.4 kHz) and twice the linear frequency, 4.0 kHz shown in Fig. 7.2a, is due to different static compressions between runs. The linear frequency measurements were taken at approximately 8 N compression, while the bifurcation is measured at approximately 4 N. On top of the experimental results, we also plot the computationally computed tongue edge, as a black dotted line. The tongue is asymmetric due to the modes softening to lower frequencies (Fig 7.2). As amplitudes of the oscillations increase, the natural frequencies decrease. This causes the tongue in Fig. 7.5a to bend towards lower frequencies. In addition, the color scale shows that the bifurcation becomes more drastic

as the mode bends further from its linear natural frequency. Figure 7.5c shows the computationally calculated bifurcation tongue for a single bead (with the experimentally investigated region indicated with the dashed blue rectangle). The quantity, f_0 , used to non-dimensionalize the frequency is the linear mode frequency. Here it is clear that the minimum is at 2, or twice this frequency. This is because the drive frequency determines how far apart the nonlinear modes must move in frequency. If the minimum is chosen the drive frequency is already a multiple of the linear mode frequency. In the context of the Floquet multipliers, the multipliers start on top of each other. If a frequency slightly lower or above the minimum is chosen, the nonlinear modes decrease or increase in frequency to be a multiple of the drive frequency. The Floquet multipliers must first move before colliding. Therefore the bifurcation occurs most easily at a multiple of the linear mode frequency, leading to a minimum at this point. The solid points in Fig. 7.5(a-d) are computed using a parameter continuation, and they correspond to the pairs of the driving frequency and amplitude at which FMs leave the unit circle, an indicator of the existence of bifurcations. In these plots, the asymmetry becomes clear. Points in red indicate that gaps are opening, which explains why the shape of the tongue changes; the dynamics at this point goes from weakly to strongly nonlinear. The units are shown in nondimensional units to stress that the onset of this nonlinear bifurcation may occur at seemingly small drive amplitudes, at a fraction of the static overlap of the chain.

For two beads (Fig. 7.5 b and d) we see two tongues: one at the sum of the two mode frequencies, 7kHz, and one at twice the higher mode's frequency, 9.8kHz. The tongue associated with the sum is characterized by quasiperiodic bifurcation dynamics, whereas the tongue at twice the modes frequency is subharmonic. A single slice from the quasiperiodic

tongue was previously shown in Fig. 7.4, where the frequency is fixed and the drive amplitude is quasistatically increased. In addition, it is important to note that our computations predict high amplitude subharmonic and quasiperiodic stable solutions exist despite gaps opening, i.e., gaps openings do not directly lead to chaotic dynamics. In this case, the dynamics are non-smooth yet still periodic. While this is somewhat surprising, the possibility of such dynamics is supported by the non-smooth periodic solutions that have previously been observed in granular chains at the uncompressed limit^{26,132}. Figures 7.5(e-g) show a representative of the FMs calculated for each tongue. If the FMs leave the unit circle on the negative real axis, it indicates a subharmonic bifurcation, and otherwise quasi-periodic dynamics. These simulations confirms the subharmonic and quasiperiodic dynamics observed experimentally for each tongue in Figures 7.3 and 7.4, in which we increase the amplitude entering the nonlinear tongue region. The critical driving amplitude for bifurcation shows a good agreement in the experimental and computational results for one and two beads.

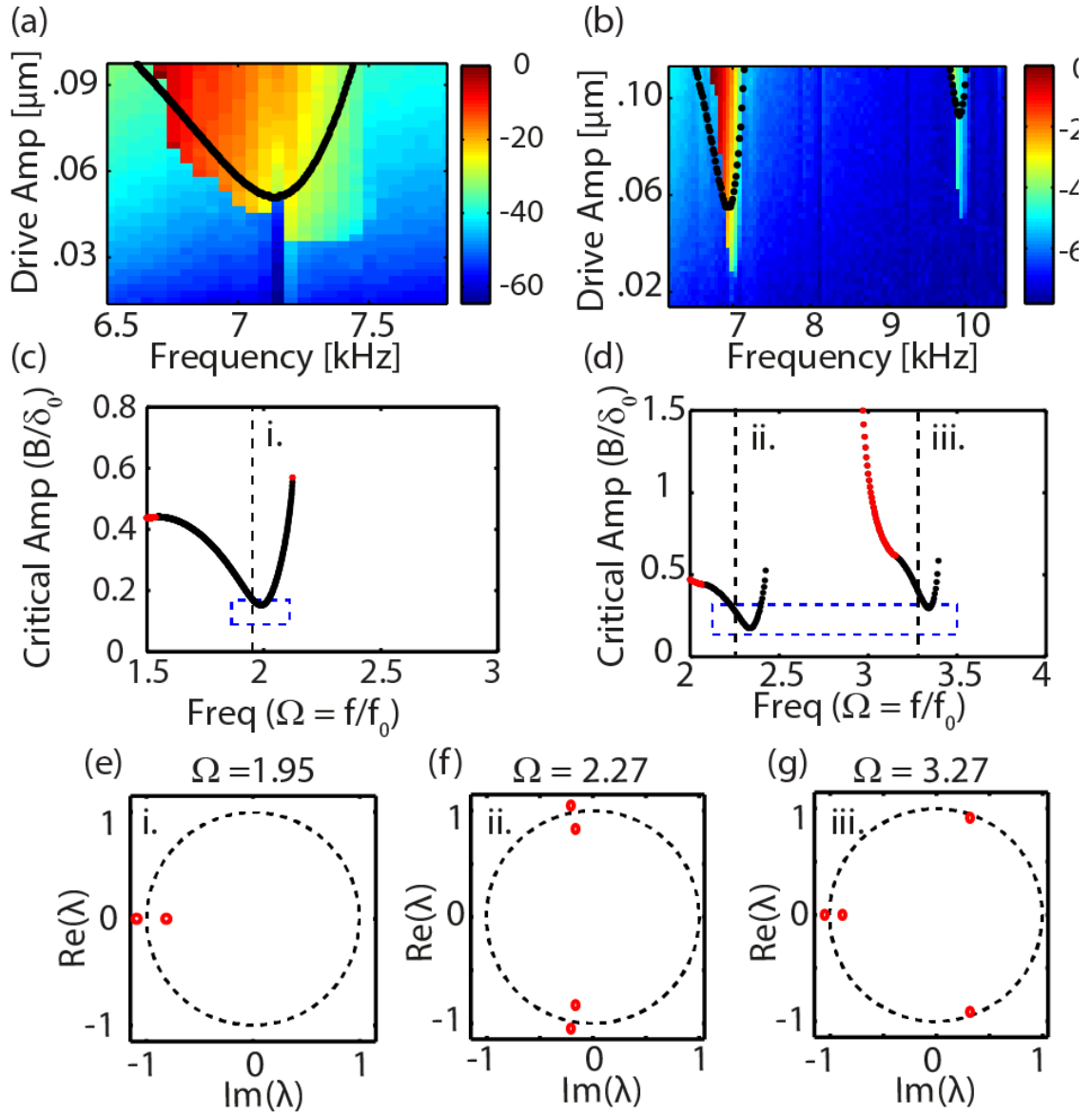


Figure 7.5: The experimentally measured bifurcation tongues observed in (a) one bead and (b) two bead systems. The color scale corresponds to maximum velocity amplitude (dB), and it demonstrates that as the mode moves further from its linear frequency, the change in dynamics becomes more drastic. The numerically calculated tongue edge is plotted directly on top of the experimental data as a black dotted line. (c) and (d) show the computational results for 1 and 2 bead chains, respectively (the units are non-dimensional). The solid points indicate where a bifurcation has occurred (i.e., a FM has left the unit circle). Red points indicate that gaps have opened between beads. The dashed rectangles indicate the parameter range for which the experimental measurements in (a) and (b). The vertical dashed lines correspond to the Floquet diagrams in (e-g). We show the unit circle to guide the eye.

The results from one and two beads help us understanding the dynamics that can take place in larger systems. Any linear combination or multiple of the mode frequencies can result in a bifurcation tongue, and for slightly larger systems the number of combinations quickly grows and so do the number of tongues. In lattices of longer length, the attenuation band that forms prevents the propagation of signals above a certain frequency. However, the previous study of a one and two bead system shows that energy can be transferred through lower frequencies. When this happens in longer chains, the attenuation band will no longer reflect all the incident signal, but instead energy will be transferred to lower frequencies that can still propagate.

In Fig. 7.6, we study the effect of the size of the system and the losses of the system on the existence and the structure of these bifurcation tongues. In particular, Fig. 7.6a shows the effect of increasing the size of the system for a given amount of losses that correspond to the non-dimensional quality factor ($Q = 27$) of the single bead system. For five beads there are already many more tongues, but they can still be distinguished. For 15 beads the tongues can no longer be distinguished and the amplitude at which the bifurcations happen is larger. This explains the sensitivity of the bifurcation that we observed for 15 beads shown and discussed in Fig. 7.1. Finally, for 25 beads we barely see the tongue structure, while for systems of 40 and 50 beads we observe no bifurcations even when driving up to 1.5 times the static overlap. Fig. 7.6b shows the effect of the losses for a given chain length ($N=15$). As the dissipation is decreased (increasing quality factor) the system can much more easily bifurcate. In both panels, we also observe that as the driving frequency increases, the appearance of bifurcations happens at larger driving amplitudes. In conclusion, as the system gets longer and/or more lossy, the

bifurcations happens at larger driving amplitude and at some point they are no longer present. Thus, there is an important interplay between the losses and the length of the system that leads to the existence or not of bifurcations and thus to the nonlinear energy transfer between phonon modes.

This could be explained from the perspective of FM as follows: The bifurcations are associated with what is called oscillatory instability, which arises from the collision of two Floquet multipliers and the associated spatially extended eigenvectors, a well-known finite-size effect. When this collision occurs, if a FM leaves the unit circle, then the solution is unstable and grows. The magnitude of this multiplier is also a measure of the strength of the instability and how quickly it grows. As discussed in Ref [17], the strength of such instabilities depends on the system size. In particular, when the size of the system is increased, the magnitude of such instabilities weakens uniformly. In other words, the unstable FMs become smaller in magnitude as the system size grows. Simultaneously, the number of such instabilities increases with system size due to the increasing density of colliding Floquet multipliers. Eventually, these instabilities vanish in the limit of an infinitely large system. Since in Hamiltonian lattices, all the FMs must lie on the unit circle, collisions result in their departure from the unit circle and are directly associated with instabilities. However, this is not the case for the driven-damped lattices. As we mentioned above, for a linearly stable periodic solution all the FMs lie on a circle of radius, $e^{-1/(2\tau f a)}$, which is smaller than one. As the dissipation increases, the Floquet multipliers have a smaller magnitude and the instability must be strong enough to allow the FM to completely leave the unit circle. Thus, it is possible for FMs to collide but still not exit the unit circle. This is due to the weak strength of the oscillatory instabilities, which becomes

weaker as the size of the lattice becomes larger. Therefore, at longer lengths there is no manifestation of bifurcations and thus no nonlinear energy transfer to the lower frequency phonon modes. This means that in shorter “periodic” systems, even relatively weak nonlinearities may become important. The bifurcations in our system occur at much lower drive amplitudes than we had previously thought, and at amplitudes where the dynamics are still weakly nonlinear and smooth. When the dynamics are weakly nonlinear the Hertzian potential can be expressed as a polynomial expansion. Therefore, periodic materials with a coupling interaction that is not strictly linear, but instead has an asymmetric or nonlinear content, may exhibit similar bifurcation dynamics. This could lead to the failure of linear approximations in other finite length systems due to weak nonlinearities.

Furthermore, we observe that at higher frequencies the bifurcations happen at higher amplitudes. This could be explained in two ways. First, the linear on-site damping in a lattice results in an increased effective damping of the higher frequency phonon modes. This is evident in our experiments for example by Fig 7.1.b, where one can see that close to the band edge, the linear response flattens out into a low pass filter and there are no longer distinct resonances. As a result, bifurcations at higher drive frequencies, which are due to the excitation of a pair of high frequency phonon modes, are less likely to appear. Second, this can also be interpreted as a consequence of the evanescent wave breaking down²⁵. The further the excitation frequency is above the band edge, the more the evanescent wave corresponding to this frequency is localized. The evanescent wave does not penetrate as deeply into the lattice at higher frequencies and the interaction between the evanescent wave and the extended modes of the crystal become increasingly smaller. This interaction becomes smaller as the chain length

increases (longer extended modes) and as the dissipation increases (weaker evanescent waves in amplitude). Correspondingly, the bifurcation instabilities occur at larger amplitudes.

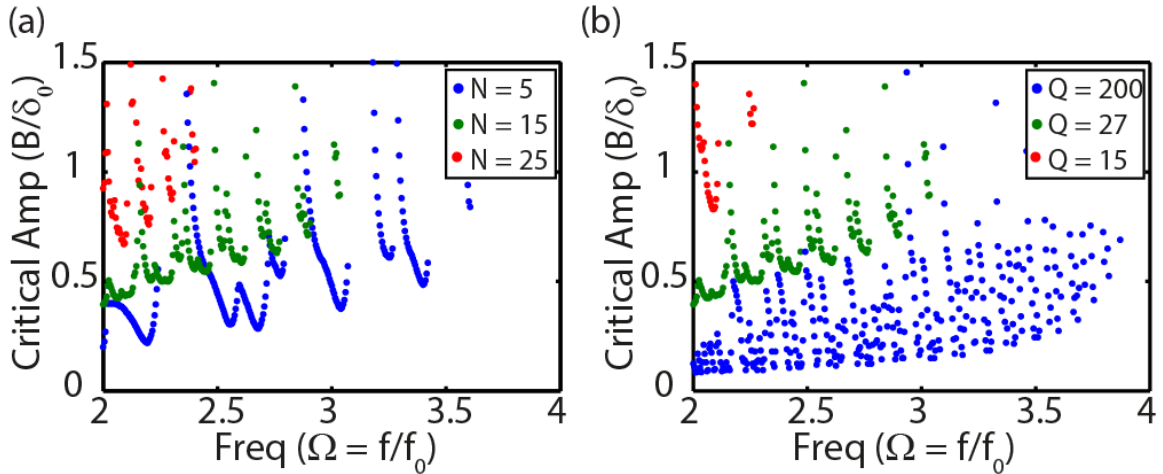


Figure 7.6: The interplay between finite size and dissipation. The points indicate a critical bifurcation amplitude, calculated using numeric. In (a) we hold the dissipation of the system constant ($Q=27$) and vary the size of the system. The individual tongues begin to overlap and the bifurcations begin to occur at higher amplitudes. In (b) the finite size ($N=15$) is held constant and the dissipation is varied. For lower dissipations the bifurcation tongues start at lower amplitude. All units shown are non-dimensional.

7.3 Conclusion

We have experimentally and computationally investigated the nonlinear resonance phenomena and the resulting bifurcation instabilities in finite, monodisperse harmonically driven one-dimensional granular chains, taking into account losses. The nonlinear bifurcation tongues arise from the finite size of the discrete system, and the tongues' shapes depend on the type of nonlinear coupling in the lattice. This dynamic response demonstrates how energy can be transferred from a single excitation signal to other frequencies fundamental to a material lattice. The nonlinear interactions in granular chains provide a completely passive mechanical

mechanism to control the transmitted frequency spectrum. The structural stability and nonlinear bifurcation dynamics of homogenous granular chains may be used in multifunctional material design where previous solutions were limited to actively controlled mechanical systems. The findings of this paper should be considered in the design of new devices consisting of nonlinear finite lattices, for example, for amplitude dependent filtering applications or for mechanical structures aiming at an enhanced frequency control of propagating waves.

7.4 Author contributions

The results from this chapter are from “Nonlinear Resonances and Energy Transfer in Finite Granular Chains”. Joseph Lydon performed the experiments and numerical analysis. Georgios Theocharis provided input and assistance with the numerical algorithm and analysis. Joseph Lydon, Georgios Theocharis, and Chiara Daraio all contributed to the writing of the manuscript.

STRONGLY NONLINEAR DYNAMIC REGIME: FREQUENCY BANDS OF STRONGLY NONLINEAR HOMOGENOUS GRANULAR SYSTEMS

Recent numerical studies on highly nonlinear, one-dimensional granular crystals composed of an infinite number of identical spherical beads in Hertzian contact showed the presence of frequency bands [Jayaprakash, et al., *Nonlinear Dynamics*, **63**: 359-385 (2011)]. These bands, denoted here as propagation and attenuation bands (PBs and ABs), are typically present in linear or weakly nonlinear periodic media; however their counterparts are not intuitive in essentially nonlinear periodic media where there is a complete lack of classical linear acoustics, i.e., in ‘sonic vacua’. Here, we study the effects of PBs and ABs on the forced dynamics of ordered, uncompressed granular systems. Through numerical and experimental techniques, we find that the dynamics of these systems depend critically on the frequency and amplitude of the applied harmonic excitation. For fixed forcing amplitude, at lower frequencies, the oscillations are large in amplitude and governed by strongly nonlinear and non-smooth dynamics, indicating PB behavior. At higher frequencies the dynamics is weakly nonlinear and smooth, in the form of compressed low amplitude oscillations, indicating AB behavior. At the boundary between the PB and the AB large-amplitude oscillations due to resonance occur, giving rise to collisions between beads and chaotic dynamics; this renders the forced dynamics sensitive to initial and forcing conditions, and hence unpredictable. Finally, we study asymptotically the near field standing wave dynamics occurring for high frequencies, well inside the AB.

8.1 Introduction

This work numerically and experimentally examines the response of an uncompressed, harmonically driven two-bead system, similar to the one discussed in the theoretical model proposed by Jayaprakash et al.¹³². In contrast to the case of statically precompressed granular crystals, uncompressed granular crystals exhibit strongly nonlinear dynamic behavior. Their response is not linearizable and there is complete absence of classical linear acoustic response. Nesterenko characterized this essentially nonlinear medium as ‘sonic vacuum’³⁵, since the linearized speed of sound (as defined in classical linear acoustics) is zero. Despite the fact that frequency bands are phenomena inherent to linear periodic systems, Jayaprakash et al.¹³² demonstrated the existence of similar propagation and attenuation bands in essentially nonlinear uncompressed granular crystals. They predicted that a one-dimensional granular crystal of infinite extent exhibits either propagation or attenuation behavior dependent on both frequency (as is the case in coupled linear periodic oscillators) and amplitude (due to the nonlinearity of the system).

The propagation band (PB) of the system is realized at lower frequencies. It is characterized by strongly nonlinear and non-smooth dynamics, a result of bead separations and collisions. This gives rise to a time-periodic train of travelling pulses, similar to solitary waves analytically predicted and experimentally demonstrated by Nesterenko³⁵. At higher frequencies, the attenuation band (AB) is characterized by a region where spatially periodic solutions cannot exist. In this regime, the system exhibits low-amplitude localized oscillations bounded by decaying spatial envelopes, similar to evanescent waves predicted in band gaps of linear media. In this high frequency regime the chain is dynamically compressed and weakly nonlinear dynamics govern the dynamical response. Jayaprakash et al.¹³² predicted that these PB and AB

exist as well in forced granular media of arbitrary length. We set out to demonstrate this behavior in a harmonically forced system of 2 beads.

8.2 Experimental results

We test the experimental setup shown in Fig. 3.2. We excite the first bead harmonically with amplitudes of approximately $0.4 \mu\text{m}$ (reproduced in the numerical simulations). Small deviations ($\pm 0.05 \mu\text{m}$) from this excitation value occur due to inherent nonlinear behavior of the actuator. We measure the force exerted on the dynamic sensor and show the existence of a high-amplitude strongly nonlinear state at low frequencies (the PB), and a low-amplitude weakly nonlinear state at high frequencies (the AB).

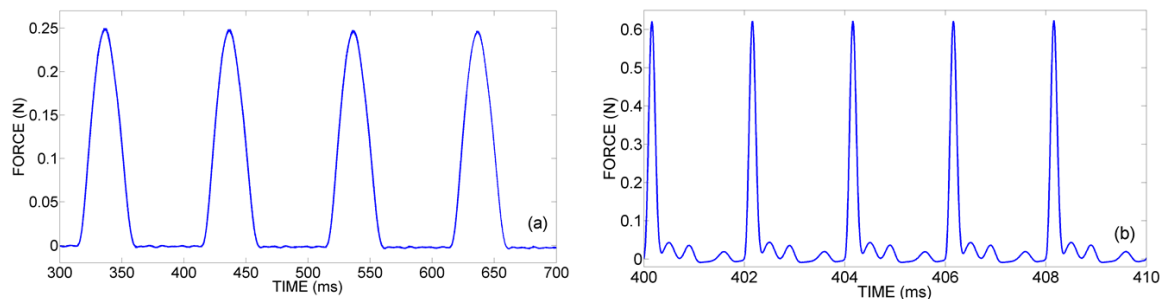


Figure 8.1: Experimental time series of the force at the dynamic sensor at (a) $f = 10$ Hz and $A = 3.951 \times 10^{-7}$ m and (b) $f = 500$ Hz and $A = 3.775 \times 10^{-7}$ m.

In Fig. 8.1a and 8.1b, we show the experimental time series of the force measured at the sensor at driving frequencies of 10 Hz and 500 Hz, respectively. These are qualitatively similar to the simulations at the same frequencies. We note a series of transmitted compressive force pulses, similar to the dynamics observed in simulation. At 10 Hz the width of this pulse is approximately half the period of the drive, however at 500 Hz this pulse width decreases below half the drive period. This is in agreement with the numerical results predicting

decreasing pulse width for higher frequencies. The maximum transmitted force is higher at 500 Hz, also in qualitative agreement with the numerical simulations. However, in the numerical simulations we observed resonance phenomena where the maximum force recorded was much higher at 1000 Hz. The experimental observation of resonances is not included in this manuscript due to difficulty in experimental repeatability.

A number of experimental uncertainties, such as misalignment, surface roughness, and bead rotations, become important and difficult to avoid as the displacement amplitudes increases at resonance. In addition, we performed an extensive series of numerical simulations of harmonically forced ordered granular systems close to the boundary between their PB and AB where nonlinear resonances are excited and the granular media execute large-amplitude oscillations. In these regions, there occur strong collisions between beads, which are well known to give rise to chaotic dynamic¹³⁴. Due to the existence of such chaotic (non-smooth) motions the forced dynamics of the forced granular systems exhibit sensitive dependence to initial and forcing conditions and become, in essence, unpredictable. This was verified in the experiments where in the resonance region (i.e., for frequencies close to the boundary between the PB and the AB) different experimental runs that were performed under identical forcing and initial conditions yielded completely different results. Hence, it appears that close to the boundary between the PB and AB the inherent chaotic dynamics of the harmonically forced system prevent the accurate measurement of the dynamic response and the resulting chaotic dynamics becomes unpredictable. We therefore omit these experimental results from further discussion herein until current research by the authors provides a better understanding and characterization of the dynamics in this regime.

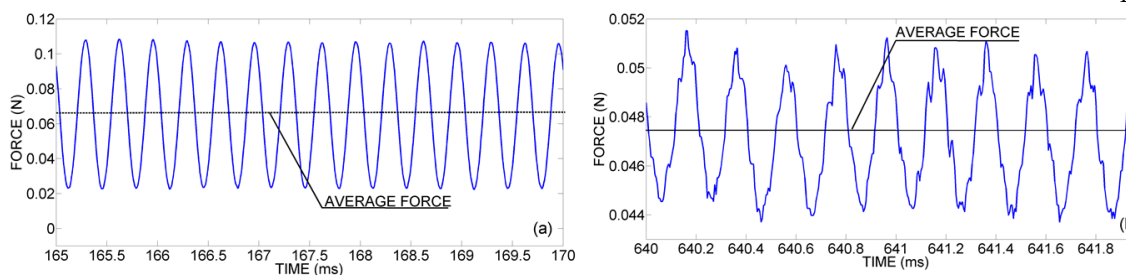


Figure 8.2: Experimental time series of the force at the dynamic sensor at (a) $f = 3000$ Hz and $A = 3.408 \times 10^{-7}$ m and (b) $f = 5000$ Hz and $A = 3.75 \times 10^{-7}$ m.

By increasing the frequency of the excitation the dynamics become again regular and fully predictable (and reproducible). Indeed, a weakly nonlinear regime is found at higher frequencies (3000 Hz – Fig. 8.2a and 5000 Hz – Fig. 8.2b), with the nonzero mean force indicating a state of sustained compression. The small-amplitude oscillations of the measured force about this mean value indicates weakly nonlinear interactions in the dynamics. Moreover, increasing the frequency decreases the transmitted force amplitude for these oscillations. A comparison of the Fourier spectrum, calculated using a discrete Fast Fourier Transform, of the dynamics in the PB (Fig. 8.3a) with those in the AB (Fig. 8.3b) underlines that fewer harmonics are excited in the weakly nonlinear phase, as is in agreement with the simulations. It should be noted that, although the experimental results do not match the numerical results quantitatively, we have good qualitative agreement between the two responses. The mismatch can be attributed to the dry friction, material damping, and other uncertainties present in the experimental setup.

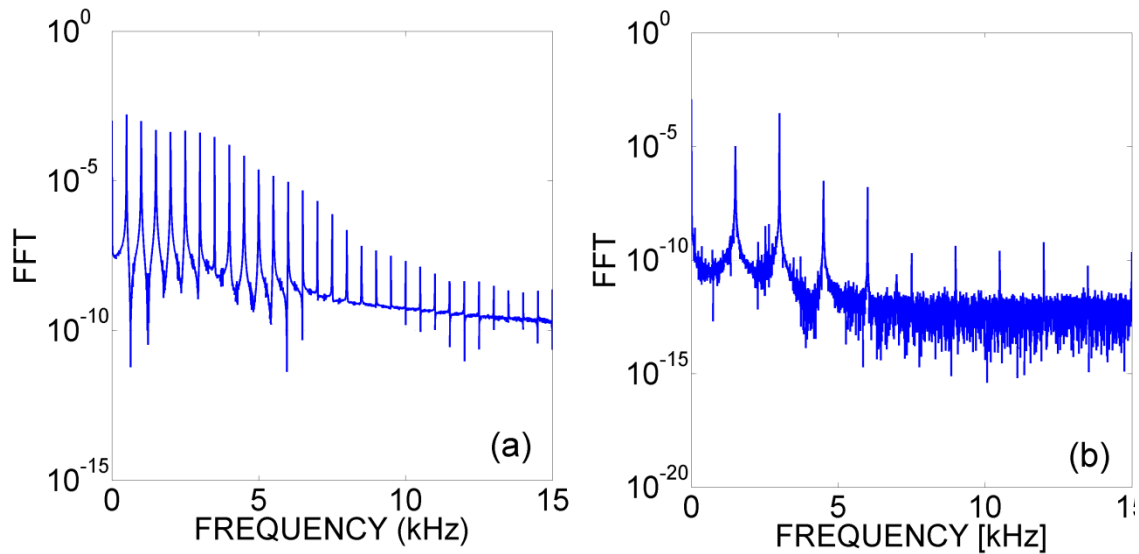


Figure 8.3: Experimental Power Spectral Densities of the force time series of (a) Fig. 8.1b: $f = 500$ Hz, and (b) Fig. 8.2a: $f = 3000$ Hz.

It should be emphasized that the reported experimental results are only for a system of two interacting beads. These experimental results show qualitative agreement with the numerical results for two beads. We believe this validates the modeling and suggests that the numerical results for longer chains hold true. At small initial compressions the experiment demonstrates similar dynamics to that predicted by our analysis for longer chains. We analytically examine the differences in dynamics for chains of arbitrary length below.

8.3 Conclusion

This paper explores in detail the presence of frequency bands in harmonically forced essentially nonlinear granular crystals. For fixed amplitude of excitation, the low-frequency dynamics is found to be strongly nonlinear, involving bead separations and collisions, and resulting in periodic trains of travelling solitary pulses. This represents the dynamics in a propagation band (PB) of the system. As we increase the drive frequency, the system enters

into a state of permanent compression which results in weakly nonlinear and smooth dynamics. In this regime the response is localized close to the actuator's excitation and rapidly decays away from it. Hence, in contrast to the propagatory dynamics realized in the PB, the higher frequency dynamics is in the form of spatially decaying (and, hence, spatially localized) standing wave oscillations. This represents the attenuation band (AB) of the system. Between these two regimes, nonlinear resonance phenomena occur, where the dynamics become chaotic due to strong collisions between beads, and the dynamics exhibit sensitive dependence on initial and forcing conditions and, hence, become unpredictable. This regime was not considered in this work and is the focus of current research by the authors.

Finally, when the dynamics is realized in the AB, we employed an asymptotic technique based on static/dynamic partitions of the bead responses, and analytically deduced that the sustained state of compression realized in the granular crystal becomes independent of the excitation frequency. However, an increase in the size of the granular crystal does increase the permanent compression, which reduces the amount of energy transferred to the crystal. These results can contribute to designing of granular-based acoustic metamaterials as acoustic filters and attenuators of externally applied periodic or transient disturbances.

8.4 Author contributions

The results from this chapter are from “Frequency Bands of Strongly Nonlinear Homogeneous Granular Systems”. Joseph Lydon performed the experiments. The analytics and numeric are done by K.R. Jayaprakash (see Appendix). Joseph Lydon, K.R. Jayaprakash, and Chiara Daraio all contributed to the writing of the manuscript.

APPLICATIONS: ENERGY HARVESTING

Nonlinear systems have been shown to outperform linear systems for energy harvesting under certain conditions¹³⁵ (see section 2.4). These methods can outperform linear systems due to the ability of a nonlinear system to transfer energy between frequencies. However, nonlinear energy harvesting systems utilize their multi-stability as an advantage over linear systems, and this means that dissipative mechanisms become important. Therefore the influence of the electrical circuit on the mechanical response is essential to more efficient energy harvesting systems. In current vibrational energy harvesting systems based on nonlinearity, the effect of electromechanical damping on the system is either ignored or so small that its effect is negligible. The following two examples present nonlinear mechanical systems that are driven to instability. This instability can only be stabilized by adding a dissipation. In this way, we use the electrical circuit to beneficially stabilize the nonlinear dynamics rather than adversely affect the state and performance of the system.

9.1 Energy harvesting inspired by thermal machines

We propose an energy harvesting system inspired by classic thermal machines. Natural energy sources present themselves as “random” or heat energy sources that must be converted to usable work energy. For the example of a steam engine, hot gas expands against a piston, transferring energy to a piston, the gas is cooled and contracts. This contraction is at a lower temperature than the expansion, and therefore when the system returns to its original state, making one full cycle, energy is transferred to the piston. This cyclical process is often

expressed in a pressure volume (PV) diagram, in which the area enclosed is the work done through a single cycle (Figure 9.1). We could also look at work done in a force-displacement cycle. We can replace the steam engine or other thermal machine, which extracts energy from the temperature difference of a hot and cold gas, with a nonlinear hysteretic spring.

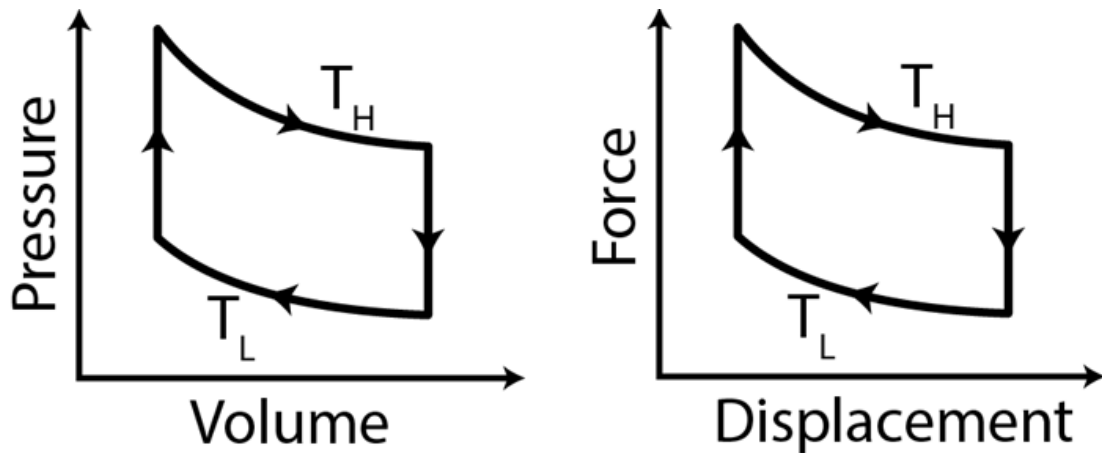


Figure 9.1: (Left) PV diagram for a traditional thermal machine such as a steam engine. (Right) We propose an energy harvesting system inspired by a thermal machine, in which the constituent harvesting is now a nonlinear hysteretic spring.

This hysteresis response is very similar to the hysteresis response that we observed in the tunable stiffness experiment, except that the cycle goes in the other direction. In the extraordinary tunable stiffness experiment, we demonstrate a damping response where the hysteresis originates from the two state solution of the nonlinear system past the bifurcation. If we can engineer a system with a hysteretic loop that goes in the opposite direction to the granular crystals, then the system acts as an energy harvester or “nonlinear thermal machine” (Figure 9.1).

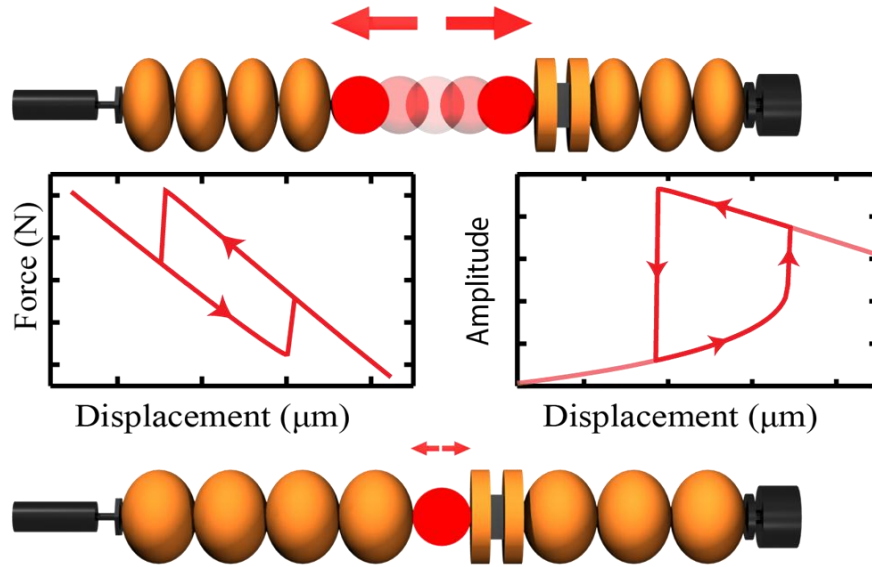


Figure 9.2: (Left) Force-displacement for the hysteretic damping mechanism observed in a granular crystal. (Right) The nonlinear amplitude response of the defect mode that results in the force-displacement relation to the left.

We propose a nonlinear energy harvesting system based on a nonlinear spring with bifurcation dynamics similar to the granular chain. In the granular example with hysteretic damping, the force interaction of the nonlinear defect mode can be approximated by a Taylor expansion, $F \sim kx + \alpha x^2 + \beta x^3$. The term with alpha describes the thermal expansion of the defect mode causing an extra force at the boundary. This results in a dependence of the force-displacement response on the amplitude-displacement response. This means a bi-stability in the amplitude response also causes a hysteresis. However, this particular system follows the low amplitude solution in compression and the high amplitude solution in extension, exactly the opposite of what we need for an energy harvester.

By changing the directionality of the bistable amplitude response, we can also change the hysteresis to go from damping to harvesting. In nonlinear dynamical systems, such as the

Duffing oscillator, it is well known that changing the sign of the cubic term, β , also changes the direction of the softening or hardening response of the resonance. In the granular crystal, the cubic term is negative, resulting in a softening potential. However, if the cubic term were positive, the potential would be hardening, and the amplitude loop could be reversed. We therefore search for a model system that has a hardening nonlinearity to demonstrate this idea of energy harvesting inspired by thermal machines.

Strings are systems with known hardening nonlinear responses¹³⁶. Therefore we study a guitar string clamped between a cantilever and a fixed wall (Fig. 9.3). In our simplified model there is an energy source that drives the vibration of the string, which transfers energy to the cantilever. We start by considering a harmonic driving source, and although this is a gross approximation to sources in real systems, it provides intuition into the phenomenology.

When the string is driven with a harmonic excitation, it reaches a steady state amplitude. This vibration amplitude causes an increase of the average length of the string. This results in an increased tension on the string, causing two effects. The first is the hardening, or stiffening, nonlinearity that causes the third order nonlinear term to be positive, $\beta > 0$. The second is the additional tension on the cantilever which causes it to displace. This is schematically represented in the right panel of Figure 9.3. The displacement of the cantilever also has a back action on the string by causing a detuning, or softening. These two effects happen at different speeds and together result in the energy harvesting response of the nonlinear string-cantilever system.

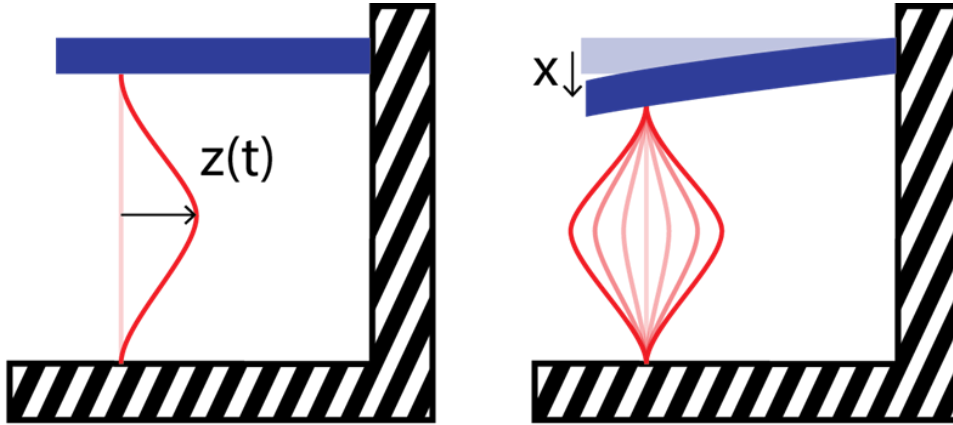


Figure 9.3: The string-cantilever system. (Left) The vibration coordinate of the string is defined as $z(t)$. (Right) The coordinate of the cantilever is defined as $x(t)$. As the amplitude of the string vibration increases there is an additional tension pulling on the cantilever.

In order to support the qualitative argument above, we begin with a partial differential equation describing the motion of a beam¹³⁷ of which a string is a limiting case and attempt to reduce this to a more manageable second order ordinary differential equation. We follow a derivation similar to Postma et al.¹³⁷

$$EI \frac{\partial^4 w}{\partial x^4} - \frac{EA}{L} \left[X + \frac{1}{2} \int_0^L \left(\frac{\partial w}{\partial x} \right)^2 dx \right] \frac{\partial^2 w}{\partial x^2} + \rho A \frac{\partial^2 w}{\partial t^2} - iB = 0 \quad (9.1)$$

The equation includes a term for bending, tension, inertia, and the excitation applied to the beam, where E, I, A, L, X, ρ, i , and B are the Young's modulus, moment of inertia, cross sectional area, length, initial tension, density, current through the beam, and perpendicular magnetic field. Using a Galerkin method, we apply a test function,

$$\phi(x) = \left(\sqrt{\frac{2}{3}} \right) \left[1 - \cos\left(\frac{2\pi x}{L}\right) \right], \quad (9.2)$$

and reduce the PDE to a second order ode,

$$m_z \ddot{z} + b_z \dot{z} + (k_z + 2\alpha x)z + \beta_z z^3 = F(t), \quad (9.3)$$

where each of the parameters listed depend on the material constants chosen in (Eq. 9.1), and where $m_z = \rho AL$, $k_z = (2\pi)^4 EI/(3L^3)$, $\alpha = 2\pi^2 EA/(3L^2)$, $\beta_z = (2\pi)^4 EA/(18L^3)$, and b_z is a viscous dissipation added to the system to reflect the dissipation in the real system. The equation is the same as a for a driven-damped Duffing oscillator⁸. Note that in this equation $\beta_z > 0$, which means that the dynamics are stiffening instead of softening, as in the case of the granular chain. As the string starts to vibrate to larger amplitudes the increase in time-averaged length is also accompanied by an increase in the average tension on the string. This also causes a detuning to higher frequencies when the string is driven to higher amplitudes, hence the stiffening nature of the string. When the equation is driven to higher amplitudes around the natural resonance of the system, the amplitude response for the Duffing oscillator is hysteretic. The detuning of the system, i.e., the difference of the drive frequency from the natural frequency of the system controls the amplitude of the response. Equation (9.3) also includes a coupling between the string and cantilever element. As the cantilever relaxes, this affects the linear resonant frequency. We can model the cantilever as a linear oscillator driven by the amplitude of the string,

$$m_x \ddot{x} + b_x \dot{x} + k_x x = -\alpha z^2, \quad (9.4)$$

where k_x , b_x , and m_x are the bending stiffness, damping, and effective mass of the cantilever beam, respectively. In addition, the cantilever's mass and stiffness must be designed so that the motion is slow compared to the string, allowing the string to remain on the steady state solution. The cantilever's motion has the effect of modulating the string's frequency. This allows us to move the bifurcated string system around the hysteretic loop through the motion of the cantilever (Fig. 9.4).

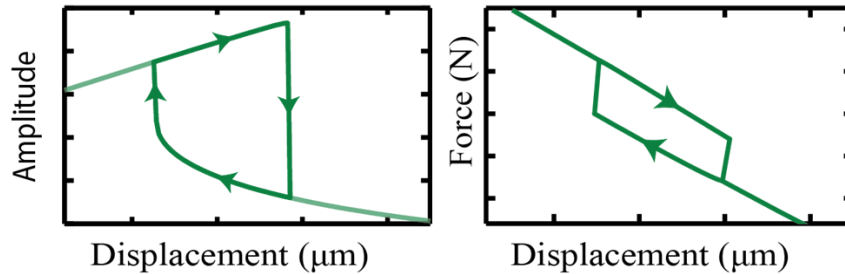


Figure 9.4: The displacement of the cantilever modulates the resonance frequency of the string. (Left) This results in a amplitude response for the string that is modulated by the cantilever's displacement, and (Right) a force-displacement relation for the cantilever that has a similar hysteresis to a thermal machine.

As the cantilever increases its displacement, $x(t)$, the amplitude of the string, $z(t)$, follows the high amplitude solution until the system falls over the bifurcation. As the displacement of the cantilever decreases, the amplitude force response follows the low amplitude solution. Equation (9.4) shows that the cantilever is driven by the string's amplitude. This results in a hysteretic force displacement curve for the cantilever, in which the string transfers energy to the cantilever through each cycle. To verify this we simulate the coupled system with no dissipation for the cantilever, $b_x=0$ (Fig. 9.5).

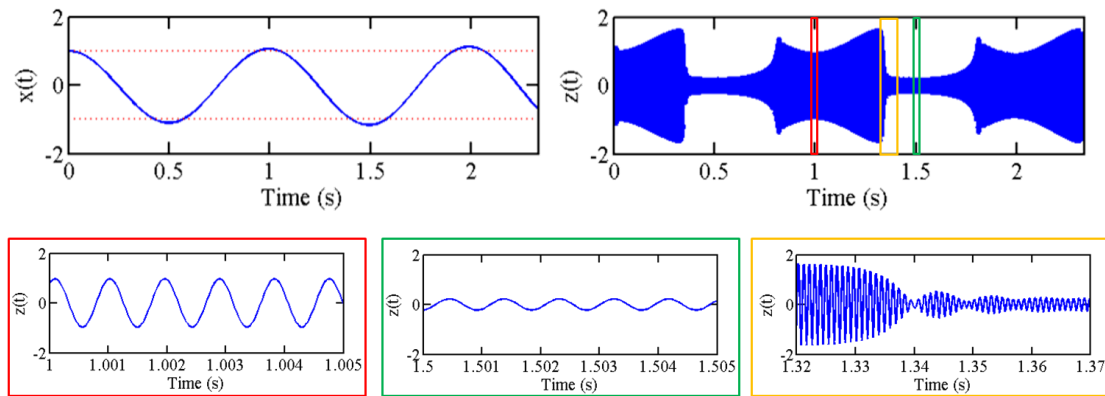


Figure 9.5: Cantilever (Top Left) time series and string (Top Right) time series. The string is driven by a harmonic signal, while the cantilever causes a slow variation of the resonance frequency. (Bottom Left) String time series for the high amplitude solution. (Bottom Middle) String time series for the low amplitude solution. (Bottom Right) String time series showing the transient dynamics..

In Figure 9.5 we simulate the coupled spring cantilever system with the cantilever given an initial potential energy in the form of a nonzero starting displacement. The string is driven harmonically with its frequency modulated by the slow movement of the cantilever. Figure 9.5 shows how the string's displacement cyclically moves from a high amplitude to a low amplitude solution, following the position of the cantilever. Each time through this cycle, the string transfers energy to the cantilever system. This can be seen in the growing amplitude of the cantilever.

What makes this nonlinear energy harvesting system different from many other solutions is the effect of electrical coupling. Without the electrical coupling the amplitude of the cantilever will grow, and the system is not stable. It is only the additional presence of damping that stabilizes the system. In this example the electrical coupling is a necessary component instead of having a detrimental effect.

9.1.1 Conclusion and outlook

While these results are preliminary and present a paradigm for developing energy harvesting materials, there are a few things that we have learned. The first is that we have demonstrated energy transfer between two different frequency modes of completely arbitrary frequency. The energy is transferred from high to low frequencies, where the frequencies are determined by the natural frequencies of the two structures. Second is that the energy transfer is synchronous. This means that if we attached a second string to the cantilever it can be pushed through its own hysteresis in phase with the other string. This is because the modulation of each string is determined by the cantilever itself.

9.2 Parametrically driven energy harvesting

The second approach that we present for an energy harvesting system is based on the parametric type resonances observed in the finite granular chains. We look to use these instabilities as an instance in which the mechanical dissipation does not balance the energy injected into the system through excitations. By introducing a coupled electrical circuit, we propose a mechanism to stabilize the mechanical system and more efficiently harvest energy.

9.2.1 Project goal

We propose a novel concept for energy harvesting based on nonlinear dynamical systems that will more efficiently harvest energy from both small and large mechanical excitations. The design approach we propose relies on creating mechanical systems that are both nonlinear and parametric, a combination that leads to a host of advantages over traditional energy harvesting approaches.

There are three primary objectives of this project: (i) to develop a theoretical model for energy harvesting in a parametric nonlinear system that will be compared with results from traditional linear systems; (ii) implement a prototype device, a sphere in contact with a vibrating surface, to harvest mechanical energy through electromechanical coupling; and (iii) to use Finite Element Methods design nonlinear geometries that also contain parametric resonances, and can implement the theory across a range of power and size scales.

9.2.2 Introduction

Mechanical resonances are basic physical phenomena, present in all engineering systems and structures. Resonance occurs when a structure experiences a periodic force at one of its natural frequencies, which depends on the design geometry and constituent materials. When a structure is at resonance there is a buildup of energy, and it generally undergoes large oscillations and deformations. In most design efforts, resonances are commonly avoided due to their potential to cause catastrophic failure of infrastructures, for example the Tacoma Narrows Bridge collapse in 1940. The Taipei 101 building, the tallest in the world until 2010, uses a tunable mass damper to protect the structure against resonances that can arise from wind or earthquakes. In this proposed work, we look at resonances as a means to achieve large oscillations for renewable energy conversion. Initially, we planned to explore a proof-of-concept device that will harvest energy from ambient sources (see Table 1). Then, since the approach would only rely on fundamental physical principles, the design would be appropriately modified to produce energy on a larger scale.

Mechanical energy conversion and production typically falls into one of two categories depending on the scale. (i) For power sources that are more than a few watts, e.g., wind or

hydrodynamic power, conventional turbine technology is used. (ii) When power levels are less than a watt, the process is typically considered energy harvesting or scavenging. For this, one of the most prolific designs is a cantilever-based piezoelectric device. The efficiency of such cantilever-designs is limited by the piezoelectric materials, which can harvest only a small fraction of energy dispersed over the whole structure¹³⁸, and only work over a small frequency bandwidth. In this proposal, we are interested in designing new and improved approaches for harvesting energy from small ambient mechanical excitations, using nonlinear dynamical systems. The fundamental concepts proposed here as a proof-of-principle could be extended to designing energy production solutions also for large power sources.

Nonlinear dynamical systems, for example simple pendula, bending beams, and many optical materials, have an amplitude dependent response. The dynamic response of these systems is different for small and large mechanical excitations. The design approach we propose relies on creating mechanical systems that are both nonlinear and parametric, a combination that leads to a host of advantages over traditional linear dynamical systems. For example, nonlinear parametric systems can be driven at resonance to amplify their mechanical deformation, and subsequently their oscillation can be accurately stabilized through geometric nonlinearities. The simplest example of a nonlinear parametric system is a spherical particle confined by rigid walls and driven by a mechanical vibration. This system is highly tunable, from weakly to strongly nonlinear, and is extremely easy to implement. We will use this simple toy-model to provide a theoretical and experimental proof of concept for new energy harvesting approaches, evaluate their efficiency, and propose scalable designs for practical engineering solutions. We will design and test an energy harvesting system based on a single spherical particle confined between rigid

boundaries. We will then demonstrate how its dynamic response can provide a completely new approach to localizing and harvesting mechanical energy. In the last few months of the planned work, we will propose designs adaptable to larger mechanical sources and different ambient conditions.

Vibration source	Peak frequency (Hz)	Acceleration amplitude (m/s^2)
Washing machine	109	0.5
External windows	100	0.7
Car engine compartment	200	12
Vehicles	5-2000	0.5-110
Refrigerator	240	0.1

Table 9.1: Example of common mechanical energy sources for small energy harvesting/scavenging. Source: "Piezoelectric Energy Harvesting Devices for Low Frequency Vibration Applications" Dongna Shen, PhD Thesis, Auburn University (2009)

9.2.3 Theoretical investigation

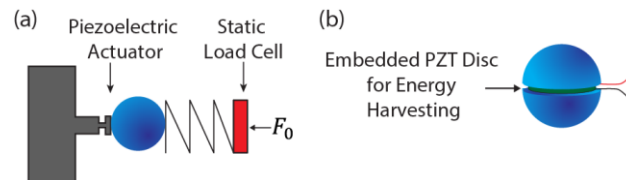


Figure 9.6: Experimental setup for a Spherical Bead Compressed Against a Piezoelectric Actuator. (a) A prototype schematic for the proof of concept energy harvesting device. This is mathematically represented in eq. 1. (b) An embedded piezoelectric sensor acts as a high impedance voltage source.

The fundamental response of both nonlinear and parametrically driven systems is well understood and has been extensively studied⁵². However, these phenomena have not yet been combined and investigated to design structures for enhanced energy harvesting and production. A sphere compressed with a force, F_0 , against a vibrating surface (Fig. 9.6), is

characterized by both a nonlinear mechanical response (deriving from the geometry of the contact between the sphere and the vibrating surface) and a parametric excitation (the ambient vibration). These physical phenomena and the response of this simple system can be described by the following model³⁵:

$$m\ddot{u} = F_0 \left[1 - u + \left(\frac{A}{F_0} \right)^{\frac{2}{3}} B \cos(\omega t) \right]_+^{3/2} - F_0 - \gamma \dot{u}, \quad (9.5)$$

where m is the mass of the sphere, u is the displacement of the bead, γ is the bead's dissipation coefficient, and A is the Hertzian spring constant. B and ω are the vibration source's amplitude and frequency, respectively. The bracket, $[x]_+ = \max(0, x)$, indicates a tensionless behavior in which there is no force attracting the bead to the vibrating surface after they separate.

The most important part of this model is the exponent of $3/2$. It results in two important physical phenomena for our proposed approach. First, the vibrating surface does not just provide acceleration to the sphere, but also acts as a parametric drive periodically varying the spring constant of the system. Second, the force between the spherical bead and flat vibrating surface is nonlinear, meaning that the effective spring constant of the system also depends on the amplitude of the vibration.

A common example of a parametric drive is a child on a swing, where the child periodically adjusts his position to increase the amplitude of his swinging. In certain frequency bands, called parametric tongues, the dynamics leads to oscillations that grow exponentially in

amplitude, even in the presence of dissipation. This phenomena is very exciting, especially in the context of energy harvesting. The structure continues to gain energy until the system collapses or is stabilized. This type of oscillator is oftentimes referred to as a self-exciting oscillation and was identified as the source that led to the ultimate collapse of the Tacoma Narrows Bridge¹³⁹. Figure 9.7a shows a parametric tongue observed in a driven single spherical particle. There is sudden discontinuous change in the dynamics above a threshold driving amplitude, a bifurcation, in which the oscillation amplitude of the bead is clearly larger. In fact, after this sudden change, as much as 21 times more energy is being transferred from the vibrating surface to the bead.

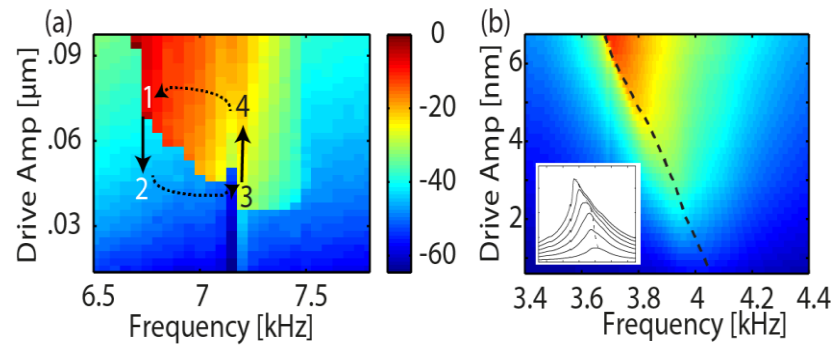


Figure 9.7: Nonlinear Detuning and Parametric Energy Harvesting. a, The parametric tongue separating regions of low and high amplitude oscillations for a single sphere particle. We would like to test the indicated cycle as a mechanism to collect mechanical energy. Initially the system would start at (1). By removing energy the system loses amplitude (2), causing the system to retune (3). This causes the amplitude to increase (4) until the nonlinearity again detunes the system (upper dotted arrow). b, The detuning of the natural frequency of the nonlinear spherical particle serves to stabilize and the dynamics. At higher amplitudes, the natural frequency decreases. (colorbar units are in dBs)

In addition, Figure 9.7a shows that the dynamics are stable above the cutoff drive amplitude. This means there is not a collapse or destructive deformation due to an exponentially increasing amplitude. Instead nonlinearity acts to prevent catastrophic events. Figure 9.7b

shows the dependence of the natural frequency of the system on amplitude. As the amplitude increases, the natural frequency decreases. This pushes the system to the edge of the parametric tongue frequency band, and prevents continuous growth in amplitude.

Using this proven fundamental physics, we will design systems that self-correct, balance, and protect themselves as a new approach for efficient energy harvesting.

9.3 Author contributions

The concept for the string-cantilever energy conversion system was developed by Joseph Lydon and Marc Serra-Garcia together. The parametrically driven system was developed by Joseph Lydon, and Chiara Daraio contributed to the writing of the manuscript.

CONCLUSIONS & RESEARCH SUMMARY

The granular crystal is a great model system to study dynamics that result from the combination of nonlinearity and broken periodicity. The similarity of the modeling and dynamical equation makes these results easily relatable to other materials systems. In the linear approximation, the granular crystal is a coupled mass spring model, the same as that used to explain the heat capacity and phonon branches in perfect crystals^{95,140}. In the nonlinear case, the interaction law can be approximated through a Taylor expansion, which helps extend the physics to other systems with nonlinearity.

In this thesis, we demonstrate new phenomena that result from the combination of nonlinearity and finite size. We show that the local defect mode, introduced from a resonant defect, has a spatial profile that can be tuned using an external compression. This could be used for applications in designing for tunable wave speed propagation. We demonstrate how the stiffness of a material can be tuned at any displacement or strain point. In a granular crystal this tuning pushes the incremental stiffness in the negative direction, however in lattices with other potentials, this could be used to engineer positive infinite stiffness. We show how nonlinearity in finite granular chains allows energy to propagate instead of the system acting as a mechanical filter. This can be used as a way to selectively transfer high frequency energy through lower frequency phonon modes. And finally we demonstrate two approaches to nonlinear energy harvesting, in which the nonlinearity is used to overcome the fundamental

limitations in linear systems. We demonstrate how nonlinearity can and should be used when designing materials or systems for targeted properties.

While the granular crystal is a specific example of a nonlinear lattice with broken periodicity, these results apply to a broader range of fields. Our results on tuning a resonant defect mode extend to other condensed matter systems where defect modes are important. For example, in optical systems, the arrangement of defects supporting localized modes has been used to achieve slow group velocities in coupled optical resonant wave guides⁵⁰. One question is, how can a local resonant defect be implemented and controlled in similar optical system to achieve tunable ultraslow group velocity?

Our results of extraordinary tunable stiffness in lattices (chapter 6) shows how the incremental stiffness can be tuned to arbitrary values. This effect would be quite interesting in a nonlinear optical system. Specifically, is it possible to tune the effective dielectric constant of a material to arbitrary values? In our analysis on energy harvesting, we show a defect mode driven at a high frequency to control the effective response at lower frequencies. This is especially interesting in enhanced coupling, where frequencies are not necessarily matched. Could this mechanism enable targeted energy transfer between a high frequency optical mode and lower frequency phonon mode?

The last chapter discussed two future applications of this work in the field of energy harvesting. While the ideas have been inspired by our studies of the physics in nonlinear lattices with broken periodicity, they are presented in simplified nonlinear systems, i.e., a coupled string-cantilever or single parametric oscillator. The models are simplified with the

hope that they can be applied to other dynamical systems. The next step for these energy harvesting examples is figuring out how to implement the physics into realistic materials and structural systems. Since many energy sources are stochastic, it is also important to study the dynamics of these physical systems under stochastic excitations.

These are just some of the questions that could be explored in future research projects that follow this research thesis. More generally this research shows that it is important to look at the physics that may be missed when making linear approximations. Oftentimes the nonlinearity provides rich dynamics that have potential in applications.

BIBLIOGRAPHY

- 1 Ernst, G., Broholm, C., Kowach, G. R. & Ramirez, A. P. Phonon density of states and negative thermal expansion in ZrW₂O₈. *Nature* **396**, 147-149 (1998).
- 2 Ashcroft, N. W. & Mermin, N. D. *Solid state physics*. (Saunders College, 1976).
- 3 Ford, J. Equipartition of Energy for Nonlinear Systems. *Journal of Mathematical Physics* **2**, 387-393, doi:doi:<http://dx.doi.org/10.1063/1.1703724> (1961).
- 4 Wong, C. W. *et al.* Strain-tunable silicon photonic band gap microcavities in optical waveguides. *Applied Physics Letters* **84**, 1242-1244, doi:doi:<http://dx.doi.org/10.1063/1.1649803> (2004).
- 5 Huang, M. *et al.* Phonon softening and crystallographic orientation of strained graphene studied by Raman spectroscopy. *Proceedings of the National Academy of Sciences* **106**, 7304-7308, doi:10.1073/pnas.0811754106 (2009).
- 6 Huang, M., Yan, H., Heinz, T. F. & Hone, J. Probing Strain-Induced Electronic Structure Change in Graphene by Raman Spectroscopy. *Nano Letters* **10**, 4074-4079, doi:10.1021/nl102123c (2010).
- 7 Yan, W. *et al.* Strain and curvature induced evolution of electronic band structures in twisted graphene bilayer. *Nat Commun* **4**, doi:10.1038/ncomms3159 (2013).
- 8 Nayfeh, A. H. & Mook, D. T. *Nonlinear Oscillations*. (Wiley, 2008).
- 9 Haasen, P. *Physical Metallurgy*. (Cambridge University Press, 1996).
- 10 Brillouin, L. *Wave Propagation in Periodic Structures: Electric Filters and Crystal Lattices*. (Dover Publications, 1953).
- 11 John, S. Strong localization of photons in certain disordered dielectric superlattices. *Phys. Rev. Lett.* **58**, 2486-2489 (1987).
- 12 Queisser, H. J. & Haller, E. E. Defects in Semiconductors: Some Fatal, Some Vital. *Science* **281**, 945-950, doi:10.1126/science.281.5379.945 (1998).
- 13 Balandin, A. A. Thermal properties of graphene and nanostructured carbon materials. *Nat Mater* **10**, 569-581 (2011).
- 14 Wei, Y. *et al.* The nature of strength enhancement and weakening by pentagon-heptagon defects in graphene. *Nat Mater* **11**, 759-763, doi:<http://www.nature.com/nmat/journal/v11/n9/abs/nmat3370.html#supplementary-information> (2012).
- 15 Zandiatashbar, A. *et al.* Effect of defects on the intrinsic strength and stiffness of graphene. *Nat Commun* **5**, doi:10.1038/ncomms4186 (2014).
- 16 Zheludev, N. I. The Road Ahead for Metamaterials. *Science* **328**, 582-583, doi:10.1126/science.1186756 (2010).
- 17 Liu, Z. *et al.* Locally Resonant Sonic Materials. *Science* **289**, 1734-1736, doi:10.1126/science.289.5485.1734 (2000).
- 18 Fang, N. *et al.* Ultrasonic metamaterials with negative modulus. *Nat Mater* **5**, 452-456, doi:http://www.nature.com/nmat/journal/v5/n6/supinfo/nmat1644_S1.html (2006).
- 19 Graeme, W. M. New metamaterials with macroscopic behavior outside that of continuum elastodynamics. *New Journal of Physics* **9**, 359 (2007).
- 20 Hess, O. *et al.* Active nanoplasmonic metamaterials. *Nat Mater* **11**, 573-584 (2012).

- 21 Florijn, B., Coulais, C. & van Hecke, M. Programmable Mechanical Metamaterials. *Phys. Rev. Lett.* **113**, 175503 (2014).
- 22 Hertz, H. in *Journal für die reine und angewandte Mathematik (Crelle's Journal)* Vol. 1882 156 (1882).
- 23 Geniet, F. & Leon, J. Energy Transmission in the Forbidden Band Gap of a Nonlinear Chain. *Phys. Rev. Lett.* **89**, 134102 (2002).
- 24 Geniet, F. & Leon, J. Nonlinear supratransmission. *Journal of Physics: Condensed Matter* **15**, 2933 (2003).
- 25 Leon, J. Nonlinear supratransmission as a fundamental instability. *Physics Letters A* **319**, 130-136, doi:<http://dx.doi.org/10.1016/j.physleta.2003.10.012> (2003).
- 26 Lydon, J. *et al.* Frequency bands of strongly nonlinear homogeneous granular systems. *Physical Review E* **88**, 012206 (2013).
- 27 Man, Y., Boechler, N., Theocharis, G., Kevrekidis, P. G. & Daraio, C. Defect modes in one-dimensional granular crystals. *Physical Review E* **85**, 037601 (2012).
- 28 Marín, J. L., Falo, F., Martínez, P. J. & Floría, L. M. Discrete breathers in dissipative lattices. *Physical Review E* **63**, 066603 (2001).
- 29 Marín, J. L. & Aubry, S. Finite size effects on instabilities of discrete breathers. *Physica D: Nonlinear Phenomena* **119**, 163-174, doi:10.1016/s0167-2789(98)00077-3 (1998).
- 30 Herbold, E. B., Kim, J., Nesterenko, V. F., Wang, S. Y. & Daraio, C. Pulse propagation in a linear and nonlinear diatomic periodic chain: effects of acoustic frequency band-gap. *Acta Mech.* **205**, 85-103, doi:10.1007/s00707-009-0163-6 (2009).
- 31 Boechler, N., Yang, J., Theocharis, G., Kevrekidis, P. G. & Daraio, C. Tunable vibrational band gaps in one-dimensional diatomic granular crystals with three-particle unit cells. *J. Appl. Phys.* **109**, doi:10.1063/1.3556455 (2011).
- 32 Boechler, N., Theocharis, G. & Daraio, C. Bifurcation-based acoustic switching and rectification. *Nat. Mater.* **10**, 665-668, doi:10.1038/nmat3072 (2011).
- 33 Nesterenko, V. F. Propagation of nonlinear compression pulses in granular media. *J Appl Mech Tech Phys* **24**, 733-743, doi:10.1007/BF00905892 (1983).
- 34 Sen, S. & Mohan, T. R. K. Dynamics of metastable breathers in nonlinear chains in acoustic vacuum. *Physical Review E* **79**, 036603 (2009).
- 35 Nesterenko, V. *Dynamics of Heterogeneous Materials*. (Springer, 2001).
- 36 Serra-Garcia, M., Lydon, J. & Daraio, C. Extraordinary stiffness tunability through thermal expansion of nonlinear defect modes. *arXiv preprint arXiv:1411.5242* (2014).
- 37 Lydon, J., Serra-Garcia, M. & Daraio, C. Local to Extended Transitions of Resonant Defect Modes. *Phys. Rev. Lett.* **113**, 185503 (2014).
- 38 Yablonoitch, E. Inhibited Spontaneous Emission in Solid-State Physics and Electronics. *Phys. Rev. Lett.* **58**, 2059-2062 (1987).
- 39 Blanco, A. *et al.* Large-scale synthesis of a silicon photonic crystal with a complete three-dimensional bandgap near 1.5 micrometres. *Nature* **405**, 437-440 (2000).
- 40 Kushwaha, M. S., Halevi, P., Dobrzynski, L. & Djafari-Rouhani, B. Acoustic band structure of periodic elastic composites. *Phys. Rev. Lett.* **71**, 2022-2025 (1993).
- 41 Sigalas, M. & Economou, E. N. Band structure of elastic waves in two dimensional systems. *Solid State Communications* **86**, 141-143, doi:[http://dx.doi.org/10.1016/0038-1098\(93\)90888-T](http://dx.doi.org/10.1016/0038-1098(93)90888-T) (1993).
- 42 Kushwaha, M. S., Halevi, P., Dobrzynski, L. & Djafari-Rouhani, B. Acoustic band structure of periodic elastic composites. *Phys. Rev. Lett.* **71**, 2022 (1993).

- 43 Maldovan, M. Sound and heat revolutions in phononics. *Nature* **503**, 209-217, doi:10.1038/nature12608 (2013).
- 44 Wagner, M. Influence of Localized Modes on Thermal Conductivity. *Physical Review* **131**, 1443-1455 (1963).
- 45 Torres, M., Montero de Espinosa, F. R., García-Pablos, D. & García, N. Sonic Band Gaps in Finite Elastic Media: Surface States and Localization Phenomena in Linear and Point Defects. *Phys. Rev. Lett.* **82**, 3054-3057 (1999).
- 46 Joannopoulos, J. D., Johnson, S. G., Winn, J. N. & Meade, R. D. *Photonic Crystals: Molding the Flow of Light (Second Edition)*. (Princeton University Press, 2011).
- 47 Rudykh, S. & Boyce, M. C. Transforming Wave Propagation in Layered Media via Instability-Induced Interfacial Wrinkling. *Phys. Rev. Lett.* **112**, 034301 (2014).
- 48 Milton, G. W. & Willis, J. R. On modifications of Newton's second law and linear continuum elastodynamics. *Proceedings of the Royal Society A: Mathematical, Physical and Engineering Science* **463**, 855-880, doi:10.1098/rspa.2006.1795 (2007).
- 49 Gantzounis, G., Serra-Garcia, M., Homma, K., Mendoza, J. M. & Daraio, C. Granular metamaterials for vibration mitigation. *J. Appl. Phys.* **114**, -, doi:doi:<http://dx.doi.org/10.1063/1.4820521> (2013).
- 50 Yariv, A., Xu, Y., Lee, R. K. & Scherer, A. Coupled-resonator optical waveguide: a proposal and analysis. *Opt. Lett.* **24**, 711-713, doi:10.1364/OL.24.000711 (1999).
- 51 Stefanou, N. & Modinos, A. Impurity bands in photonic insulators. *Physical Review B* **57**, 12127-12133 (1998).
- 52 Nayfeh, A. & Mook, D. *Nonlinear Oscillations*. (John Wiley & Sons, 1979).
- 53 Turing, A. M. The Chemical Basis of Morphogenesis. *Philosophical Transactions of the Royal Society of London. Series B, Biological Sciences* **237**, 37-72, doi:10.1098/rstb.1952.0012 (1952).
- 54 Lorenz, E. N. Deterministic Nonperiodic Flow. *Journal of the Atmospheric Sciences* **20**, 130-141, doi:10.1175/1520-0469(1963)020<0130:DNF>2.0.CO;2 (1963).
- 55 Strogatz, S. H. *Nonlinear Dynamics and Chaos: With Applications to Physics, Biology, Chemistry, and Engineering*. (Westview Press, 1994).
- 56 Lattanzi, L., Raney, J. R., De Nardo, L., Misra, A. & Daraio, C. Nonlinear viscoelasticity of freestanding and polymer-anchored vertically aligned carbon nanotube foams. *J. Appl. Phys.* **111**, -, doi:doi:<http://dx.doi.org/10.1063/1.3699184> (2012).
- 57 Franken, P. A., Hill, A. E., Peters, C. W. & Weinreich, G. Generation of Optical Harmonics. *Phys. Rev. Lett.* **7**, 118-119 (1961).
- 58 Jhang, K.-Y. Nonlinear ultrasonic techniques for nondestructive assessment of micro damage in material: A review. *Int. J. Precis. Eng. Manuf.* **10**, 123-135, doi:10.1007/s12541-009-0019-y (2009).
- 59 Matlack, K. H. *et al.* Evaluation of radiation damage using nonlinear ultrasound. *J. Appl. Phys.* **111**, -, doi:doi:<http://dx.doi.org/10.1063/1.3692086> (2012).
- 60 Li, F., Anzel, P., Yang, J., Kevrekidis, P. G. & Daraio, C. Granular acoustic switches and logic elements. *Nat Commun* **5**, doi:10.1038/ncomms6311 (2014).
- 61 Dauxois, T. & Peyrard, M. *Physics of Solitons*. (Cambridge University Press, 2006).
- 62 Campbell, D. K., Rosenau, P. & Zaslavsky, G. M. Introduction: The Fermi–Pasta–Ulam problem—The first fifty years. *Chaos: An Interdisciplinary Journal of Nonlinear Science* **15**, -, doi:doi:<http://dx.doi.org/10.1063/1.1889345> (2005).

- 63 Kevrekidis, P. G. Non-linear waves in lattices: past, present, future. *IMA J. Appl. Math.* **76**, 389-423, doi:10.1093/imamat/hxr015 (2011).
- 64 *Waves Called Solitons: Concepts and Experiments*. (Springer, 1999).
- 65 Zabusky, N. J. & Kruskal, M. D. Interaction of "Solitons" in a Collisionless Plasma and the Recurrence of Initial States. *Phys. Rev. Lett.* **15**, 240-243 (1965).
- 66 Theocharis, G. *et al.* Intrinsic energy localization through discrete gap breathers in one-dimensional diatomic granular crystals. *Physical Review E* **82**, doi:10.1103/PhysRevE.82.056604 (2010).
- 67 Flach, S. & Gorbach, A. V. Discrete breathers — Advances in theory and applications. *Physics Reports* **467**, 1-116, doi:<http://dx.doi.org/10.1016/j.physrep.2008.05.002> (2008).
- 68 Boechler, N. *et al.* Discrete Breathers in One-Dimensional Diatomic Granular Crystals. *Phys. Rev. Lett.* **104**, 244302 (2010).
- 69 Hoogeboom, C. *et al.* Hysteresis loops and multi-stability: From periodic orbits to chaotic dynamics (and back) in diatomic granular crystals. *EPL (Europhysics Letters)* **101**, 44003 (2013).
- 70 Theocharis, G. *et al.* Localized breathing modes in granular crystals with defects. *Physical Review E* **80**, 066601 (2009).
- 71 Lazaridi, A. N. & Nesterenko, V. F. Observation of a new type of solitary waves in a one-dimensional granular medium. *J Appl Mech Tech Phys* **26**, 405-408, doi:10.1007/BF00910379 (1985).
- 72 Nesterenko, V. F., Lazaridi, A. N. & Sibiryakov, E. B. The decay of soliton at the contact of two "acoustic vacuums". *J Appl Mech Tech Phys* **36**, 166-168, doi:10.1007/BF02369645 (1995).
- 73 Daraio, C., Nesterenko, V. F., Herbold, E. B. & Jin, S. Tunability of solitary wave properties in one-dimensional strongly nonlinear phononic crystals. *Physical Review E* **73**, 026610 (2006).
- 74 Daraio, C., Nesterenko, V. F., Herbold, E. B. & Jin, S. Energy Trapping and Shock Disintegration in a Composite Granular Medium. *Phys. Rev. Lett.* **96**, 058002 (2006).
- 75 Leonard, A., Fraternali, F. & Daraio, C. Directional Wave Propagation in a Highly Nonlinear Square Packing of Spheres. *Experimental Mechanics*, 1-11, doi:10.1007/s11340-011-9544-6.
- 76 Jayaprakash, K. R., Starosvetsky, Y., Vakakis, A., Peeters, M. & Kerschen, G. Nonlinear normal modes and band zones in granular chains with no pre-compression. *Nonlinear Dynamics* **63**, 359-385, doi:10.1007/s11071-010-9809-0 (2011).
- 77 Nesterenko, V. F., Daraio, C., Herbold, E. B. & Jin, S. Anomalous wave reflection at the interface of two strongly nonlinear granular media. *Phys. Rev. Lett.* **95**, doi:10.1103/PhysRevLett.95.158702 (2005).
- 78 Job, S., Melo, F., Sokolow, A. & Sen, S. How Hertzian Solitary Waves Interact with Boundaries in a 1D Granular Medium. *Phys. Rev. Lett.* **94**, 178002 (2005).
- 79 Job, S., Santibanez, F., Tapia, F. & Melo, F. Wave localization in strongly nonlinear Hertzian chains with mass defect. *Physical Review E* **80**, 025602 (2009).
- 80 Roundy, S. *et al.* Improving power output for vibration-based energy scavengers. *Pervasive Computing, IEEE* **4**, 28-36, doi:10.1109/MPRV.2005.14 (2005).
- 81 Roundy, S. On the Effectiveness of Vibration-based Energy Harvesting. *Journal of Intelligent Material Systems and Structures* **16**, 809-823, doi:10.1177/1045389x05054042 (2005).

- 82 Anton, S. R. & Sodano, H. A. A review of power harvesting using piezoelectric materials (2003-2006). *Smart Materials & Structures* **16**, R1-R21, doi:10.1088/0964-1726/16/3/r01 (2007).
- 83 Stephen, N. G. On energy harvesting from ambient vibration. *Journal of Sound and Vibration* **293**, 409-425, doi:<http://dx.doi.org/10.1016/j.jsv.2005.10.003> (2006).
- 84 Cottone, F., Vocca, H. & Gammaitoni, L. Nonlinear Energy Harvesting. *Phys. Rev. Lett.* **102**, doi:10.1103/PhysRevLett.102.080601 (2009).
- 85 Gammaitoni, L., Neri, I. & Vocca, H. Nonlinear oscillators for vibration energy harvesting. *Applied Physics Letters* **94**, -, doi:doi:<http://dx.doi.org/10.1063/1.3120279> (2009).
- 86 Erturk, A., Hoffmann, J. & Inman, D. J. A piezomagnetoelastic structure for broadband vibration energy harvesting. *Applied Physics Letters* **94**, -, doi:doi:<http://dx.doi.org/10.1063/1.3159815> (2009).
- 87 Khovanova, N. A. & Khovanov, I. A. The role of excitations statistic and nonlinearity in energy harvesting from random impulsive excitations. *Applied Physics Letters* **99**, -, doi:doi:<http://dx.doi.org/10.1063/1.3647556> (2011).
- 88 Litak, G., Friswell, M. I. & Adhikari, S. Magnetopiezoelectric energy harvesting driven by random excitations. *Applied Physics Letters* **96**, -, doi:doi:<http://dx.doi.org/10.1063/1.3436553> (2010).
- 89 Gammaitoni, L., Neri, I. & Vocca, H. The benefits of noise and nonlinearity: Extracting energy from random vibrations. *Chemical Physics* **375**, 435-438, doi:<http://dx.doi.org/10.1016/j.chemphys.2010.08.012> (2010).
- 90 Hajati, A. & Kim, S. G. Ultra-wide bandwidth piezoelectric energy harvesting. *Applied Physics Letters* **99**, doi:10.1063/1.3629551 (2011).
- 91 Davis, J. R. & Committee, A. I. H. *Metals Handbook*. (ASM International, 1998).
- 92 First Steps towards Piezoaction. *Piezomechanik* (2010).
- 93 Nesterenko, V. F. *Dynamics of heterogeneous materials*. (Springer, 2001).
- 94 Johnson, K. L. *Contact mechanics*. (Cambridge University Press, 1987).
- 95 Kittel, C. *Introduction to solid state physics*. (Wiley, 1996).
- 96 Jordan, D. & Smith, P. *Nonlinear Ordinary Differential Equations: Problems and Solutions: A Sourcebook for Scientists and Engineers: A Sourcebook for Scientists and Engineers*. (OUP Oxford, 2007).
- 97 Nayfeh, A. H. & Balachandran, B. *Applied Nonlinear Dynamics: Analytical, Computational and Experimental Methods*. (Wiley, 2008).
- 98 Simion, R. P. & Sen, S. Non-linear resonance-like processes in confined driven granular alignments and energy harvesting. *Proceedings of the Institution of Mechanical Engineers Part I-Journal of Systems and Control Engineering* **225**, 522-529, doi:10.1177/0959651811400940 (2011).
- 99 Preumont, A. *Mechatronics: Dynamics of Electromechanical and Piezoelectric Systems*. (Springer, 2006).
- 100 IEEE Standard on Piezoelectricity. *ANSI/IEEE Std 176-1987, 0_1*, doi:10.1109/IEEESTD.1988.79638 (1988).
- 101 Jae-Hwang, L., Jonathan, P. S. & Edwin, L. T. Micro-/Nanostructured Mechanical Metamaterials. *Advanced Materials* **24**, 4782-4810, doi:10.1002/adma.201201644 (2012).

- 102 Maldovan, M. & Thomas, E. L. Simultaneous localization of photons and phonons in two-dimensional periodic structures. *Applied Physics Letters* **88**, -, doi:doi:<http://dx.doi.org/10.1063/1.2216885> (2006).
- 103 Noda, S., Chutinan, A. & Imada, M. Trapping and emission of photons by a single defect in a photonic bandgap structure. *Nature* **407**, 608-610 (2000).
- 104 Schneider, D. *et al.* Defect-Controlled Hypersound Propagation in Hybrid Superlattices. *Phys. Rev. Lett.* **111**, 164301 (2013).
- 105 Soljačić, M. & Joannopoulos, J. D. Enhancement of nonlinear effects using photonic crystals. *Nat Mater* **3**, 211-219 (2004).
- 106 Zhang, S., Yin, L. & Fang, N. Focusing Ultrasound with an Acoustic Metamaterial Network. *Physical Review Letters* **102**, 194301 (2009).
- 107 Pendry, J. B., Schurig, D. & Smith, D. R. Controlling Electromagnetic Fields. *Science* **312**, 1780-1782, doi:10.1126/science.1125907 (2006).
- 108 Zhang, S., Xia, C. & Fang, N. Broadband Acoustic Cloak for Ultrasound Waves. *Physical Review Letters* **106**, 024301 (2011).
- 109 Jaglinski, T., Kochmann, D., Stone, D. & Lakes, R. S. Composite Materials with Viscoelastic Stiffness Greater Than Diamond. *Science* **315**, 620-622, doi:10.1126/science.1135837 (2007).
- 110 Majidi, C. & Wood, R. J. Tunable elastic stiffness with microconfined magnetorheological domains at low magnetic field. *Applied Physics Letters* **97**, -, doi:doi:<http://dx.doi.org/10.1063/1.3503969> (2010).
- 111 Nicolaou, Z. G. & Motter, A. E. Mechanical metamaterials with negative compressibility transitions. *Nat Mater* **11**, 608-613, doi:<http://www.nature.com/nmat/journal/v11/n7/abs/nmat3331.html#supplementary-information> (2012).
- 112 Dong, L., Stone, D. S. & Lakes, R. S. Broadband viscoelastic spectroscopy measurement of mechanical loss and modulus of polycrystalline BaTiO₃ vs. temperature and frequency. *physica status solidi (b)* **245**, 2422-2432, doi:10.1002/pssb.200880270 (2008).
- 113 Lakes, R. S., Lee, T., Bersie, A. & Wang, Y. C. Extreme damping in composite materials with negative-stiffness inclusions. *Nature* **410**, 565-567 (2001).
- 114 Lapine, M., Shadrivov, I. V., Powell, D. A. & Kivshar, Y. S. Magnetoelastic metamaterials. *Nat Mater* **11**, 30-33 (2012).
- 115 Jaglinski, T. M. & Lakes, R. S. in *Adaptive Structures* 231-246 (John Wiley & Sons, Ltd, 2007).
- 116 Wojnar, C. S. & Kochmann, D. M. A negative-stiffness phase in elastic composites can produce stable extreme effective dynamic but not static stiffness. *Philosophical Magazine* **94**, 532-555, doi:10.1080/14786435.2013.857795 (2013).
- 117 Montroll, E. W. & Potts, R. B. Effect of Defects on Lattice Vibrations. *Physical Review* **100**, 525-543 (1955).
- 118 Boechler, N., Theocharis, G. & Daraio, C. Bifurcation-based acoustic switching and rectification. *Nat Mater* **10**, 665-668, doi:<http://www.nature.com/nmat/journal/v10/n9/abs/nmat3072.html#supplementary-information> (2011).

- 119 Martin, P., Mehta, A. D. & Hudspeth, A. J. Negative hair-bundle stiffness betrays a mechanism for mechanical amplification by the hair cell. *Proceedings of the National Academy of Sciences* **97**, 12026-12031, doi:[10.1073/pnas.210389497](https://doi.org/10.1073/pnas.210389497) (2000).
- 120 Karabalin, R. B. *et al.* Signal Amplification by Sensitive Control of Bifurcation Topology. *Physical Review Letters* **106**, 094102 (2011).
- 121 Ibrahim, R. A. Recent advances in nonlinear passive vibration isolators. *Journal of Sound and Vibration* **314**, 371-452, doi:<http://dx.doi.org/10.1016/j.jsv.2008.01.014> (2008).
- 122 Deymier, P. A. *Acoustic Metamaterials and Phononic Crystals*. (Springer, 2013).
- 123 Craster, R. V. & Guenneau, S. *Acoustic Metamaterials: Negative Refraction, Imaging, Lensing and Cloaking*. (Springer, 2012).
- 124 Karman, T. *Engineer Grapples with Nonlinear Problems*. (1944).
- 125 Powers, P. E. *Fundamentals of Nonlinear Optics*. (Taylor & Francis, 2011).
- 126 Liang, B., Guo, X. S., Tu, J., Zhang, D. & Cheng, J. C. An acoustic rectifier. *Nat Mater* **9**, 989-992, doi:<http://www.nature.com/nmat/journal/v9/n12/abs/nmat2881.html#supplementary-information> (2010).
- 127 Guyer, R. A. & Johnson, P. A. *Nonlinear Mesoscopic Elasticity: The Complex Behaviour of Rocks, Soil, Concrete*. (Wiley, 2009).
- 128 Khomeriki, R., Lepri, S. & Ruffo, S. Nonlinear supratransmission and bistability in the Fermi-Pasta-Ulam model. *Physical Review E* **70**, 066626 (2004).
- 129 Togueu Motcheyo, A. B., Tchawoua, C. & Tchingang Tchameu, J. D. Supratransmission induced by waves collisions in a discrete electrical lattice. *Physical Review E* **88**, 040901 (2013).
- 130 Theocharis, G., Boechler, N. & Daraio, C. *Acoustic Metamaterials and Phononic Crystals*. 217-251 (Springer, 2013).
- 131 Cabaret, J., Tournat, V. & Béquin, P. Amplitude-dependent phononic processes in a diatomic granular chain in the weakly nonlinear regime. *Physical Review E* **86**, 041305 (2012).
- 132 Jayaprakash, K., Starosvetsky, Y., Vakakis, A., Peeters, M. & Kerschen, G. Nonlinear normal modes and band zones in granular chains with no pre-compression. *Nonlinear Dynamics* **63**, 359-385, doi:[10.1007/s11071-010-9809-0](https://doi.org/10.1007/s11071-010-9809-0) (2011).
- 133 Tournat, V., Inserra, C. & Gusev, V. Non-cascade frequency-mixing processes for elastic waves in unconsolidated granular materials. *Ultrasonics* **48**, 492-497, doi:<http://dx.doi.org/10.1016/j.ultras.2008.03.014> (2008).
- 134 Holmes, P. J. The dynamics of repeated impacts with a sinusoidally vibrating table. *Journal of Sound and Vibration* **84**, 173-189, doi:[http://dx.doi.org/10.1016/S0022-460X\(82\)80002-3](http://dx.doi.org/10.1016/S0022-460X(82)80002-3) (1982).
- 135 Harne, R. L. & Wang, K. W. A review of the recent research on vibration energy harvesting via bistable systems. *Smart Materials and Structures* **22**, 023001 (2013).
- 136 Lee, E. W. Non-linear forced vibration of a stretched string. *British Journal of Applied Physics* **8**, 411 (1957).
- 137 Postma, H. W. C., Kozinsky, I., Husain, A. & Roukes, M. L. Dynamic range of nanotube- and nanowire-based electromechanical systems. *Applied Physics Letters* **86**, -, doi:<http://dx.doi.org/10.1063/1.1929098> (2005).
- 138 Erturk, A. & Inman, D. J. *Piezoelectric Energy Harvesting*. (Wiley, 2011).

- 139 Billah, K. Y. & Scanlan, R. H. Resonance, Tacoma Narrows bridge failure, and undergraduate physics textbooks. *American Journal of Physics* **59**, 118-124, doi:doi:<http://dx.doi.org/10.1119/1.16590> (1991).
- 140 Morse, P. M. *Thermal Physics*. (W.A. Benjamin, 1969).
- 141 Wang, F., Sigmund, O. & Jensen, J. S. Design of materials with prescribed nonlinear properties. *Journal of the Mechanics and Physics of Solids* **69**, 156-174, doi:<http://dx.doi.org/10.1016/j.jmps.2014.05.003> (2014).
- 142 Vaezi, M., Seitz, H. & Yang, S. A review on 3D micro-additive manufacturing technologies. *Int J Adv Manuf Technol* **67**, 1721-1754, doi:10.1007/s00170-012-4605-2 (2013).

APPENDIX

1.1 Analytic modeling for extraordinary stiffness tunability

This section follows chapter 6 and provides an analytic derivation to explain the tunable stiffness phenomena. The analytics were done primarily by Marc Serra-Garcia and demonstrate the broader applicability of this concept to other 1-D lattices.

The system considered in chapter 6 consists of a chain of particles coupled through an anharmonic interaction potential (Fig A.1a). In order to get exact results, the motion of all particles needs to be accounted for. However, studying the dynamics of a large number of particles analytically is a difficult problem. In our system we can avoid this complexity by realizing that most of the motion is concentrated around the defect. This is a consequence of the defect mode being highly localized. This localization allows us to capture all of the essential dynamics of the system by considering a single oscillating particle and assuming that other particles in the lattice displace only quasi-statically (Fig A.1c,d). By using this simplification, we can qualitatively reproduce all of the effects that we have observed experimentally, such as the tuned force-displacement relationship of the lattice. In order to accomplish this, we consider the system at a prescribed total displacement, and then proceed to calculate the amplitude of vibration of the defect, as well as the static force at the boundary.

At each fixed compression value, we model the defect as a point mass M , with a dynamic displacement from equilibrium, u_d . The defect is subject to a linear damping $F_d = -b\dot{u}_d$ and a periodic excitation force $F(t) = F_e \cos(\omega t)$. As per our model approximation, we

consider the neighboring particles to have a constant displacement from equilibrium denoted by Δ . We also assume that the defect motion happens only at the excitation frequency, and is given by $u_d = A \cos(\omega t + \varphi)$. We replace the particles between the defect neighbors and the walls by a linear spring with a force relation $F(\Delta) = F_0 + K_C \Delta$, where F_0 is the static force at equilibrium and K_C is calculated by linearizing the interaction force of all the particles after the defect's neighbors and lumping them into a single spring.

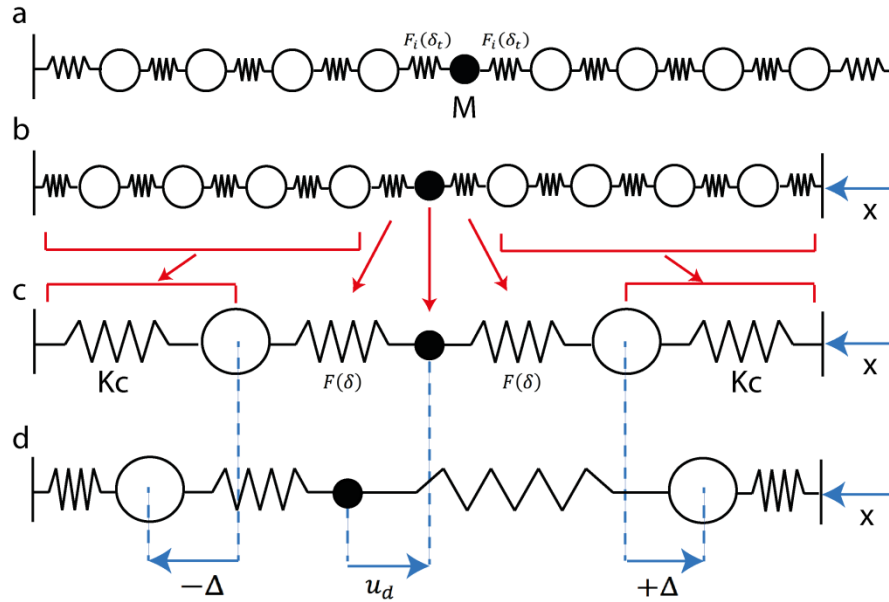


Figure A.1: Analytical modeling of the system. **a** Initial lattice with no deformation. The lattice consists of a chain of particles, where the central particle is a defect having a mass M smaller than the rest of the particles. The defect interacts with the neighbors through a nonlinear force $F_i(\delta_t)$, where δ_t is the total distance separating the defect and the neighbors. **b** Deformed lattice. The lattice boundary has been displaced by an amount x . **c** Simplified system used in the analytical approximation. For each fixed displacement value x , the interaction potential between the defect and the neighbors is approximated by a third order polynomial $F(\delta)$, where $\delta = \delta_t - \delta_0$, δ_0 being the equilibrium distance between the defect and the neighbors in the deformed lattice with no defect drive. All the other beads in the chain are approximated by two linear springs K_C , with K_C calculated independently for each deformation value x . **d** Simplified system with the defect in motion. The defect is displaced from equilibrium by an amount u_d . The two neighboring beads are

statically pushed away from it by an amount Δ due to thermal expansion.

We further simplify the system by performing a Taylor expansion of the nonlinear spring connecting the defect mode with the two half-lattices on each side. We take the Taylor expansion up to third degree, $F(\delta) = F_0 + k\delta + k'\delta^2 + k''\delta^3$. Here, $F_i(\delta_t)$ is approximated by the $F(\delta)$. A force including terms up to third degree is able to capture static equilibrium, linear oscillation, thermal expansion, and resonance bending effects. The expansion is calculated around the inter-particle distance at rest, denoted by δ_0 . At each deformation value, we calculate the coefficients in the Taylor expansion for the defect-neighbor interaction and the linearized spring constant for the half-lattices.

This model results in an equation of motion for the single defect particle and an equation for the static equilibrium of the defect's neighbors. Note that, due to the symmetry of the system, we only need a single equilibrium equation for the two neighbors.

$$M\ddot{u}_d + b\dot{u}_d - F(-u_d - \Delta) + F(u_d - \Delta) = F_e \cos \omega t \quad (\text{A.1})$$

$$K_C \Delta + F_0 = F(u_d - \Delta) \quad (\text{A.2})$$

To solve for the amplitude and static force, we perform a harmonic balance⁸⁸ including only components at the excitation frequency, and discarding terms containing powers of A^2 above 3. We neglect higher frequency components because they are significantly lower in the frequency spectrum of the defect's vibration. For the neighbor's equation, we neglect all the harmonic terms and take only the zero-frequency component force. This procedure results in the following condition for the amplitude of the defect:

$$A^2 \left[\left(2k + \frac{3}{4} \left[2k'' - \frac{8}{3} \left(\frac{k'^2}{K_c + k} \right) \right] A^2 - M \omega^2 \right)^2 + (b\omega)^2 \right] - F_e^2 = 0 \quad (\text{A.3})$$

The harmonic balance condition allows us to determine the vibration amplitude of the defect, since all other variables are known: the parameters k , k' , k'' and K_c depend on the total deformation of the lattice, which is prescribed. F_e and ω describe the defect excitation and are also prescribed. The defect's mass M and damping b are fixed parameters of the system.

We can get further insight on the properties of this system by realizing that the amplitude condition (Eq. A.3) is identical to the one that is obtained by performing the same harmonic balance procedure on a Duffing oscillator. A Duffing oscillator is a single degree of freedom dynamical system described by the equation $\ddot{x} + \frac{1}{\tau} \dot{x} + \omega_0^2 x + \alpha x^3 = F_d/M$, and is an extremely well studied system. In order to transform our system into a Duffing oscillator, we use the equations:

$$\omega_0^2 = \frac{2k}{M} \quad (\text{A.4})$$

$$\alpha = \frac{1}{M} \left(2k'' - \frac{8}{3} \frac{k'^2}{K_c} \right). \quad (\text{A.5})$$

Knowing the vibration amplitude of the defect, it is possible to determine the thermal expansion, and therefore the force at the boundary. To do so we use the defect neighbor's equilibrium equation, and the fact that the force on the linearized spring, K_c , that connects the defect's neighbors to the boundary is the same on both ends of the spring.

$$F_b = F_0 + \frac{1}{2} \left(\frac{k'}{1 + \frac{k}{k_c}} \right) A^2 \quad (\text{A.6})$$

As expected, the force at the boundary is the sum of the force without any defect drive, and a thermal expansion term that increases with increasing defect motion. The thermal expansion is a consequence of the asymmetric terms in the interaction potential. During a period of the defect oscillation around an equilibrium point, symmetric terms result in an equal amount of attractive and repulsive force. In contrast, asymmetric terms introduce different amounts of attractive and repulsive force, and therefore produce a net effect in the force at the boundary.

Since the analytical model allows us to predict the static force at each displacement value, we can differentiate this prediction with respect to the displacement in order to obtain the stiffness (Eq. A.7). This equation contains the original stiffness of the lattice, a term relating changes in force at the boundary to changes in the vibration amplitude of the defect, and a term due to the change in the thermal expansion coefficient as the lattice is compressed.

$$k = \frac{dF_b}{dx} = \frac{dF_0}{dx} + \left(\frac{k'}{1 + \frac{k}{k_c}} \right) A \frac{dA}{dx} + \frac{1}{2} A^2 \frac{d}{dx} \left(\frac{k'}{1 + \frac{k}{k_c}} \right) \quad (\text{A.7})$$

The term dA/dx can be found implicitly from the harmonic balance. This is done by thinking of the balance condition (Eq. A.3) as a function of the amplitude and displacement, and noting that the amplitude itself depends on the displacement:

$$\psi(A(x), x) = A^2 \left[\left(2k(x) + \frac{3}{4} \left[2k''(d) - \frac{8}{3} \left(\frac{k'(x)^2}{K_c(x) + k(x)} \right) \right] A^2 - M \omega^2 \right)^2 + (b\omega)^2 \right] - F_e^2. \quad (\text{A.8})$$

Since this function must stay constant at zero for all displacements, its total derivative with respect to the displacement must also be zero:

$$\frac{d\psi}{dx} = \frac{\partial\psi}{\partial A} \frac{dA}{dx} + \frac{\partial\psi}{\partial x} = 0. \quad (\text{A.9})$$

From the previous equation, it is possible to obtain a closed expression for dA/dx , provided that the amplitude of oscillation is known:

$$\frac{dA}{dx} = - \frac{\left(\frac{\partial\psi}{\partial x} \right)_A}{\left(\frac{\partial\psi}{\partial A} \right)_x}. \quad (\text{A.10})$$

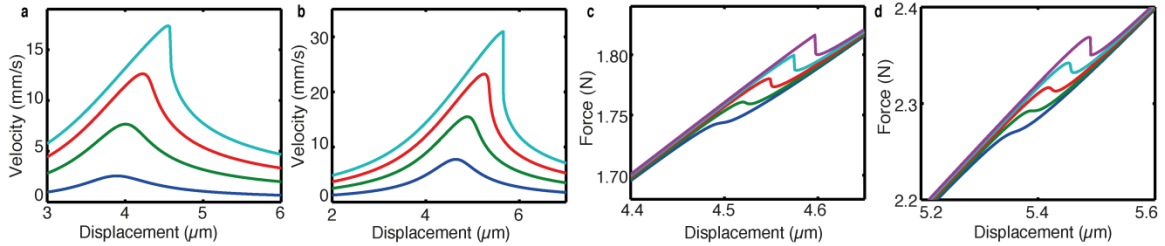


Figure A.2: Analytical predictions and comparison to numerical results. **a** Defect response obtained by numerically integrating the equations of motion for the full system. **b** Defect response predicted by the analytical model **c** Force- displacement relation of the material obtained through numerical integration **d** Force- displacement relation obtained analytically. All panels are calculated for an excitation frequency of 10.5 KHz at increasing excitation amplitudes.

We have created a simplified model that captures the tuning of the incremental stiffness through the excitation of local defect modes. We use the model to engineer the nonlinear interaction potential so it allows us to tune the stiffness to arbitrarily positive values. This is accomplished by looking at the stiffness equation (Eq. A.7). When the changes in the stiffness are very large, the term $k'A \partial A / \partial x$ is always dominant. This is because $\partial A / \partial x$ can grow arbitrarily large, while the other terms in the equation are bounded. The term's contribution to the stiffness of the chain, K , is given by:

$$\Delta K = - \frac{A}{1 + \frac{k}{K_c}} \frac{k' \left(\frac{\partial \psi}{\partial x} \right)_A}{\left(\frac{\partial \psi}{\partial A} \right)_x}. \quad (\text{A.11})$$

This contribution is large when the system approaches a bifurcation. When that happens, $\partial \psi / \partial x$ tends to zero. Depending on the sign of the numerator $-k'(\partial \psi / \partial x)$, the stiffness will grow arbitrarily positive or arbitrarily negative. We study this value for a power law potential, $F = Ax^p$ (Fig. A.3a). When the exponent p is between 0 and 1, the numerator is positive. In lattices with this kind of interaction force law, the stiffness can be tuned to arbitrarily positive values (Figs. A.3b and A.3c). Recently proposed theoretical work^{S141} combined with novel microfabrication techniques^{S142} should enable the design of mechanical lattices with tailored interaction potentials. Therefore, it should be possible to create materials with stiffness that can be tuned over a broad range to positive or negative values.

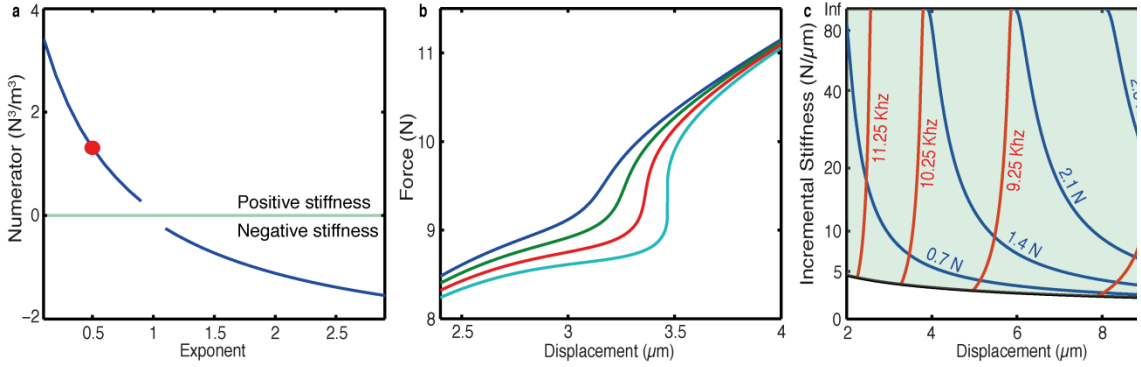


Figure A.3: Stiffness tuning to positive infinity. **a** Stiffness numerator corresponding to a power law potential $F = \frac{1}{p} \delta_t^p$ as a function of the exponent. Calculated for a chain of 9 particles with $\delta_T = 1$. Parameters are $M = 1$ and $b = 0.025$. **b** Force-displacement curves for a 9-particle lattice with a power law interaction force exponent $F = Ap^{0.5}$, $A = 5600$. The exponent 0.5 is indicated as a red dot in **a**. The curves correspond to an excitation frequency of 10.5 KHz and increasing excitation forces. **c** Map relating the applied excitation frequency and amplitude to the stiffness, for the same system as **b**. In all panels the interaction force law is assumed to be equal between all neighboring particles. For **b** and **c**, the defect's mass and damping are the same as in Fig A.2.

1.2 Analysis for strongly nonlinear frequency bands

This section follows the experimental results from chapter 8. The analysis examines the extension from a system of two beads to frequency bands in the infinite limit. This analysis was done principally by K.R. Jayaprakash.

In this section, we analytically study the weakly nonlinear dynamics in the AB (attenuation band). The induced permanent compression leads to a linearizable system suitable for analytical techniques. We extend the previous results by considering a homogeneous crystal of N beads. Similar to the setup explained in section 3.34 for two beads, the first bead is harmonically driven and the N -th bead is constrained by a fixed wall. All the beads interact with their nearest neighbors through Hertzian interaction law. We incorporate linear viscous damping (coefficient λ) between interacting beads to simulate dissipative effects in the

experimental system and to suppress transient dynamics. Here, we account for the damping force only when the beads are in contact and thus incorporate the Heaviside function (Θ) on the relative displacement of the beads. In our analytical approach we non-dimensionalize the equations of motion so that the results are of general applicability. We therefore begin with presenting the equations of motion of the theoretical model of an N bead chain with right end fixed and the left end harmonically excited:

$$\begin{aligned}
m_1 \frac{d^2 u_1}{dt^2} &= (4/3)E_{1*} \sqrt{R} (F(t) - u_1)_+^{3/2} - (4/3)E_* \sqrt{\frac{R}{2}} (u_1 - u_2)_+^{3/2} + \\
&\quad \lambda (\dot{f}(t) - \dot{u}_1) \Theta [f(t) - u_1] - \lambda (\dot{u}_1 - \dot{u}_2) \Theta [u_1 - u_2] \\
&\quad \dots \\
m_i \frac{d^2 u_i}{dt^2} &= (4/3)E_* \sqrt{\frac{R}{2}} \left\{ (u_{i-1} - u_i)_+^{3/2} - (u_i - u_{i+1})_+^{3/2} \right\} + \\
&\quad \lambda (\dot{u}_{i-1} - \dot{u}_i) \Theta [u_{i-1} - u_i] - \lambda (\dot{u}_i - \dot{u}_{i+1}) \Theta [u_i - u_{i+1}] \\
&\quad \dots \\
m_N \frac{d^2 u_N}{dt^2} &= (4/3)E_* \sqrt{\frac{R}{2}} (u_{N-1} - u_N)_+^{3/2} - (4/3)E_{2*} \sqrt{R} (u_N)_+^{3/2} + \\
&\quad \lambda (\dot{u}_{N-1} - \dot{u}_N) \Theta [u_{N-1} - u_N] - \lambda (\dot{u}_N) \Theta [u_N],
\end{aligned} \tag{A.12}$$

where $i = 2, 3, \dots, (N-1)$ are the bead subscripts and $F(t) = A \sin(\omega t)$ is the harmonic base excitation. The appropriate non-dimensionalization leads to the set of normalized equations of motion,

$$\begin{aligned}
\frac{d^2 X_1}{d\tau^2} &= \eta [\sin(\beta\tau) - X_1]_+^{3/2} - \frac{1}{\sqrt{2}} (X_1 - X_2)_+^{3/2} + \\
&\xi (\beta \cos(\beta\tau) - X'_1) \Theta [\sin(\beta\tau) - X_1] - \xi (X'_1 - X'_2) \Theta [X_1 - X_2] \\
&\quad \dots \\
\frac{d^2 X_i}{d\tau^2} &= \frac{1}{\sqrt{2}} \{ (X_{i-1} - X_i)_+^{3/2} - (X_i - X_{i+1})_+^{3/2} \} + \\
&\xi (X'_{i-1} - X'_i) \Theta [X_{i-1} - X_i] - \xi (X'_i - X'_{i+1}) \Theta [X_i - X_{i+1}] \\
&\quad \dots \\
\frac{d^2 X_N}{d\tau^2} &= \frac{1}{\sqrt{2}} (X_{N-1} - X_N)_+^{3/2} - \alpha (X_N)_+^{3/2} + \\
&\xi (X'_{N-1} - X'_N) \Theta [X_{N-1} - X_N] - \xi (X'_N) \Theta [X_N],
\end{aligned} \tag{A.13}$$

where E_* is the effective stiffness between the interacting beads, and $X_i = u_i / A$, $\tau = (4E_* \sqrt{AR} / 3m)^{1/2} t \equiv \psi t$, $\eta = E_{1*} / E_*$, $\alpha = E_{2*} / E_*$, $\beta = \omega / \psi$, and $\xi = \lambda / m\psi$ are non-dimensional variables relating (3) and (4). Without loss of generality, we consider $\eta = 1$ and $\alpha = 1$ denoting that the dynamic sensor, actuator, and beads are made of the same material. This does not affect the validity of the resulting dynamics. Recalling the material and experimental data from section 3.3.4, we obtain $E_* = E_S / [2(1 - \nu_S^2)]$, $A = 3.5 \times 10^{-7} m$, and $\omega = 8500 \text{ Hz}$; moreover, the non-dimensional quantities are computed as $\beta = 3.1742$, $\psi = 1.6825 \times 10^4$, and $\xi = 0.5$.

As a second step, and in view of the fact that a sustained compression is experienced by the beads in the AB, we decompose the bead displacements into ‘static’ (permanent constant compression) and ‘dynamic’ (oscillatory) components. For high frequency excitations in the AB, experiment and simulation indicate that small amplitude oscillations about a permanent compressed state occur, and this decomposition is in line with this observation. This motivates

us to introduce new translated coordinates $X_j(\tau) = \delta_j + x_j(\tau)$, where the j -th bead's displacement is expressed as a combination of its static, $\delta_j > 0$, and dynamic, $x_j(t)$, components. In simulations we observed that $\delta_j > \delta_{j+1}$, i.e., that the permanent compression experienced by each bead decreases as we move away from the actuator and the standing wave oscillation in the AB becomes spatially localized (Fig. A.4). The axes in Fig. A4-A8 denote the non-dimensional units derived above. From the previously shown results it can be deduced that no separation occurs between beads once the dynamics enters the AB, i.e., the dynamics is smooth between interacting beads. Therefore the subscript '+' can be eliminated from the equations of motion (Eq. A.13), which greatly facilitates the asymptotic analysis. The only exception is the contact between the actuator and first bead.

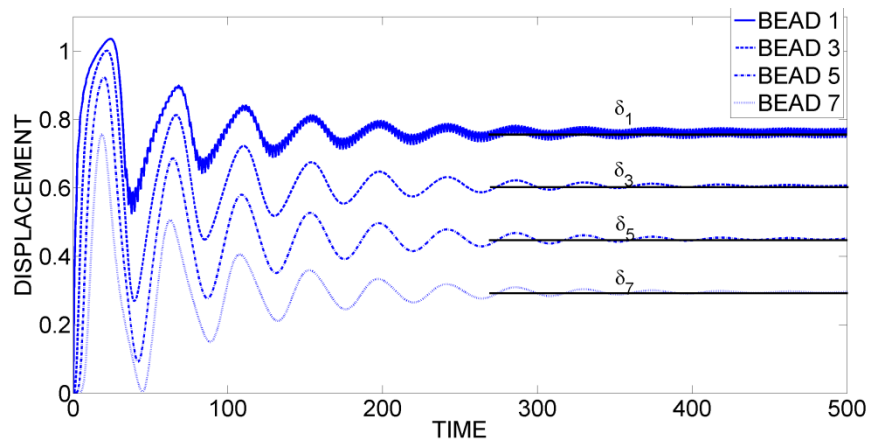


Figure. A.4: The displacement response of 1st, 3rd, 5th, and 7th beads of a 10 bead homogeneous chain under harmonic excitation with frequency in the attenuation zone. All units are non-dimensional.

When the dynamics is well inside the AB it holds that $|\sin(\beta\tau) - \delta_1| \gg x_1(\tau)$, except in the close neighborhood of points 'a' and 'b' as shown in Fig. A.5a. Thus, it can be assumed that $[\sin(\beta\tau) - \delta_1 - x_1] > 0$ in the region between points 'a' and 'b' where the actuator displacement exceeds the permanent compression of the first bead δ_1 , and $[\sin(\beta\tau) - \delta_1 - x_1] < 0$ when the actuator displacement is less than δ_1 .

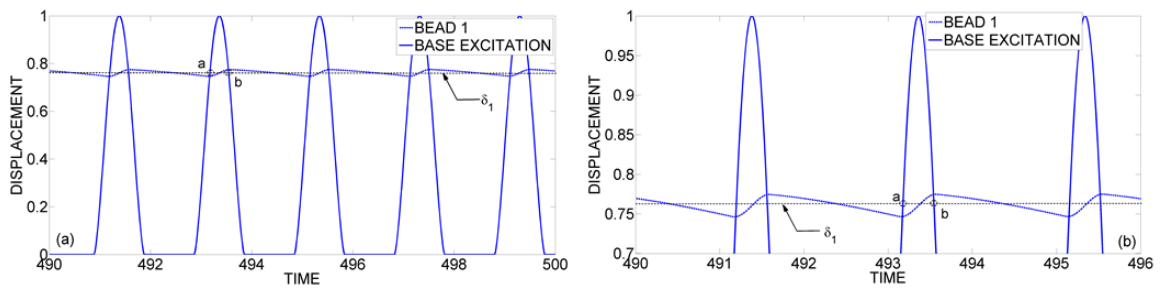


Figure A.5: The displacement response of the 10-bead homogeneous chain under harmonic excitation with frequency in the attenuation zone: (a) Response of the first bead superimposed to the excitation, and (b) detail of (a). All units are non-dimensional.

Figure A.5b shows a detailed view of the region between points 'a' and 'b'. It follows that we can modify (4) by decomposing the responses in terms of static and dynamic components and incorporating the observations mentioned above. This leads to the following modified equations:

$$\begin{aligned} \frac{d^2 x_1}{d\tau^2} = & \eta [\sin(\beta\tau) - \delta_1]_+^{3/2} - \frac{3}{2} \eta [\sin(\beta\tau) - \delta_1]_+^{1/2} x_1 - \\ & \frac{1}{\sqrt{2}} (\delta_1 - \delta_2)^{3/2} - \frac{3}{2\sqrt{2}} (\delta_1 - \delta_2)^{1/2} (x_1 - x_2) + \\ & \xi(\beta \cos(\beta\tau) - x'_1) H[\sin(\beta\tau) - \delta_1] - \xi(x'_1 - x'_2) + O(x_1^p x_2^q) \\ & \dots \end{aligned}$$

$$\begin{aligned} \frac{d^2 x_i}{d\tau^2} = & \frac{1}{\sqrt{2}} \left\{ (\delta_{i-1} - \delta_i)^{3/2} + \frac{3}{2} (\delta_{i-1} - \delta_i)^{1/2} (x_{i-1} - x_i) - (\delta_i - \delta_{i+1})^{3/2} - \frac{3}{2} (\delta_i - \delta_{i+1})^{1/2} (x_i - x_{i+1}) \right\}_+ \\ & \xi(x'_{i-1} - 2x'_i + x'_{i+1}) + O(x_{i-1}^p x_i^q) + O(x_i^r x_{i+1}^s) \\ & \dots \\ \frac{d^2 x_N}{d\tau^2} = & \frac{1}{\sqrt{2}} (\delta_{N-1} - \delta_N)^{3/2} + \frac{3}{2\sqrt{2}} (\delta_{N-1} - \delta_N)^{1/2} (x_{N-1} - x_N) - \alpha (\delta_N)^{3/2} - \frac{3}{2} \alpha (\delta_N)^{1/2} x_N \\ & + \xi(x'_{N-1} - 2x'_N) + O(x_{N-1}^p x_N^q) + O(x_N^z) \\ & i = 2, 3, \dots, (N-1), \quad p+q \geq 2, \quad r+s \geq 2, \quad z \geq 2. \end{aligned}$$

As in the previous discussion, the only non-smooth component is in the first equation of (Eq. A.14), modeling the separation of the actuator and first bead.

We observe that there are two terms on the right hand side of (Eq. A.14) resulting from the interaction between beads; namely static components dependent only on δ_j , and dynamic components involving $x_j(\tau)$. We account for the non-smooth terms in (Eq. A.14) by expanding the harmonic excitation term $\left([\sin(\beta\tau) - \delta_1]_+^{3/2}\right)$ in Fourier series to obtain ‘static’ and ‘dynamic’ components as follows:

$$[\sin(\beta\tau) - \delta_1]_+^{3/2} = a_0 + \sum_{n=1}^{\infty} a_n \cos(n\beta\tau) + \sum_{n=1}^{\infty} b_n \sin(n\beta\tau) \quad (\text{A.15})$$

with the coefficients defined as:

$$\begin{aligned} a_0 &= \frac{\beta}{2\pi} \int_{-\pi/\beta}^{\pi/\beta} [\sin(\beta\tau) - \delta_1]_+^{3/2} d\tau \\ a_n &= \frac{\beta}{\pi} \int_{-\pi/\beta}^{\pi/\beta} [\sin(\beta\tau) - \delta_1]_+^{3/2} \cos(n\beta\tau) d\tau \\ b_n &= \frac{\beta}{\pi} \int_{-\pi/\beta}^{\pi/\beta} [\sin(\beta\tau) - \delta_1]_+^{3/2} \sin(n\beta\tau) d\tau. \end{aligned} \quad (\text{A.16})$$

Now, by balancing the static components in all (smooth) equations (Eq. A.14), we obtain the following recursive relation that can be used for computing the permanent compression between beads:

$$\begin{aligned} (\delta_{j-1} - \delta_j)^{3/2} - (\delta_j - \delta_{j+1})^{3/2} &= 0 \\ \dots & \\ \frac{1}{\sqrt{2}}(\delta_{N-1} - \delta_N)^{3/2} - \alpha(\delta_N)^{3/2} &= 0. \end{aligned} \quad (\text{A.17})$$

where $j = 2, 3, \dots, (N-1)$. A trivial algebraic manipulation yields,

$$\delta_{j-1} = 2\delta_j - \delta_{j+1} \quad (\text{A.18})$$

$$\begin{aligned} \dots & \\ \delta_{N-1} &= \delta_N(1 + \gamma) \end{aligned} \quad (\text{A.19})$$

$$\delta_i = \frac{\delta_{i-1} [1 + (N-i)\gamma]}{[1 + (N-i+1)\gamma]}, \quad 1 < i \leq N,$$

where $\gamma = 2^{1/3} \alpha^{2/3}$. The only unknown in the above set of equations is the permanent compression of the first bead, δ_1 . Once this is evaluated the compression of all the other beads can be expressed in terms of δ_1 . The compression δ_1 can be obtained by balancing the static force components in the first equation of (Eq. A.14), i.e., balancing the constant term from the Fourier series (Eq. A.15) with the constant force interaction between the first and the second beads. Then, we obtain an implicit relation of the form,

$$\frac{\eta\beta}{2\pi} \int_{-\pi/\beta}^{\pi/\beta} [\sin(\beta\tau) - \delta_1]_+^{3/2} d\tau - \frac{1}{\sqrt{2}} (\delta_1 - \delta_2)^{3/2} = 0. \quad (\text{A.20})$$

Substituting for δ_2 in terms of δ_1 and rescaling time $\tilde{\tau} = \beta\tau$, we derive the final form for the equation governing the permanent compression of the first bead,

$$\left\{ \frac{\eta}{\pi} \int_{\sin^{-1}(\delta_1)}^{\pi/2} (\sin(\tilde{\tau}) - \delta_1)^{3/2} d\tilde{\tau} \right\}^{2/3} = \delta_1 \left[\frac{1}{1 + (N-1)\gamma} \right], \quad (\text{A.21})$$

where the '+' sign is removed from (Eq. A.19) since $(\sin(\tilde{\tau}) - \delta_1)^{3/2} \geq 0$ within the limits of integration.

The above equation is evaluated numerically to obtain δ_1 . This analysis predicts that the static compression δ_1 of the first bead (and therefore of any other bead) is independent of the

excitation frequency when the dynamics is well inside the AB (i.e., for relatively high frequencies). This is verified through numerical simulations (Fig. A.6), where we depict the response of the first bead for a homogeneous chain with $N=10$ at various excitation frequencies β inside the AB. The static component of the response is independent of the excitation frequency. This analysis assumes weakly nonlinear behavior, and these predictions are not valid at lower frequencies as the dynamics makes the transition from the PB (propagation band) to the AB (attenuation band).

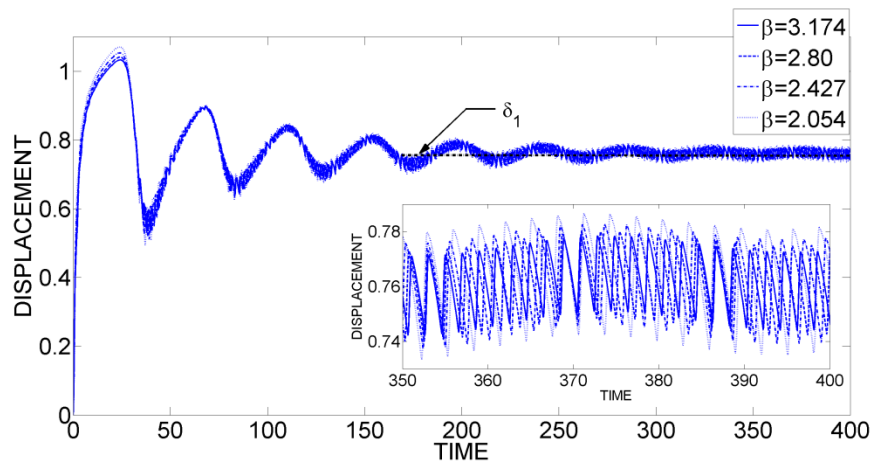


Figure A.6 (Color online) the displacement response of first bead of a 10-bead homogeneous chain with varying normalized excitation frequency and fixed normalized excitation amplitude equaling unity (dynamics deep inside the attenuation zone). All units are non-dimensional.

The static overlap of each bead in the granular chain is evaluated using (Eq. A.18, A.19, and A.20) and is compared to the results derived from numerical simulation for a 20 bead crystal, $N=20$ (Fig. A.7). The numerical simulations show good correspondence with the analytical estimates and confirm that the spatial variation of the static overlap is nearly linear. As the length of the crystal is increased the static component of the first bead's displacement reaches

unity asymptotically, whereas the static offset of the last bead approaches zero. Hence, the resulting standing wave oscillations executed by the beads become spatially localized well inside the AB of the harmonically forced system. In essence, for a sufficiently large number of beads, the chain detaches from the exciter and the energy input to the chain approaches zero asymptotically.

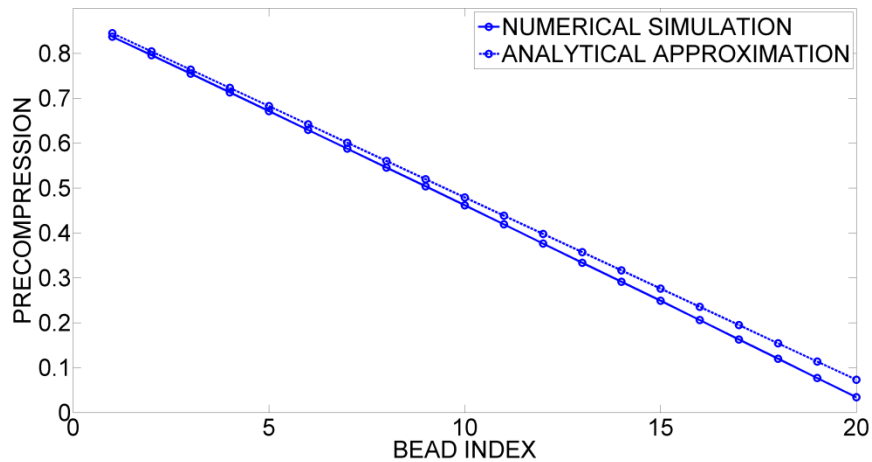


Figure A.7: Spatial variation of permanent precompression (δ_i) in a 20 bead chain when the dynamics is deep in the attenuation zone. All units are non-dimensional.

Finally, we obtain analytic estimates of the individual oscillatory responses of the beads by considering the dynamic components of the bead displacements in (Eq. A.14). We arrive at reduced dynamic equations for each $x_j(\tau)$ by removing the static components of (Eq. A.14). These reduced equations depend on the dynamic components of the Fourier series expansion (Eq. A.15). We then find analytic approximations for the oscillatory components of the bead responses for an N degree of freedom linear damped oscillator system with periodically varying forcing frequency. The presence of damping terms leads to steady state periodic responses. Due to the presence of damping, the amplitudes of the dynamic components of the

bead responses (i.e., the oscillations about the beads' static offsets) decrease with increasing frequency. For a particular fixed frequency these amplitudes decrease away from the site of the actuator, i.e., $x_j(\tau) > x_{j+1}(\tau)$, confirming the attenuatory nature of the dynamics, as described above.

The agreement between numerical and analytical response for the forced two-bead system is presented in Fig. A.8. The analytical responses closely match the numerical ones, and both $x_1(\tau) > x_2(\tau)$ and $\delta_1 > \delta_2$. Although the transient dynamics is not captured by our analytic study, the steady state dynamics shows good correspondence between analytical prediction and numerical simulation.

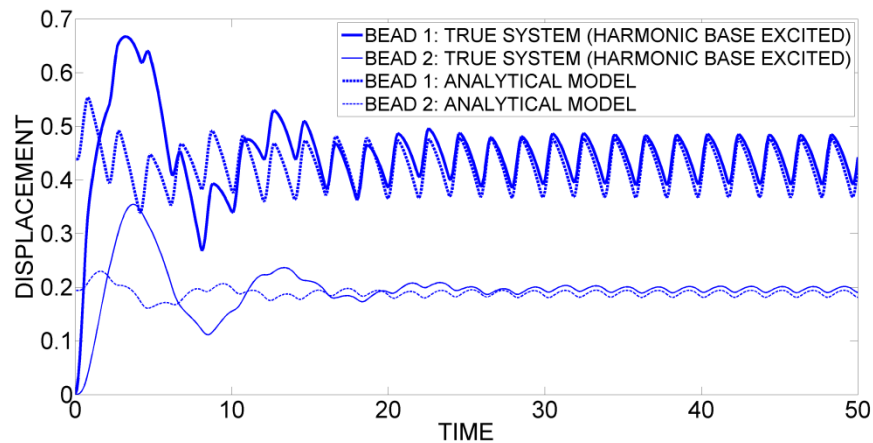


Figure A.8: Correspondence between analytical and numerical response of the 2-bead system when the dynamics is in the attenuation zone. All units are non-dimensional.